Master's thesis

NTNU
Norwegian University of Science and Technology
Faculty of Natural Sciences
Department of Materials Science and Engineering

Kristoffer Eggestad

Computational Study of Migration Barriers in the Li Ion Solid State Electrolyte $Li_7La_3Zr_2O_{12}$

Master's thesis in Chemical Engineering and Biotechnology
Supervisor: Professor Sverre M. Selbach
Co-supervisor: Post doc. Dr. Benjamin A. D. Williamson
June 2021

NTNU
Norwegian University of
Science and Technology

Abstract

To combat climate change, new technology in the field of energy storage needs to be developed. To ensure safe and high performing batteries, current state of the art solid state electrolytes needs to be improved. In this project the Li ion mobility of the known solid state electrolyte $Li_7La_3Zr_2O_{12}$ has been investigated using density functional theory. The tetragonal $Li_7La_3Zr_2O_{12}$ structure is stable in room temperature and this phase has been studied during this project.

Migration barriers for the vacancy, interstitial and interstitialcy transport mechanisms have been calculated using climbing image nudged elastic band calculations. The effects of point defects on the migration barriers for vacancy diffusion have also been investigated. These point defects include low-energy native defects as well as defects resulting from Al-, Nb- and Y-doping. The effects of localisation of a charge compensating electron or hole has also been studied for vacancy diffusion. The $Nb_{Zr}^{\bullet}$ and $Y_{Zr}^{'}$ defects were chosen to evaluate the response of a localised electron and hole, respectively. Lastly, the calculated migration barriers were used together with charge carrier densities in order to estimate the ionic conductivity from the different transport mechanisms and to estimate ionic conductivities in the undoped, Al-doped, Nb-doped and Y-doped structures.

The results show a very low migration barrier for vacancy diffusion of 0.110 eV. The interstitial mechanism shows very large migration barriers of more than 2 eV, while the interstitialcy paths show relatively low migration barriers of 0.2-0.4 eV. The introduction of additional point defects to the vacancy paths resulted in a small increase in migration barriers, with the Y_{La}^{x} showing the highest migration barriers of 0.199 and 0.171 eV. The localisation of either an electron or a hole on different ions resulted in a small difference in the migration barrier compared to the migration barriers calculated without the forced localisation. Furthermore, the calculations with different sites of localisation resulted in almost identical migration barriers. The Li ion conductivity from vacancy diffusion was predicted to be in the order of 10^{-5} $\frac{\mathrm{S}}{\mathrm{cm}}$ for undoped, Al-doped and Y-doped structures, respectively. The Nb-doped structure, with charge carrier densities calculated from an O-rich/metal poor sintering environment, displayed an ionic conductivity in the order of 10^{-4} $\frac{\mathrm{S}}{\mathrm{cm}}$. The calculated contribution from interstitialcy diffusion resulted in values in the order of 10^{-8} $\frac{\mathrm{S}}{\mathrm{cm}}$.

Overall, the results show that vacancy diffusion is the main contributor to Li-ion conductivity. The calculated ionic conductivities are about 10 times larger than experimental values. This discrepancy is likely due to the large charge carrier densities as a result of using the PBEsol functional instead of a hybrid functional. In spite of the deviation in the ionic conductivity, the results show that aliovalent doping of the tetragonal $Li_7La_3Zr_2O_{12}$ structure can lead to an increase in ionic conductivity. Further work should include investigating additional point defects in order to study if the vacancy migration barriers are vulnerable to some types of defects. In addition, other structures should also be researched to investigated if similar results are observed in similar structures.

Sammendrag

For å bekjempe klimaforandringer må ny teknologi innefor energilargingsfeltet utvikles. For å sikre trygge og gode batterier må faststoffelektrolyttene, som brukes per dags dato, forbedres. I dette prosjektet ble mobiliteten til Li-ioner i den kjente faststoffelektrolytten $Li_7La_3Zr_2O_{12}$ undersøkt. Den tetragonale fasen til $Li_7La_3Zr_2O_{12}$ strukturen er stabil ved romtemperatur og det er denne fasen som ble undersøkt i dette prosjektet.

Migrasjonsbarrierer for vakans, interstitiell og kjedeinterstitell transportmekanisme har blitt beregnet ved "CI-NEB" kalkulasjoner. Effekten av ekstra punktdefekter på migrasjonsbarrierene for vakansdiffusjon har også blitt undersøkt. Disse defektene inkluderer lavenergi intrinske defekter og defekter som dannes som et resultat av doping med Al, Nb og Y. Effekten av lokalisering av et ladningskompenserende elektron eller hull på migrasjonsbarrierene for vakansdiffusjon har også blitt studert. Defektene som ble valgt for å teste lokalisering av et elektron og et hull var henholdsvis $Nb^{\bullet}_{Zr}$ og Y'_{Zr}. Til slutt ble de beregnede migrasjonsbarrierene brukt sammen ladningsbærertettheter til å estimere ioneledningsevne fra de forskjellige transportmekanismene og til å estimere ioneledningsevner i udopet, Al-dopet, Nb-dopet and Y-dopet strukturer.

Resultene viser en veldig lav migrasjonbarriere for vakansdiffusion på 0.110 eV. Den interstitielle transportmekanismen viser svært høye migrasjonsbarrierer på mer enn 2 eV, mens den kjedeinterstitielle mekanismen viser relativt lave migrasjonsbarrierer på 0.2-0.4 eV. Introduksjonen av punktdefekter til vakansveiene resulterte i noe forhøyede i migrasjonsbarrierer, der Y^x_{La} defekten viser størst økning opp til 0.199 og 0.171 eV. Lokalisering av enten et elektron eller et hull på forskjellige ioner resulterte i en liten forskjell i migrasjonsbarrierene. Dessuten resulterte kalkulasjonene med lokalisering av et elektron eller hull på de forskjellige ionene i nesten identiske migrasjonsbarrierer. Ledningsevnen av Li-ioner fra vakansdiffusjon ble estimert til å være over 10^{-5} $\frac{S}{cm}$ for den udoped, Al-dopede og Y-dopede strukturen. Den Nb-dopede strukturen, med ladningsbærertetthet beregnet fra O-rikt/metallfattig sintringsmiljø, viste en ioneledningsevne på over 10^{-4} $\frac{S}{cm}$. Bidraget til ledningsevnen fra kjedeinterstitielldiffusjon ble beregnet til å være rundt 10^{-8} $\frac{S}{cm}$.

Resultatene viser at vakansdiffusjon er hovedbidragsyteren til ledningsevne av Li-ioner. De beregnede ioneledningsevnen er omtrent 10 ganger større enn eksperimenelle verdier. Denne forskjellen skylles antageligvis den store ladningsbærertettheten som igjen kan skyldes bruken av PBEsol funksjonalet istedet for et hybridfunksjonal. På tross av denne feilen i beregnet ledningseve viser resultatene at aliovalent doping av tetragonal $Li_7La_3Zr_2O_{12}$ kan føre til en forbedring av ledningsevnen av Li-ioner. Videre arbeid bør innkludere undersøkelser av flere punkt defekter for å kunne studere om migrasjonbarrierene fra vakansdiffusjon er sårbare mot noen typer defekter. I tillegg bør også andre strukturer undersøkes for å sjekke om tilsvarende resultater observeres i lignende strukturer.

Preface

This master's thesis is the result of the course *TMT4900 - Materials Chemistry and Energy Technology, Master's Thesis* at the Department of Materials Science and Technology at the Norwegian University of Technology and Science. The project is also a part of the OXIBAT project, dedicated to developing next generation oxide electrolytes for solid-state batteries. All computations completed during the project were performed on resources provided by UNINETT Sigma2 - the National Infrastructure for High Performance Computing and Data Storage in Norway.

Acknowledgements

First and foremost, I would like to thank my supervisors, Professor Sverre M. Selbach and Post doc. Dr. Benjamin A. D. Williamson, for their excellent guidance. In addition to the irreplaceable help, they created a great environment for learning and research. Secondly, I would like to thank the OXIBAT project for providing invaluable information, feedback and discussions. I would also like to thank the Battery group at the department for teaching me about all the aspects of a battery as well as the great feedback. Lastly, I would like to thank my friends, classmates and family for all their continuous support during my five years at NTNU. Especially I would like to thank my fellow master's student, Ivar L. Råheim, for all the help and fun he has provided during work on the master's thesis.

Table of Contents

List of Figures

List of Tables

Abbreviations

DFT - Density Functional Theory

LIB - Lithium Ion Battery

LLZO - Lithium Lanthanum Zirconium Oxide

NEB - Nudged Elastic Band

SSE - Solid State Electrolyte

VASP - Vienna *Ab-Initio* Simulation Package

1 Introduction

Climate change is listed, by the United Nations, as one of the global issues the world is facing [1]. Decades of burning fossil fuel has lead to an increase in the amount of CO_2 in the atmosphere and it is one of the major contributors to the strengthened green house effect. Other gases such as water, methane and ozone also contribute to this effect [2]. A dangerous result of the increased green house effect is a global rise in average temperature. For instance, release of bound water by melting of inland ice will cause the global mean sea level to rise. World wide more than 200 million people live less then 5 meters above the sea level [3] and will therefore suffer consequences and forced to move. In addition, a large number of the worlds biggest cities are located in coastal areas and will be partly destroyed by an increase in the mean sea level.

To avoid catastrophic consequences of climate change and global warming, the temperature increase needs to be kept as low as possible. Therefore, as a result of the annual United Nations Climate Conference held in Paris in 2015, the Paris Agreement was made. The agreement is a legally binding international treaty with a goal of limiting the increase in global average temperature to well below 2 °C above pre-industrial levels and preferably below 1.5 °C [4]. The IPCC's (Intergovernmental Panel on Climate Change) Special Report from 2018, on the impacts of global warming of 1.5 °C above pre-industrial levels, states that limiting the global temperature increase to under 1.5 °C would demand unprecedented changes to all aspects of the human society [5]. In order to reach the goal, the burning of fossil fuel needs to stop, and to facilitate this change new technology in the field of energy production and storage needs to be developed.

Battery technology have gained increasingly more attention during the last couple of decades and are now one of major energy storage technologies in use. The main advantages of batteries are that they can store electric energy, which can be produced environmentally friendly, they are in some degree portable and it is very easy to retrieve the stored energy from batteries. Unfortunately, there do not exists a single type of battery that is best suited for all purposes and scenarios and therefore, many different battery technologies are currently in use. There are still several challenges with current state of the art batteries that needs to be solved.

Many of the different variations of Li ion batteries show promising properties and are widely researched. However, they are all facing many difficult challenges. For example, many of the different types use a type electrolyte made of an organic liquid or gel, which is often very flammable. Another common problem is degradation of the batteries which in turn leads to capacity and power loss. The cause of degradation could for example be due to the formation of a solid electrolyte interface, formation of dendrites or decomposition of binders [6]. Binders are additives that are necessary for ensuring good contact between electrodes and the and metal current collectors [7].

A possible solution to many of the challenges is to introduce a solid state electrolyte. These solid electrolytes are usually made out of non-flammable ceramics and will therefore resolve this safety issue in these types of batteries. In addition, Li ion batteries with solid electrolytes are expected to endure many charge and discharge cycles and have a long life time, due to the dendrites difficulty forming and growing in solids. However, there are still many challenges with solid state electrolytes with respect to their ionic conductivity.

Unfortunately, solids have a tendency to inhibit lower ionic conductivity than liquids and therefore, a lot of research focuses on exactly this property.

This project is dedicated to investigate the known solid state electrolyte $Li_7La_3Zr_2O_{12}$ with the aim of gaining a fundamental understanding of Li ion transport in solids. The research will be conducted by the use of materials simulations with density functional theory (DFT). In addition, methods for improving ionic conductivity will also be studied. The project will follow the flow chart shown in figure 1.1 and end by using results from previous work [8] together with results from this project to predict Li ion conductivity in different variations of the $Li_7La_3Zr_2O_{12}$ structure. The goal of the project is to contribute to the knowledge regarding mechanisms of Li ion conductivity in order to facilitate prediction of materials and structures for future solid state electrolytes.

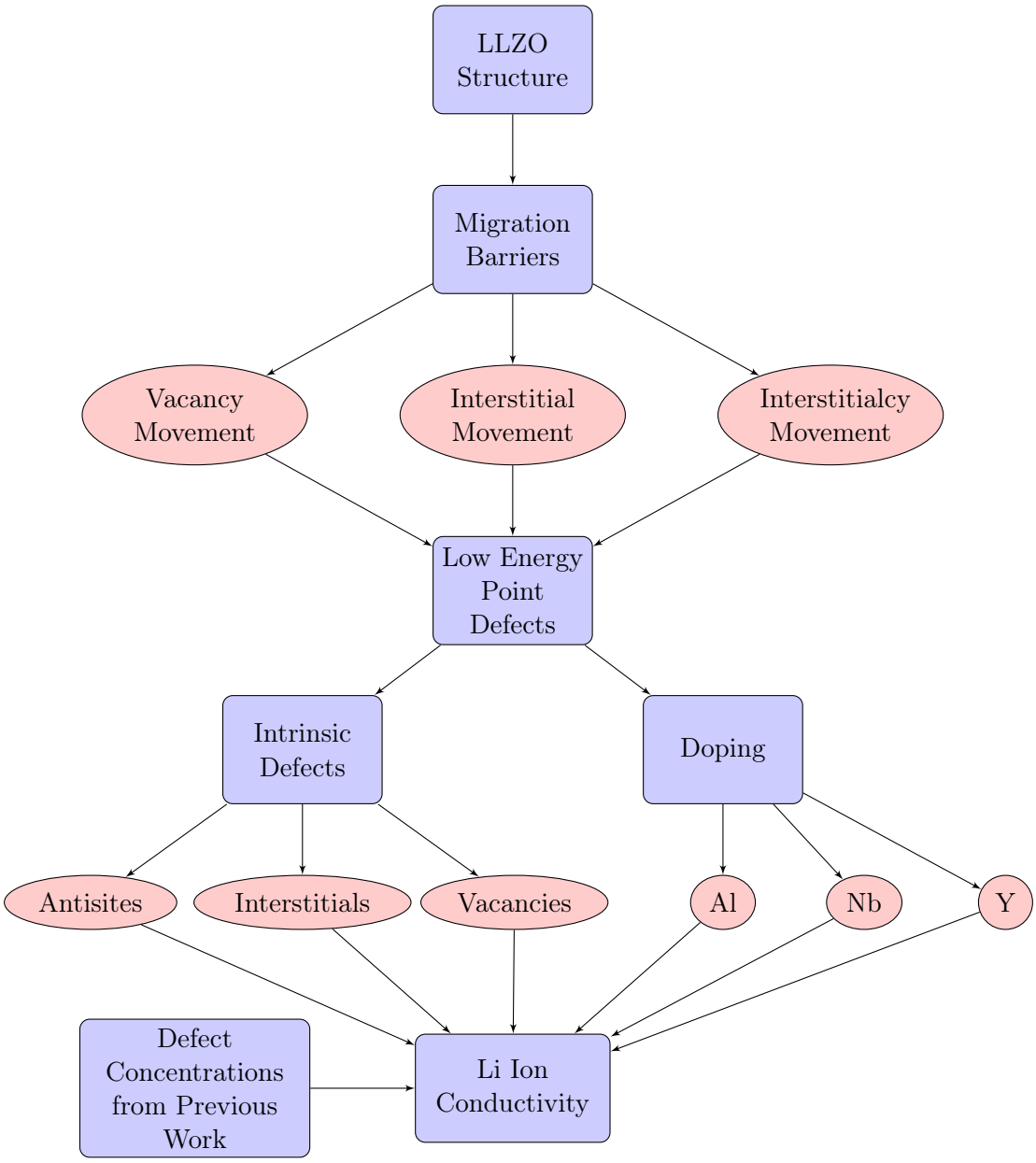

Figure 1.1: Flowchart describing the project

2 Background

2.1 Batteries

There are two main types of electrochemical power sources, fuel cells and batteries. Batteries are categorised as either primary or secondary cells, where the primary batteries inhibits only the galvanic operating mode, while secondary batteries also have the ability to operate electrolytically. In other words, secondary cells are rechargeable while primary cells are not. The voltaic pile, constructed by Alessandro Volta in 1800, is commonly recognised as the worlds first battery, even though archaeologist have found devices resembling batteries originating from the antiquity. Volta's pile was made of a stack of alternating Zn and Cu disks separated by cloth soaked in brine and could produce a steady flow of electrical current [9].

There are three main components of a battery. A cathode, an anode and an electrolyte. During discharge an oxidation reaction is happening at the anode at the same time as a reduction reaction is happening at the cathode. In addition, while these reactions are taken place, electrons are moving from the anode, through an outer circuitry, to the cathode. Simultaneously, the active ions are moving from the anode to the cathode through the electrolyte. What the active ions are depends on the type of battery and could for example be Li ions. During charging all of these reactions are reversed [9].

There are several different properties a battery needs to inhibit to be successful. Some of these are high specific energy, high energy density, high charging rate, long life time and low cost. In addition, safety and the stability of the battery is also very important. Currently, there do not exist a single type of battery in the lead in all of these categories and therefore, different batteries are chosen for different situations.

Li ion batteries or LIBs are currently one of the most familiar types of batteries and have during the last decade revolutionized the electric vehicle industry. Rechargeable LIBs was first commercialized by Sony CO. in 1991 and have been growing in popularity ever since. However, primary LIBs were developed already in the early 1970s as a response to the demand for better batteries. Li, with its low atomic number and high electrode potential, was an ideal candidate to challenge the battery technology in use at that time. Research and development of the first rechargeable LIBs was troubled by difficulties concerning safety as a result of dendrite formation. Dendrite formation in LIBs is uneven deposition of Li during charge/discharge cycles and is still one of the major problems with current state of the art LIBs causing degradation and shortened lifetime [7].

Similar to other batteries, LIBs are also made of a cathode, an anode and an electrolyte. Carbon is very often used as anode material, but silicon has lately gained a lot of attention and is heavily researched. One of the main challenges with the use of silicone anodes is the large volume expansion, of up to 400 % [10], during lithiation. Li metal anodes are also in consideration with its very high theoretical specific capacity ($2860\frac{mAh}{g}$), low density ($0.59\frac{g}{cm^3}$) and strongly reducing properties ($-3.040V$), but challenges concerning dendrite formation and low Coulombic efficiently have made it difficult to use [11]. Compared to the number of anode materials, a lot of different cathode materials are researched and used. Earlier many of these materials contained a large portion Co, but due to the problems

concerning obtaining Co as well as new knowledge with respect to cathode materials and properties, less and less Co are used. Co is not an abundant element, which makes it expensive, in addition to political and ethical issues concerning the Co mines in Africa [12]. One of the most known cathode materials used in LIBs is $LiCo_2O$. $LiCo_2O$ has been a successful cathode material, but it is expensive compared to other materials and has problems with stability and degradation when overcharged [13, 14, 15]. The electrolytes used in LIBs are generally made of a Li salt in an organic liquid or gel. $LiPF_6$ is one example of a salt that is commonly used and shows great performance, but at elevated temperature it can become unstable [16]. In addition, the organic solvent is often very flammable and dendrites are easily able to grow in them.

Many new battery technologies are currently being researched and are not yet commercialized. An example of a type of battery, that might be an alternative to LIBs in the future, is Mg ion battery. Mg batteries have the possibility to use Mg metal anodes, which have a theoretical volumetric energy density of almost two times the theoretical volumetric energy density of Li metal anodes. In addition, Mg metal anodes do not have problems with dendrite formation during charge/discharge cycles and do not react violently with water. Furthermore, other advantages of Mg is that it is more abundant than Li and Mg metal can be produced from sea water [17].

2.2 Solid State Electrolytes

One solution to many of the current challenges with LIBs is to replace the organic electrolyte with a solid state electrolyte (SSE). Importantly, this will remove the flammable organic part of the electrolyte and resolve the safety issue. In addition, all solid state batteries are more durable due to the nature of solids compared to liquids. Furthermore, solids generally reacts slower than liquids and therefore, solid batteries are expected to endure more charge/discharge cycles, which consequently leads to longer expected life span. Thermal stability is also very important for batteries, and in conditions where liquid electrolytes would freeze, boil or decompose many of the proposed SSEs will be stable. The good chemical stability of many SSEs also makes it possible to introduce high performing electrodes like Li metal anodes [18]. Lastly, the use of SSEs could lead to an increase in both specific energy and energy density due to the possible combinations with high voltage cathode materials as well as high capacity anode materials [19].

One of the main challenges of many possible SSE materials is the low ionic conductivity at ambient temperature [20]. Another major challenge is the stability of the SSEs. Many of the possible candidates cannot survive the reducing environment at the anode when for instance a Li metal anode is used [19, 20]. In addition, many also have troubles with thermal stability and decomposes at higher temperatures [20]. An advantage with SSEs is that dendrites does not easily form, however there are still challenges with dendrite formation. The last main challenge with SSEs is the interface between the electrolyte and the electrodes. During charge/discharge cycles there will be a volume expansion and contraction in the materials and this can result in cracks and poor contact between the electrolyte and electrodes [19]. In addition, all solid state batteries can also suffer problems with thermal expansion. If the materials used in the battery have very different thermal expansion coefficients, the results can be cracks in the interfaces during production as well as during usage. A consequence of these cracks and poor contact is reduced ionic conductivity in the interfaces.

There are several different types of SSEs and two of them are inorganic oxide and sul-

fide electrolytes. Oxide electrolytes exhibits large bandgaps which results in high stability against high voltages and are therefore suitable for strongly reducing or oxidizing electrodes. In addition, many of the oxide SSEs are relatively stable in air which is desirable for electrolyte research as well as commercialisation of batteries. Some of the challenges with oxide electrolytes is that they often require high sintering temperature to achieve the desired density and ionic conductivity. Consequently, the electrolytes thermal stability, in addition to the thermal expansion coefficients, becomes very important. Oxide electrolytes often also show low ionic conductivity and it is usually contributed to the attraction between the negative O and positive Li ions. In sulfide based electrolytes the O ions are changed with S ions and the problem with attraction between anions and Li ions is therefore reduced. S ions are also larger than O ions and the use of S ions may lead to larger Li pathways in the structure, thus higher Li ion conductivity. In addition, sulfides are in general soft and malleable compared to oxides and it is therefore easier to achieve a good contact between the electrolyte and the electrodes [21].

In general, a good solid state electrolyte material needs to have high ionic conductivity, preferably more than $10^{-3}\frac{S}{cm}$ at room temperature, and electronic conductivity of less than $10^{-8}\frac{S}{cm}$ to limit or prevent self-discharge. In addition, the electrolyte needs to have high electrochemical, chemical and thermal stability to be suitable for a wide range of cathode and anode materials. Lastly, the electrolyte should be made of abundant, nontoxic elements [22].

2.3 Ionic Conductivity

The two major types of electrical conductivity in solid materials are electronic and ionic conductivity. In electronic conductivity the carrier of electrical charge are electrons and holes, while in ionic conductivity, ions or vacancies are charge carriers. The charge carried by a single electron is the elementary charge, in contrast to ions where their charge is dependent on their valency. For instance the charge carried by a single Li^+ ion is one times the elementary charge, while the charge carried by Mg^{2+} ions is two times the elementary charge [23].

$$\sigma = nq\mu \tag{2.3.1}$$

Equation 2.3.1 displays conductivity as a function of the number of charge carriers in a certain volume, n, the charge of the charge carrier, q, and the mobility of the charge carrier, μ. If there are multiple charge carriers the conductivity can be expressed as a sum of the contribution from the different charge carriers, 2.3.2.

$$\sigma = \sum_i \sigma_i = \sum_i n_i q_i \mu_i \tag{2.3.2}$$

For a Li ion battery to work it is crucial that the electrolyte transport Li ions and therefore, the conductivity of Li ions in the electrolyte is very important. Both the number of charge carriers as well as the mobility should be optimised to improve this critical property. Examples of possible Li ion charge carriers are V'_{Li} and $Li_i^{\bullet}$. The number of point defects can be increased by tuning the sintering environment and by aliovalent doping. The sintering environment can be tuned by for example changing the composition of the sintering atmosphere or by increasing or decreasing the temperature. For instance, increasing the

partial pressure of oxygen can increase the amount of oxygen in the material. Possible results of this change could for example be more oxygen interstitials and less oxygen vacancies. Aliovalent doping is to introduce other species with different oxidation states into the structure and the goal is to induce charge compensating defects. For example changing a Na^{+} ion into a Mg^{2+} in the NaCl structure will lead to a charge of $+1$ that needs to be compensated. The structure can in principle compensate this charge by either making a V'_{Na} or a Cl'_{i} [24], and where latter is much less likely than former.

2.3.1 Ionic Transport Mechanisms

There three main mechanisms of transport in ionic compounds and which mechanism that is the most prominent in a material is highly dependent of both the structure an the size of the ions. These mechanisms are vacancy, interstitial and interstitialcy diffusion. A common element in these three mechanisms is that they all start in a local equilibrium state. Thereafter, they reach a saddle point where maximum lattice strain occurs, and lastly the structures settles in another local equilibrium state [24], more on this topic in Section 2.3.2.

Vacancy diffusion, illustrated in Figure 2.1, is where an ion moves from its lattice site to a vacancy site in its vicinity. This movement results in an empty lattice site, where the ion was initially situated. Other ions will now be able to move to this site and the process can be repeated. To get a flow of ions this mechanism is repeated over and over again [25, 26]. Vacancies are recognised as one of the most important point defects in metals and ionic crystals and the vacancy mechanism is known to be a dominant mechanism of diffusion in many materials [24].

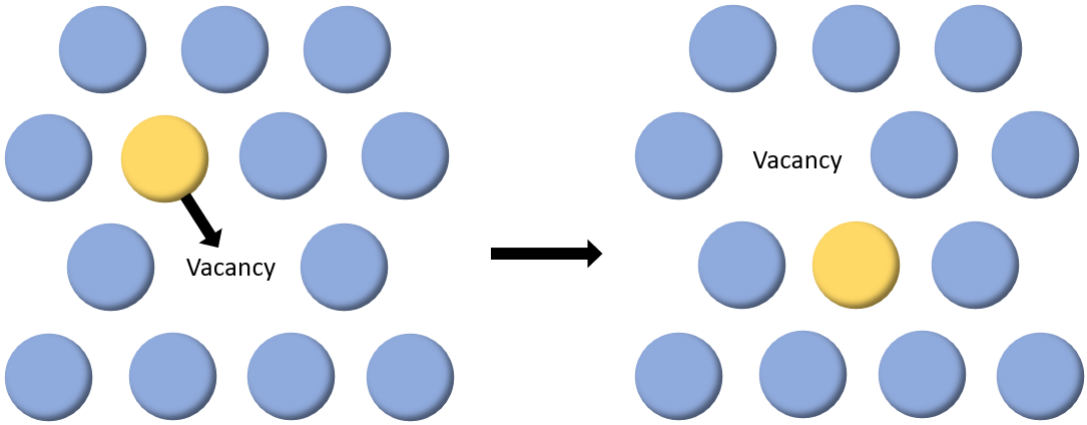

Figure 2.1: Vacancy diffusion. The ion marked in yellow moves from its lattice site to a vacancy/free lattice site close by.

Interstitial diffusion is where an ion moves from interstitial site to interstitial site through the structure. Figure 2.2 displays this mechanism and the interstitial ion is marked with red. This diffusion mechanism is very difficult for larger ions due to the small nature of the interstitial sites, as well as the narrow interstitial path in between lattice ions [26].

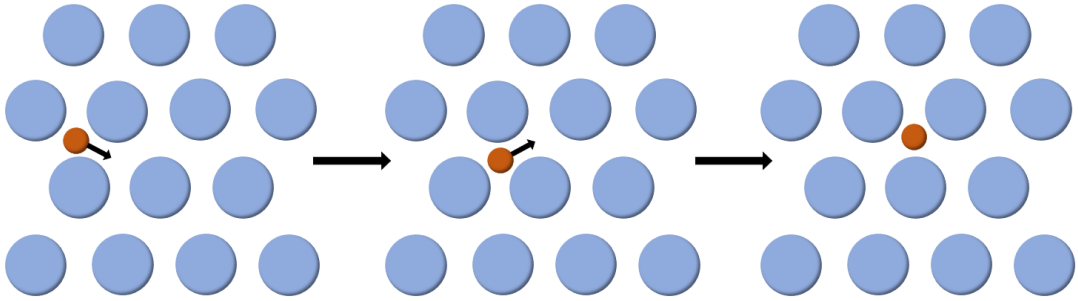

Figure 2.2: Interstitial diffusion. The small ion marked in red moves through the lattice from interstitial site to interstitial site.

The third mechanism is interstitialcy diffusion and are illustrated in Figure 2.3. An ion at an interstitial site (coloured in green) pushes another ion (coloured in purple) from its lattice site into another interstitial site while simultaneously moving to and occupying the lattice site where the other ion was initially situated [26].

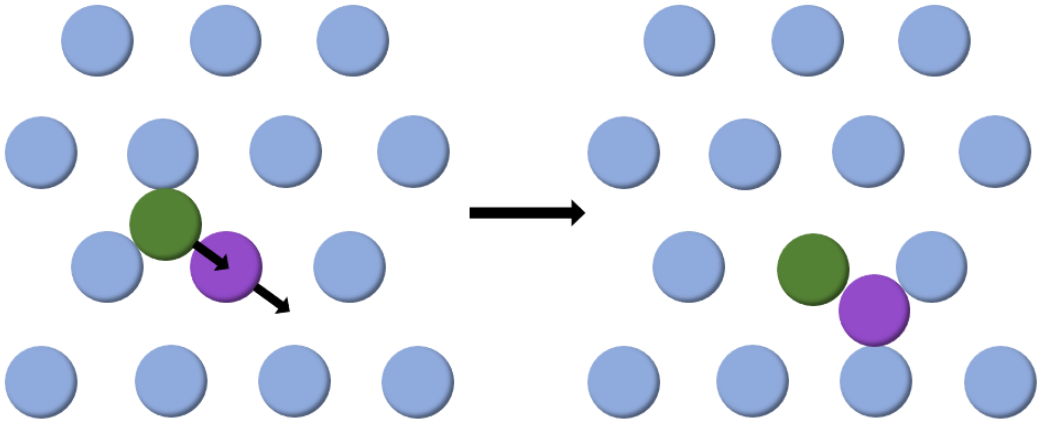

Figure 2.3: Interstitialcy diffusion. The green ion pushes the purple from its lattice site into an interstitial site.

2.3.2 Migration Barriers

Ionic conduction are often limited by the mobility of the charge carriers. The challenge is that positive ions are surrounded by negative ions and negative ions are surrounded by positive ions. This configuration often results in very stable compounds and a lot of energy needs to be added in order for the charge carriers to be able to move. This energy barrier is called the migration barrier [23, 25]. Figure 2.4 shows vacancy diffusion (a) together with an energy profile (b) to illustrate the migration barrier. Both the initial and final structures are in a local minimum and for the ion to move it must have enough energy to pass the saddle point.

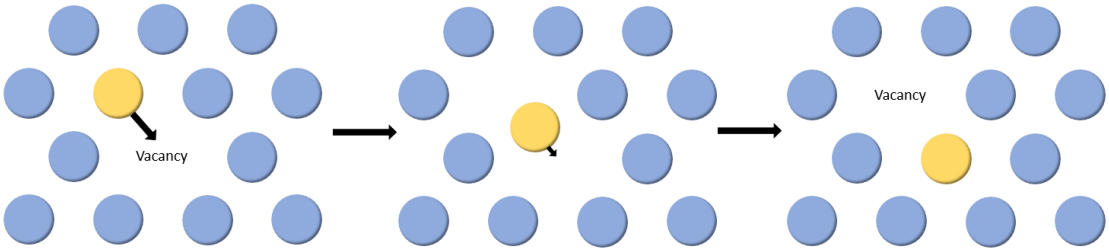

(a) Vacancy diffusion

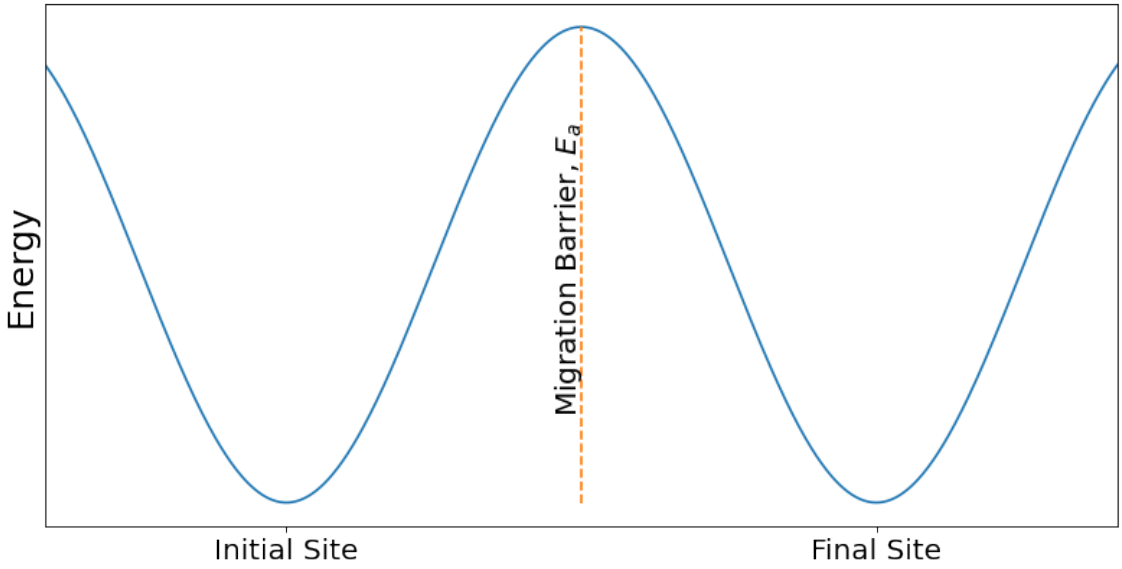

(b) Energy profile

Figure 2.4: Migration barrier

Above 0 K all atoms are vibrating and the energy state of atoms can therefore be described by probability functions. The probability of an ion to overcome the energy barrier and move is proportional to the Boltzmann distribution as described by equation 2.3.3 [21, 27].

$$\rho \propto e^{-\frac{E_a}{k_B T}} \tag{2.3.3}$$

Where E_a is the energy barrier, T is the absolute temperature and k_B is the Boltzmann's constant. The probability for an ion to move is therefore increasing with decreasing migration barrier as well as increasing with increasing temperature. As a result, the ionic conductivity is also increasing with increasing temperature and decreasing migration barrier.

2.4 Mobility

The mobility, μ, of a charge carrier describes how easily the charge carrier can move and it is a function of the temperature, the diffusion coefficient, D, and the charge.

$$\mu_i = \frac{q_i D_i}{k_B T} \tag{2.4.1}$$

The diffusion coefficient can further be described by the following equation:

$$D_i = D_0 \exp\left(-\frac{E_a}{k_B T}\right) \tag{2.4.2}$$

Where D_0 is the diffusion pre-factor. Adding equation 2.3.1 and 2.4.1 together gives the Nernst-Einstein equation displayed in equation 2.4.3 [28]. This equation can be used to calculate ionic conductivity based on migration barriers and charge carrier densities.

$$\sigma = \frac{n_i q_i^2 D_i}{k_B T} \tag{2.4.3}$$

2.5 LLZO

LLZO or $Li_7La_3Zr_2O_{12}$ is a known Li ion conductor and can be used as a solid electrolyte in LIBs. The SSE have many favourable properties and the most noticeable being relatively high ionic conductivity, wide electrochemical stability window and dry air stability [29]. The wide electrochemical stability region makes the structure compatible with Li metal anodes and a wide range of cathode materials. The Li stuffed garnet consists of Li in tetrahedral, octahedral and distorted octahedral sites as well as ZrO_6 octahedral and LaO_8 dodecahedral [30], see Figure 2.5 (b). Table 2.1 displays the lattice parameters, the space group and the different atomic positions in the tetragonal LLZO structure.

Table 2.1: The tetragonal $Li_7La_3Zr_2O_{12}$ structure

Lattice parameters	$a = b = 13.24$ Å $c = 12.70$ Å $\alpha = \beta = \gamma = 90°$	
Space Group	$I4_1/acd$	
Atomic Positions [30]	Li	Tetrahedral, 8a Octahedral, 16f Distorted Octahedral, 32g
	Zr	Octahedral, 16c
	La	Dodecahedral, 8b, 16e

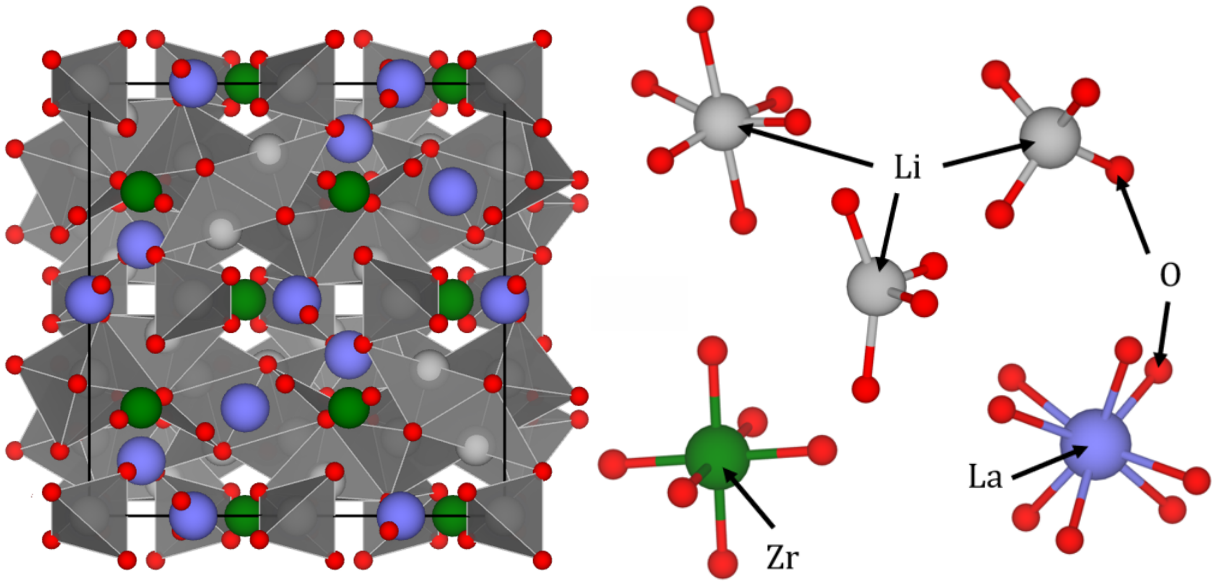

(a) The conventional cell with lithium polyhedral colored in grey

(b) The different cation sites

Figure 2.5: The tetragonal $Li_7La_3Zr_2O_{12}$ structure visualized by the use of `VESTA`

The thermodynamically stable phase of LLZO in room temperature is the tetragonal phase, see Figure 2.5 (a), but the cubic phase is known to have higher Li^+ conductivity. The cubic phase is often reported with around two orders of magnitude better ionic conductivity than the tetragonal phase [31], thus more desirable. Therefore, a lot of research have been dedicated to try to stabilize this phase at room temperature, and aliovalent doping, with for example Nb^{5+} at Zr^{4+} sites and Al^{3+} at Li^+ sites, has proven to stabilize the cubic structure [32]. The introduction of hypervalent cations results in the formation of additional defects and the overall entropy will increase. The cubic structure will then be stabilized as a result of the increased disorder. Table 2.2 displays examples of reported Li ion conductivities for both the tetragonal and the cubic LLZO phase.

Table 2.2: The ionic conductivity of the tetragonal and cubic phase of $Li_7La_3Zr_2O_{12}$

Structure	Space Group	Lithium Ion Conductivity
Tetragonal LLZO	$I4_1/acd$	$1.63 \cdot 10^{-6}$ at 27 °C [33]
Cubic LLZO	$Ia\bar{3}d$	$5.11 \cdot 10^{-4}$ at 25 °C [34]

Even though the ionic conductivity of the LLZO structure is relative high, it would be preferable if it was even better. A common method used to increase ionic conductivity in solids is aliovalent doping. Doping with ions with a different oxidation state will demand compensation in the structure, thus inducing additional defects. For instance doping the Zr^{4+} sites with Nb^{5+} will result in a charge of $+1$ that needs to be compensated. This can for example be done by removing one Li ion, thus creating a V'_{Li}. To increase the Li ion conductivity in LLZO more Li vacancies are preferred and equation 2.5.1 and 2.5.2 shows an ideal case where the scenario above is described.

$$Nb_2O_5 \xrightarrow{ZrO_2} 2\,Nb^{\bullet}_{Zr} + O''_i + 4\,O^x_O \tag{2.5.1}$$

$$\mathrm{O}_i^{''} + 2\,\mathrm{Li}_{\mathrm{Li}}^{x} \rightleftharpoons 2\,\mathrm{V}_{\mathrm{Li}}^{'} + \mathrm{Li_2O\ (g)} \tag{2.5.2}$$

Aliovalent doping could have favourable results with respect to both the stabilisation of the cubic phase and inducing desired defects, but the introduction of hypervalent cations may also have some possible trade-offs. The extrinsic defects may for instance reduce the mobility of the Li ions by either blocking the paths or having a strong affinity for the Li ions or vacancies. Therefore, doping with hypervalent cations may lead to an increase in the migration barriers and consequently a decrease in the overall ionic conductivity. Migration barriers in the cubic LLZO structure is reported to be around 0.3 eV by both molecular dynamics and DFT with the PBE functional, and a little higher values for the tetragonal structure [35, 36]. Experimental results also show a migration barrier of about 0.3 eV at room temperature for the cubic structure [37].

There are several challenges with respect to the sintering process of SSEs. LLZO and many of the other SSEs show problems with Li loss during sintering. The vaporization of Li is a known problem and can have a large impact on the relative density of the electrolytes, thus also the ionic conductivity [38]. Li_2CO_3(s) can be and is often used as Li source in the making of LLZO [39] and equation 2.5.3 shows how Li may escape from high temperature systems.

$$\mathrm{Li_2CO_3(s)} \xrightarrow{\text{High T}} \mathrm{Li_2O\,(g) + CO_2(g)} \tag{2.5.3}$$

To resolve the issue of volatilisation of Li, the sintering temperature is often kept as low as possible and Li salts are often added in excess. On the contrary, low temperature sintering can also result in low density materials and therefore, additives are often added to aid the sintering process. The addition of Al^{3+} ions have for instance proven to reduce the amount of Li escaping during sintering by forming a protective $LiAlO_2$ layer on the surface [40]. In addition, the relative density is also important with respect to dendrite formation. Dendrites are known to form in grain boundaries and will with high current density eventually lead to short-circuiting [41]. However, the short-circuiting period is shown to be increasing with increasing relative density for LLZO like structures, and it is therefore reasonable to contribute this to the growth of dendrites being more difficult in materials with high relative density [42].

Investigations of the LLZO structure by Squires et al. [43] by the use of DFT have shown a wide range of different native defects. This includes O and Li interstitials and vacancies as well as several cation antisites; $\mathrm{Li}_{\mathrm{La}}^{''}$, $\mathrm{La}_{\mathrm{Zr}}^{'}$, $\mathrm{Li}_{\mathrm{Zr}}^{'''}$ and $\mathrm{Zr}_{\mathrm{Li}}^{\bullet\bullet\bullet}$. $\mathrm{V}_{\mathrm{Li}}^{'}$ is shown to be one of the most prominent defects for both oxygen poor and rich environments and the O defects were shown to be strongly dependent on the environment. Extrinsic defects have been investigated in previous work [8] and prove that both doping with Nb and Al can induce desired defects in the structure. In other words, the addition of these species in the structure may lead to an increase in the $\mathrm{V}_{\mathrm{Li}}^{'}$ concentration. Figure 2.6 displays how the number of $\mathrm{V}_{\mathrm{Li}}^{'}$ for Al, Nb and Y doped tetragonal LLZO structures depends on the amount of O in the environment. All of these structures are doped with 0.25 atoms per formula unit. It is also shown that Al prefers $\mathrm{Li}^{\mathrm{tet}}$ sites, Nb prefers Zr sites and Y prefers La sites. The site preference of Al^{3+} ions in the cubic LLZO have been investigated by Rettenwander et al. [44] by the use of DFT and concludes that Al^{3+} ions prefer a coordination number of 4 and therefore the $\mathrm{Li}^{\mathrm{tet}}$ sites.

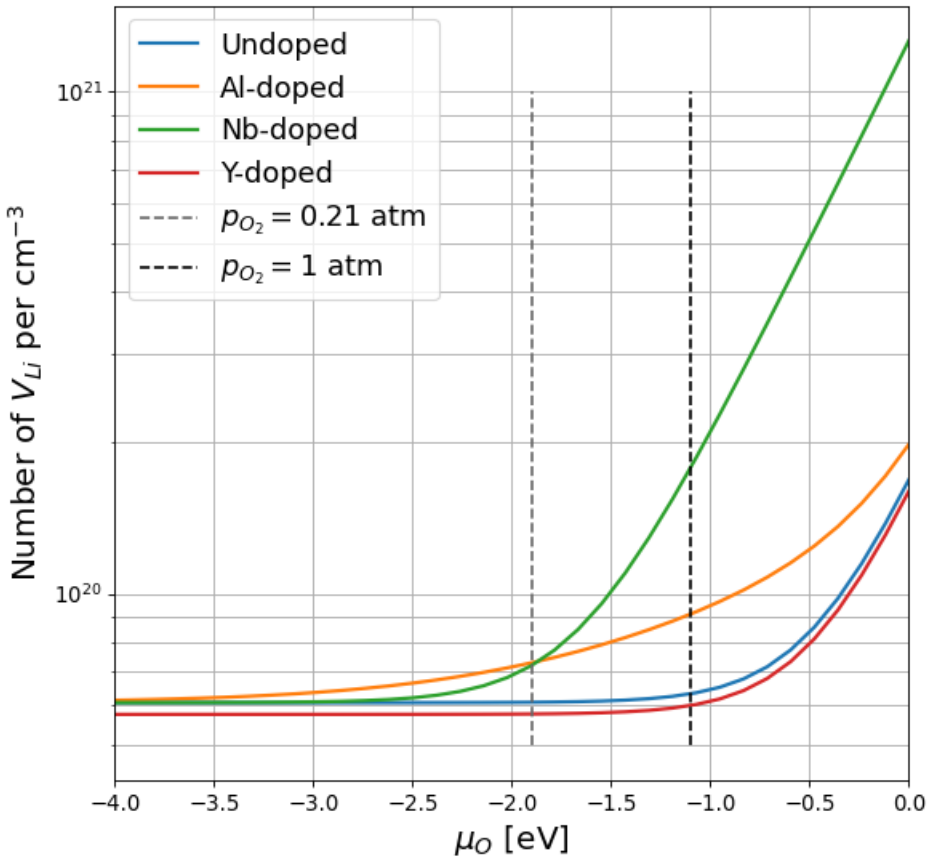

Figure 2.6: The number of lithium vacancies per cm^{-3} as a function of the stability region indicated by the chemical potential of oxygen [8]. O-poor/metal-rich environments are to the left and O-rich/metal-poor environments are to the right.

The diffusion mechanisms in LLZO is not well known and in general, vacancy diffusion is considered the main diffusion mechanism for many inorganic SSEs, but interstitialcy or interstitialcy like diffusion is also recognised in some structures, eg. $Li_{4-x}Ge_{1-x}P_xS_4$ [45]. Regarding the LLZO structure, most researchers assume that vacancy diffusion is the major transport mechanism and do not consider interstitial or interstitialcy diffusion. There are many reports presenting results showing that Li ion conductivity is increasing with increasing number of V'_{Li} [46, 47]. These results indicates that the assumption of vacancy diffusion being a main transport mechanism is correct. On the other hand, V'_{Li} are known to stabilize the cubic LLZO phase and could therefore be the sole reason for the increased ionic conductivity.

Most SSE research are on polycrystalline materials, and this is because it is generally easier to make and produce polycrystalline materials. In polycrystalline SSEs higher density usually translates to higher ionic conductivity. Therefore, it is important to have high density SSEs, and high density can be achieved with small particles with a range of particle sizes [23]. In addition, high density ceramics have in most cases higher strength which is also desirable for SSEs. A consequence of small particles is that there will be a large number of grain boundaries, and therefore, grain boundary diffusion is very important in polycrystalline SSEs. It is shown that Li ion transport in LLZO is limited by grain boundary diffusion. However, the difference between the bulk ionic conductivity and grain boundary conductivity is strongly dependent on temperature. At room temperature the Li ion transport speed in the grain boundaries are very different for the different low energy

grain boundaries. The transport speed ranges from two times slower to two orders of magnitude slower than the ionic conductivity of the bulk [48].

3 Computational Background

The book "Density Functional Theory: A Practical Introduction" by Sholl and Steckel [49] is used as basis for Section 3.1 and 3.2.

3.1 Quantum Mechanics

At the end of 1800s more and more experimental results showed that classical mechanics failed when looking at very small particles. Further investigations proved that the classical concepts of particles and waves blend together and this lead to the birth of the quantum mechanics. Small particles needed to be described not as particles, but instead as particles in a wave like distribution in space. The functions describing these waves are called wave functions, Ψ, and all dynamical information describing a particle can be found within the wave function [27]. Equation 3.1.1 shows the time independent Schrödinger equation.

$$\hat{H}\Psi = E\Psi \tag{3.1.1}$$

Where $\hat{H}$, Ψ and E are the Hamiltonian, wave function and the energy of the system, respectively. The Hamiltonian is an operator describing the energy of the system and includes a kinetic, $\hat{K}$, and a potential, $\hat{V}$, contribution. When looking at systems with both nuclei and electrons, for instance a molecule, the kinetic energy operator can be broken down to a kinetic electron operator and a kinetic nuclei operator. The potential energy can be reduced to contributions from electron electron repulsions, nuclei nuclei repulsions and electron nuclei attractions:

$$\hat{H} = \hat{K} + \hat{V} = (\hat{K}_e + \hat{K}_n) + (\hat{V}_{e,e} + \hat{V}_{n,n} + \hat{V}_{e,n}) \tag{3.1.2}$$

Solving the Schrödinger can give valuable information about a system. For example information about stability of a system or the energy needed to change a system. Because of the complicated nature of the Schrödinger equation the Born-Oppenheimer approximation is often applied. Nuclei are large and slow compared to electrons, and therefore, for a set of nuclei and electrons, the electrons will always be able to move to their ground state before the nuclei have the time to move. In other words, when looking at the electrons the kinetic energy operator for nuclei, $\hat{K}_n$, can be ignored and nuclei nuclei interactions, $\hat{V}_{n,n}$, kept constant. The Hamiltonian operator can then be described as sum of the electronic kinetic energy, electron electron interactions and electron nuclei interactions:

$$\hat{H} = \hat{K}_e + \hat{V}_{e,e} + \hat{V}_{e,n} \tag{3.1.3}$$

As a result, the wave function can be decoupled into two wave functions, equation 3.1.4. One function describing the nuclei and one function describing the electrons. This approximation is called the Born-Oppenheimer approximation.

$$\Psi(\{R_i\}, \{r_i\}) \longrightarrow \Psi_n(\{R_i\}) \cdot \Psi_e(\{r_i\}) \tag{3.1.4}$$

After the Born-Oppenheimer approximation has been applied, there are still challenges with the complexity of the Schrödinger equation. For instance a H_2O molecule consist of 10 electrons, and because there are three spatial coordinates describing each electron, solving the Schrödinger equation for Ψ_e becomes a 30 dimensional problem. The Schrödinger equation can, with the Born-Oppenheimer approximation, be solved for simple systems, but it becomes exponentially more complicated with increasingly larger systems and simplifications are needed. This problem is called *The Many Body Problem*.

3.2 DFT - Density Functional Theory

A solution to *The Many Body Problem* is *Density Functional Theory* and it is based on two important theorems provided by Kohn and Hohenberg [50]. The first theorem states that: *The ground state energy from Schrödinger's equation is a unique functional of the electron density.* The ground state energy, E, can therefore be expressed as:

$$E = E\left[\rho(r)\right] \tag{3.2.1}$$

Where $\rho(r)$ is the electron density and can be expressed as as sum off all the individual electron wave functions and their complex conjugate:

$$\rho(r) = 2\sum_i \psi_i^*(r)\psi_i(r) \tag{3.2.2}$$

The result of the first theorem is that the ground state electron density uniquely determines all properties of the ground state of the system. Furthermore, this means that finding the ground state electron density results in finding the overall ground state energy and thereby solving the Schrödinger equation. Consequently, each electron wave function can then be solved separately as a function of three spatial variables with the following Hamiltonian operator:

$$\hat{H}_e = \hat{K}_e + \hat{V}_{n,e} + \hat{V}_{\rho,e} \tag{3.2.3}$$

Where $\hat{V}_{\rho,e}$ describes the potential between the electron and the electron density. As a result, the problem gets reduced from a 3N dimensional problem to many(N) 3 dimensional problem, where N is the number of electrons. The second theorem states that: *The electron density that minimizes the energy of the overall functional is the true electron density corresponding to the full solution of the Schrödinger equation.* This means that solving Schrödinger's equation can be done by finding the electron density that minimizes the overall functional. However, the energy functional is not known and is often expressed as a sum of a known part and an unknown part:

$$E\left[\{\psi_i\}\right] = E_{known}\left[\{\psi_i\}\right] + E_{XC}\left[\{\psi_i\}\right] \tag{3.2.4}$$

The unknown part, $E_{XC}[\{\psi_i\}]$, is called the exchange correlation functional. It includes all quantum mechanical effects that are not known and needs to be approximated. There excist several different types of approximations and two of them are the *Local Density Approximation* (LDA) and *Generalized Gradient Approximation* (GGA). Two examples of commonly used GGA functionals are the *Perdew-Wang functional* (PW91) and the

Perdew-Burke-Ernzerhof functional (PBE). As a result of all of these approximations, the Schrödinger equation for a single electron wave function can now be expressed as:

$$\left[\hat{K}_e + \hat{V}_{n,e} + \hat{V}_{\rho,e} + \hat{V}_{XC}\right] \psi_i(r) = \varepsilon_i \psi_i(r) \tag{3.2.5}$$

The set of single electron wave functions is called the Kohn-Sham equations. Solving this set of equations will yield the ground state electron density, thus also the true ground state energy of wave function describing the system. To solve the Kohn-Sham equations the potential between the electrons and the electron density, $\hat{V}_{\rho,e}$, needs to be found. This potential is dependent on the electron density, $\rho(r)$, which unfortunately is dependent on the set of single electron wave functions, see equation 3.2.2. Therefore, to solve the set of single electron wave functions the Kohn-Sham scheme can be used [51], see Figure 3.1.

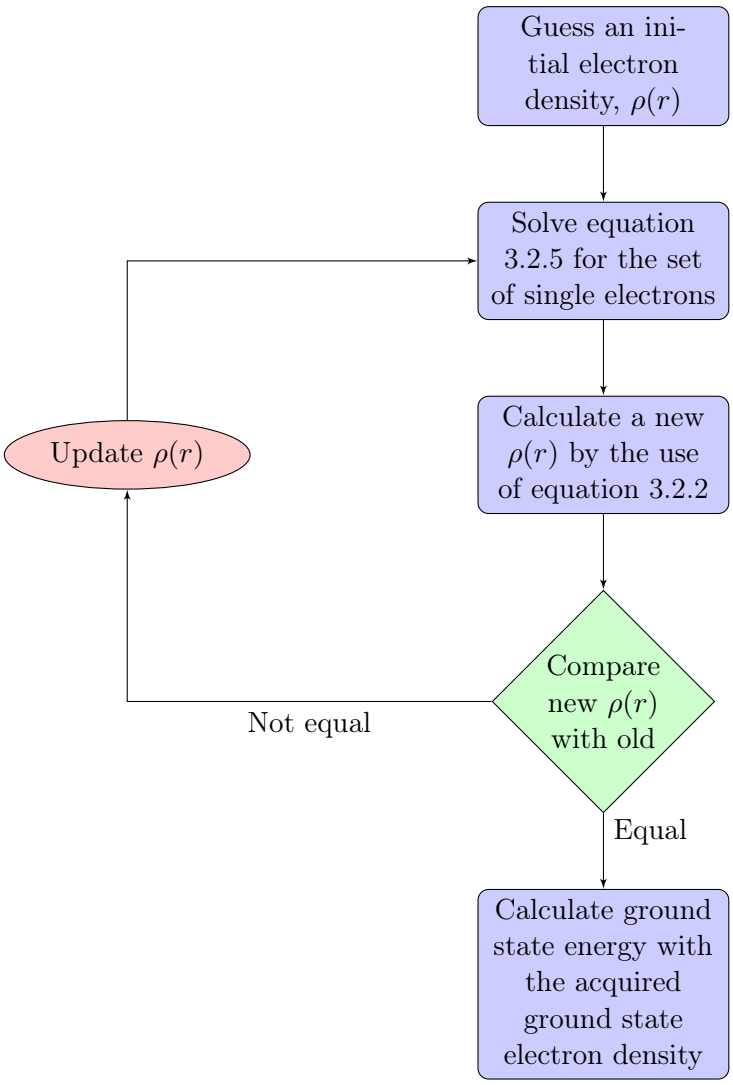

Figure 3.1: Kohn Shame scheme [51]. $\rho(r)$ is the electron density

To initialize the calculation, a guess at the electron density is needed. Thereafter, the set of single electron wave functions is solved and a new electron density calculated. Then the guessed electron density is compared to the calculated electron density. If they are not equal, the new electron density is then used to recalculate and solve the set of single

electron wave functions and thereafter finding a new electron density. This is repeated until the electron density used as input is the same as the one calculated form the solution to the set of single electron wave functions. If they are equal, the ground state electron density is found and the calculations can proceed to calculate the the ground state energy of the wave function describing the system.

3.3 Nudged Elastic Band

Nudged Elastic Band or NEB is a method developed to find and investigate the minimum energy path for a transition between an initial and a final state [52]. The NEB method is in the material science community commonly used to look at vacancy diffusion in metals and alloys, as well as to investigate ionic diffusion in membrane, cathode and electrolyte materials. Conducting NEB calculations consists of three main steps. Firstly, a start and an end structure needs to be defined and relaxed. Secondly, structures/images in between the start and end points needs to be generated and this is commonly done by the use of linear interpolation. See Section B for more information about how these structures are generated in this project. Lastly, a NEB algorithm is used to compute and find the lowest energy path [53]. In this project climbing image NEB is used and this method is just a small modification of the regular NEB method. After a couple of iterations of the regular NEB method, thus gaining information about the shape of the minimum energy path, the "climbing" structure is moved up the energy profile in order to get high precision at the saddle point. As a result, NEB calculations will give more precise estimations of migration barriers [54]. The NEB calculation can be conducted with several different optimizers [55]. A couple of them are discussed more in detail in Section A. Thereafter, the results can be used to find the migration barrier for the minimum energy path found.

3.4 VASP

VASP or "The Vienna *Ab-Initio* Simulation Package" is the software used for all DFT calculations in this project [56, 57, 58, 59]. Examples of some of the input files needed for conducting DFT calculations using VASP are displayed in Section G. For more information about VASP visit the VASP-wiki.

4 Computational Method

In this project all DFT calculations were performed using Fram, a supercomputer provided by UNINETT Sigma2 - the National Infrastructure for High Performance Computing and Data Storage in Norway. All other calculations were done using the python library `PYMATGEN` together with python scripts written by people involved in this project. A description of the script developed to find interstitial and interstitialcy paths can be found in Section F.4. All DFT calculations were performed using VASP with the PBEsol functional [60] and a plane wave cut-off energy of 600 eV, see Section C for the convergence testing of the tetragonal LLZO structure.

4.1 Migration Barriers

All calculations concerning migration barriers in this project were performed using gamma point relaxation. This includes both relaxation of start and end structures as well as the NEB calculations. 1x1x1 was used as kpoints and listing G.6 displays the `KPOINTS` file used.

4.1.1 Vacancy Diffusion

Distinct paths between Li ions in the tetragonal LLZO structure were found using the `pymatgen.analysis.path_finder` [53]. More information about the script can be found in Section F.1. Two paths were found (shown in Figure 5.1 and 5.2 in the results section) and were used to construct start and end structures for both paths. After these structures were relaxed, five structures in between the start and end points were generated by interpolation also using `pymatgen`. See Section B for more information about how these structures were made. The generated structures were then, together with the start and end points, used in NEB calculations. After these calculations were finished, total cell energy were plotted relative to the energy of the structure describing the initial structure, as a function of distance traveled by the Li ion. These plots are displayed in Section 5.1.1.

In addition, after visual investigation of the tetragonal LLZO structure, another vacancy path were added to the calculations. As seen in Figure 5.1 and 5.2, vacancy path 1 are from a Li^{tet} site to a distorted Li^{oct} site, while path 2 are from a Li^{oct} site to a distorted Li^{oct} site. Furthermore, both the Li^{tet} sites and Li^{oct} sites in the tetragonal LLZO structure are surrounded by distorted Li^{oct} sites. Therefore, it is also possible to have an unique Li vacancy path going from a distorted Li^{oct} site to another distorted Li^{oct} site. Calculations were therefore also performed on the vacancy path shown in Figure 5.3.

4.1.2 Interstitial Diffusion

To find and define the possible interstitial paths in the LLZO structure, all the interstitial sites needed to be found. Several different methods were tested to find the interstitial sites, but due to the large and complicated nature of the LLZO structure, all of the methods found several hundred possible sites. Many of these sites were situated almost on top of

each other or almost on the top of lattice sites, and could therefore be eliminated. After filtering the sites by removing all interstitials closer than 1 Å to either another interstitial site or a lattice site, there were still too many possible interstitial sites left. Figure F.1 in the appendix displays the LLZO structure with all the possible interstitial sites received from `PYMATGEN`s `VoronoiInterstitialGenerator`. This interstitial generator is based on simple Voronoi analysis and more information about the script can be found in Section F.2. To try to resolve the issue with too many interstitial sites generated, `PYMATGEN`s `ChargeDensityAnalyzer` was tested. Instead of using the LLZOs structure as an input, this method uses the structures charge density instead. All the minimums in the charge density were recognised as possible interstitial sites and the total amount of possible sites were reduced by a large number, see Figure F.2. See Section F.3 for more information about the `ChargeDensityAnalyzer`. Some of these proposed interstitial sites were also situated to close to each other or lattice sites, and for this reason, these interstitial sites were filtered and removed with the same criteria as above.

After obtaining all the possible interstitial sites, `pymatgen.analysis.path_finder` [53] was used to find the distinct paths between them. In spite of all the effort to reduce the number of possible interstitial paths, there were still a large number of possible paths found by the script. Because vacancy diffusion is recognised as the major contributor to Li transport in LLZO, it is essential to look at the best possible scenario for interstitial diffusion. This is important in order to be able to evaluate if the interstitial mechanism will contribute to the overall Li ion conductivity. With a poor result from these calculations, interstitial diffusion can be disregarded as a transport mechanism and with a great result, more paths needs to be investigated. Therefore, the script was modified to return the three paths with the largest free radius around the path. These paths would hopefully give the interstitial transport mechanism the best possible opportunity to succeed. The three paths are shown in Figure 5.5, 5.6 and 5.7 in the results section. The start and end structures, of the three paths, were relaxed and structures in between were constructed in a similar fashion as for the vacancy diffusion. Thereafter, the NEB calculations were started and after relaxation, the relative energies were plotted.

4.1.3 Interstitialcy Diffusion

Finding interstitialcy paths also require knowledge about the interstitial positions in the structure. The interstitial sites found earlier were therefore also used to find and generate interstitialcy paths. To generate the interstitialcy paths, all the interstitials sites were added to the structure and then neighbors to all the unique Li lattice position were evaluated. A path were found if the Li site had two or more neighbors that were interstitials and could make an interstitialcy path with an angle of more than 90°. Thereafter, equivalent paths were removed after the following criteria. Firstly, if two paths have the same lattice Li and if the ions in interstitial positions are periodic images of each other. Secondly, if the paths had the same lattice Li as well as equal total distance and angle.

Similarly as for the interstitial paths, there were still many interstitialcy paths left after all the filters had been applied. Therefore, the three paths with the angle closest to 180°were chosen for the NEB calculations. This was done to give the interstitialcy diffusion mechanism the best possible opportunity to show low migration barriers because of the same reasoning as for interstitial diffusion. Figure 5.9, 5.10 and 5.11 show the chosen paths. Start end and structures were again generated, relaxed and used to make the structures for the NEB calculations. After relaxation of the NEB calculations, the energies were plotted and are displayed in Figure 5.12.

4.1.4 Migration Barriers for Vacancy Diffusion with Additional Point Defects

Migration barriers for vacancy diffusion in the presence of point defects have also been investigated. A selection of low energy defects were added to structures close to the moving Li ion. The formation energies of these defects were calculated during a previous project [8] and are displayed in Table 4.1. For instance for the $Nb_{Zr}^{\bullet}$ defect, a Zr ion close to the vacancy path was replaced by a Nb ion. This structure is shown in Figure 5.13. Thereafter, the start and end structures were relaxed and used in new NEB calculations. The calculated lowest energy paths for vacancy path 1 and 2 with additional defects can be found in Figure 5.14 and 5.15.

Table 4.1: Formation energies of a selection of low energy defects in both O poor/metal rich and O rich/metal poor environments [8]

Defects	Oxygen poor/Metal rich	Oxygen rich/Metal poor
$O_i^{''}$	3.303 eV	0.413 eV
$V_O^{\bullet\bullet}$	1.134 eV	7.570 eV
$Li_i^{\bullet}$	0.512 eV	3.384 eV
$Al_{Li^{tet}}^{\bullet\bullet}$	0.907 eV	0.618 eV
$Nb_{Zr}^{\bullet}$	2.240 eV	0.138 eV
Y_{La}^{x}	0.483 eV	0.483 eV
$Y_{Zr}^{'}$	0.804 eV	0.679 eV

4.1.5 Migration Barriers with a Localised Hole or Electron

Previously it was found that the Fermi level is pinned mid-gap, as can be seen in Appendix Figure E.1. The LLZO structure was also found to have a large band gap, see Figure D.1, and these results indicates that the structure is a bad conductor of both holes and electrons. The PBEsol functional is a standard density functional which is known for not localising electrons or holes correctly and therefore producing incorrect results for structures where this is important. Consequently, calculations with forced localisation of donated electrons or holes were carried out in order to solve this issue and investigate how the additional electrostatic effects would influence the migration barriers of $V_{Li}^{'}$ in LLZO. The defect $Y_{Zr}^{'}$ was chosen to test the effect of localised holes and $Nb_{Zr}^{\bullet}$ was chosen to test the effect of localised electrons. Vacancy path 1 and 2 were used as test paths. Equation 4.1.1 and 4.1.2 are showing the need for charge compensation by an electron or a hole, respectively.

$$\frac{1}{2}Nb_2O_5 \xrightarrow{ZrO_2} Nb_{Zr}^{\bullet} + e^{'} + \frac{5}{2}O_O^x \tag{4.1.1}$$

$$\frac{1}{2}Y_2O_3 \xrightarrow{ZrO_2} Y_{Zr}^{'} + h^{\bullet} + \frac{3}{2}O_O^x \tag{4.1.2}$$

To find where to place the extra hole or electron, the density of states was investigated and Figure D.2 displays the calculated density of states for the undoped LLZO structure. The figure clearly shows that the upper part of the valence band is mostly O p orbitals and thus it can be rationalised that the hole will be localised on an O 2p orbital. Y is not a part of the density of state plot and was therefore also considered a candidate for

the localised hole. Similar evaluations for the $Nb_{Zr}^{\bullet}$ were also made. Nb has known to incorporate as Nb^{4+} in wide band gap metal oxides such as SnO_2 [61] and the lower part of the conduction band shows some mixing of the O p and La d orbitals. Therefore, the Nb ion in addition to a La and an O ion close to the defect were recognised as possible sites for the extra electron.

In order to try to set up calculations where an electron or a hole is localised on an ion, the magnetic moments of the ions were used. The magnetic moments were calculated by equation 4.1.3, where n is the number of unpaired electrons. For all of the ions with a localised hole or electron the number of unpaired electrons is 1 and the magnetic moment will therefore be $\sqrt{3}$. Ions with no unpaired electrons will have a magnetic moment of 0. These magnetic moments were specified in the `INCAR` file with the `MAGMOM` tag.

$$\text{Magnetic Moment} = \sqrt{n(n+2)} = \sqrt{1(1+2)} = \sqrt{3} \tag{4.1.3}$$

In total, to test localisation of electrons, six systems were investigated. The extra electron was placed on either a Nb, O or La ion for both vacancy path 1 and 2. Four systems were conducted to test the localisation of holes. In these calculations the hole was situated on either the Y ion or an O ion close to the defect.

4.2 Ionic Conductivity

Ionic conductivity for the all the different variations of the LLZO structure were calculated using equation 2.4.3. The diffusion prefactor, $D_0 = 7.056 \cdot 10^{-10}\ \frac{\text{m}^2}{\text{s}}$, was taken from "Ab initio molecular dynamics study of lithium diffusion in tetragonal $Li_7La_3Zr_2O_{12}$" by B. Andriyevsky et al. [62]. In their article the diffusion coefficient for tetragonal LLZO in ambient temperature (300 K) was estimated to be around $D = 0.64 \cdot 10^{-15}\ \frac{\text{m}^2}{\text{s}}$. Thereafter, they used this value to calculate a migration barrier of $E_a = 0.36$ eV. To find an estimation of the diffusion prefactor for tetragonal LLZO, equation 2.4.2 together with the migration energy and diffusion coefficient taken from B. Andriyevsky et al., was used as shown in equation 4.2.1. k_B is the Boltzmann constant, T is the temperature and D_0 is the diffusion prefactor.

$$D_0 = \frac{D}{\exp\left(-\frac{E_a}{k_B T}\right)} = \frac{0.64 \cdot 10^{-15}\,\frac{\text{m}^2}{\text{s}}}{\exp\left(-\frac{0.36\text{eV}}{1.38 \cdot 10^{-23}\,\frac{\text{J}}{\text{K}} \cdot 300\text{K}}\right)} = 7.056 \cdot 10^{-10}\ \frac{\text{m}^2}{\text{s}} \tag{4.2.1}$$

4.2.1 Vacancy Conductivity

To calculate an estimation of ionic conductivity contribution from vacancy movement, charge carrier densities found and presented in previous work [8] were used together with the harmonic average of the migration barriers calculated during this project. The harmonic average of the migration barriers for the undoped structure was calculated from the migration barriers of vacancy path 1 and 2 with and without native defect. For the doped structures, the defects with the respective dopant were also included in the harmonic average migration barrier. The calculated harmonic averages used to estimate the ionic conductivities are shown in Table 5.5. To calculated vacancy ionic conductivity, the

V'_{Li} densities presented in Table 4.2 are used as charge carrier densities and the results are presented in Figure 5.18.

Table 4.2: V'_{Li} and $Li_i^{\bullet}$ concentrations with different sintering environments used to calculate ionic conductivities [8]

	Oxygen poor/metal rich		Oxygen rich/metal poor	
Dopant	V'_{Li} [cm^{-3}]	$Li_i^{\bullet}$ [cm^{-3}]	V'_{Li} [cm^{-3}]	$Li_i^{\bullet}$ [cm^{-3}]
Undoped	$6.05 \cdot 10^{19}$	$6.08 \cdot 10^{19}$	$1.68 \cdot 10^{20}$	$2.56 \cdot 10^{19}$
Al-doped	$6.35 \cdot 10^{19}$	$5.79 \cdot 10^{19}$	$1.98 \cdot 10^{20}$	$1.91 \cdot 10^{19}$
Nb-doped	$6.05 \cdot 10^{19}$	$6.08 \cdot 10^{19}$	$1.26 \cdot 10^{21}$	$2.93 \cdot 10^{18}$
Y-doped	$5.74 \cdot 10^{19}$	$6.41 \cdot 10^{19}$	$1.60 \cdot 10^{20}$	$2.38 \cdot 10^{19}$

4.2.2 Interstitialcy Conductivity

Ionic conductivity from interstitialcy diffusion have also been estimated. The migration barrier used for this calculation was the harmonic average of migration barriers for interstitialcy path 1 and 3 and the calculation of the harmonic barrier is shown in equation 4.2.2.

$$E_m = \left(\frac{0.421^{-1} + 0.194^{-1}}{2} \right)^{-1} \text{eV} = 0.266 \text{ eV} \tag{4.2.2}$$

The density of $Li_i^{\bullet}$ was used as charge carrier densities for predicting the contribution from interstitialcy diffusion. The calculated ionic conductivities are displayed in Figure 5.19.

5 Results

5.1 Migration Barriers

In this section many of the figures are used to display calculated lowest energy paths. To make these figures, all the energies are normalized to the energy of the initial structures. In other words, the total energy of the initial structure is subtracted from all of the energies of the structures in the NEB calculation. Thereafter, these energies are plotted as a function of the distance the Li ion has moved.

5.1.1 Vacancy Diffusion

Figure 5.1 and 5.2 display the two vacancy paths found by the use of `PYMATGEN`'s `PATHFINDER`. In path 1 the Li ion is moving from a tetrahedral site to a distorted octahedral site and in path 2 the Li ion is moving from a octahedral site to a distorted octahedral site. Figure 5.3 displays the third distinct path where the Li ion is moving from a distorted octahedral site to another distorted octahedral site. The path lengths are also displayed in the figures and are 2.6, 2.6 and 2.7 Å, respectively.

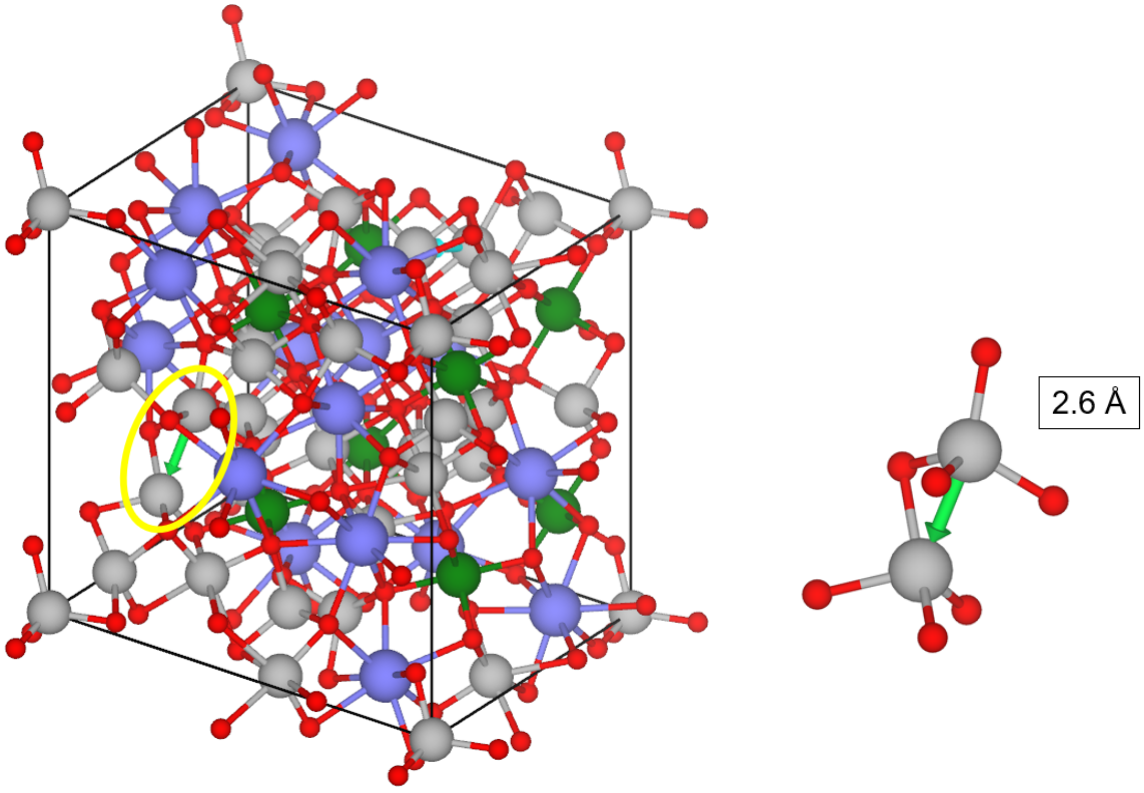

(a) (b)

Figure 5.1: Distinct vacancy path 1 visualized by the use of `VESTA`

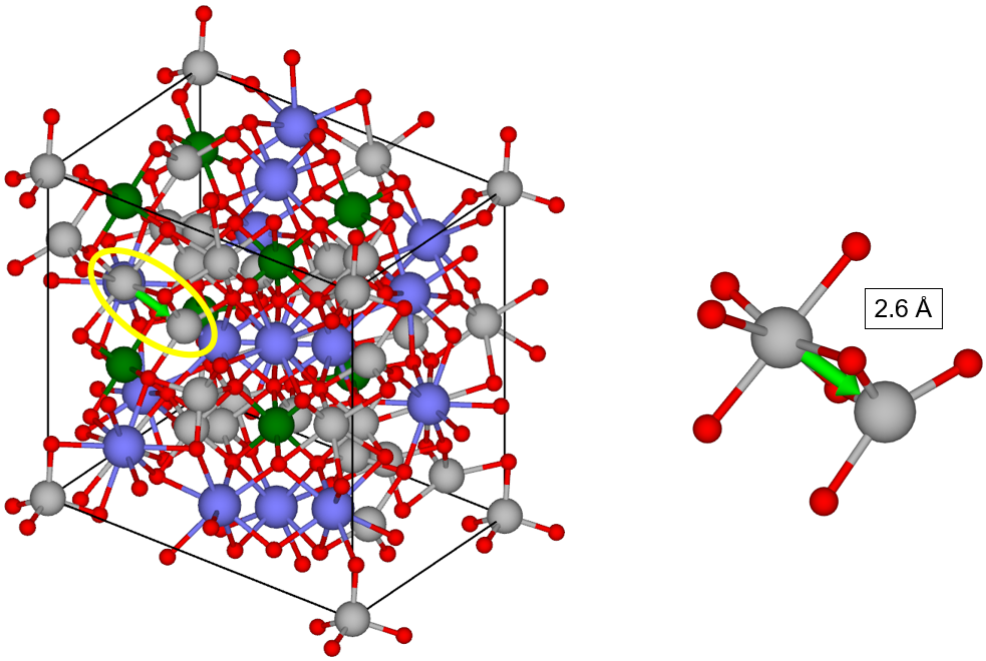

(a) (b)

Figure 5.2: Distinct vacancy path 2 visualized by the use of `VESTA`

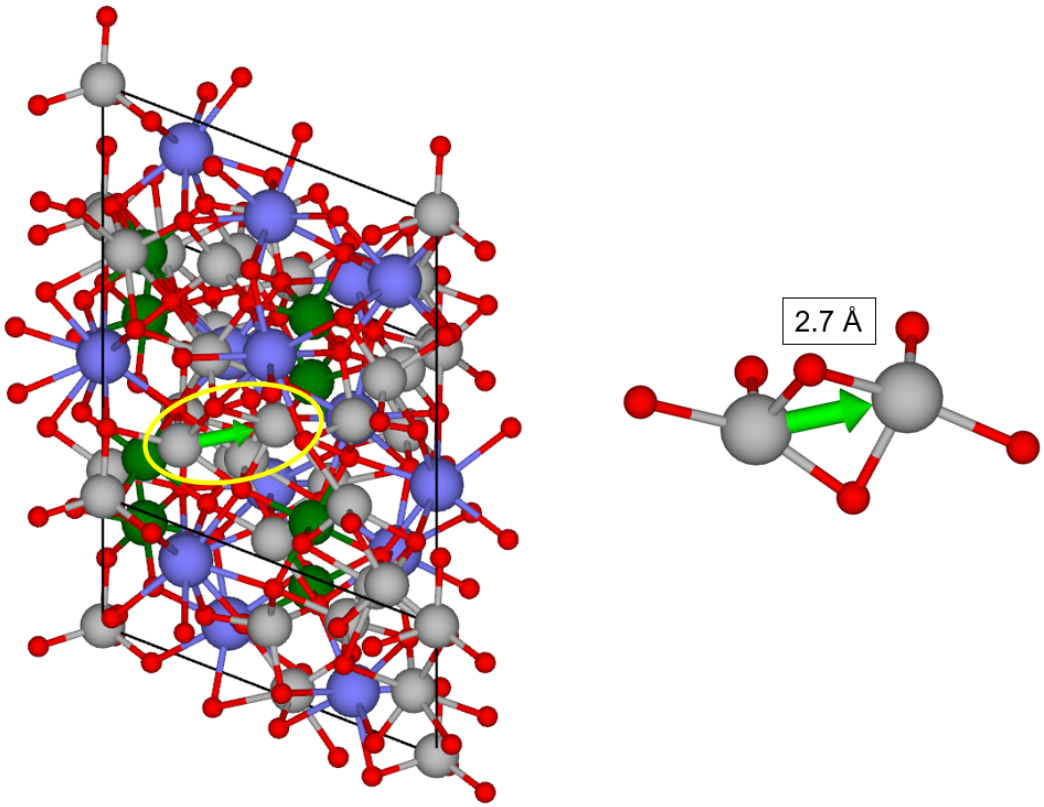

(a) (b)

Figure 5.3: Distinct vacancy path 3 visualized by the use of `VESTA`

Figure 5.4 shows the lowest energy paths, for three different vacancy paths, found by NEB calculations. Path 1 and 2 show very low migration energies, while path 3 shows a higher migration barrier of about twice the energy of path 1 and 2. The migration barriers found for the three different paths are displayed in Table 5.1 and they are all very low compared to experimental values 0.3 eV for the cubic structure [37]. Vacancy path 1 shows the largest difference in energy between the start and end structure, and some reduction in path length compared to the structure before relaxation. Both path 2 and 3 show very similar energies for the start and end structures. Path 3 shows a double peak with a large valley in the energy profile.

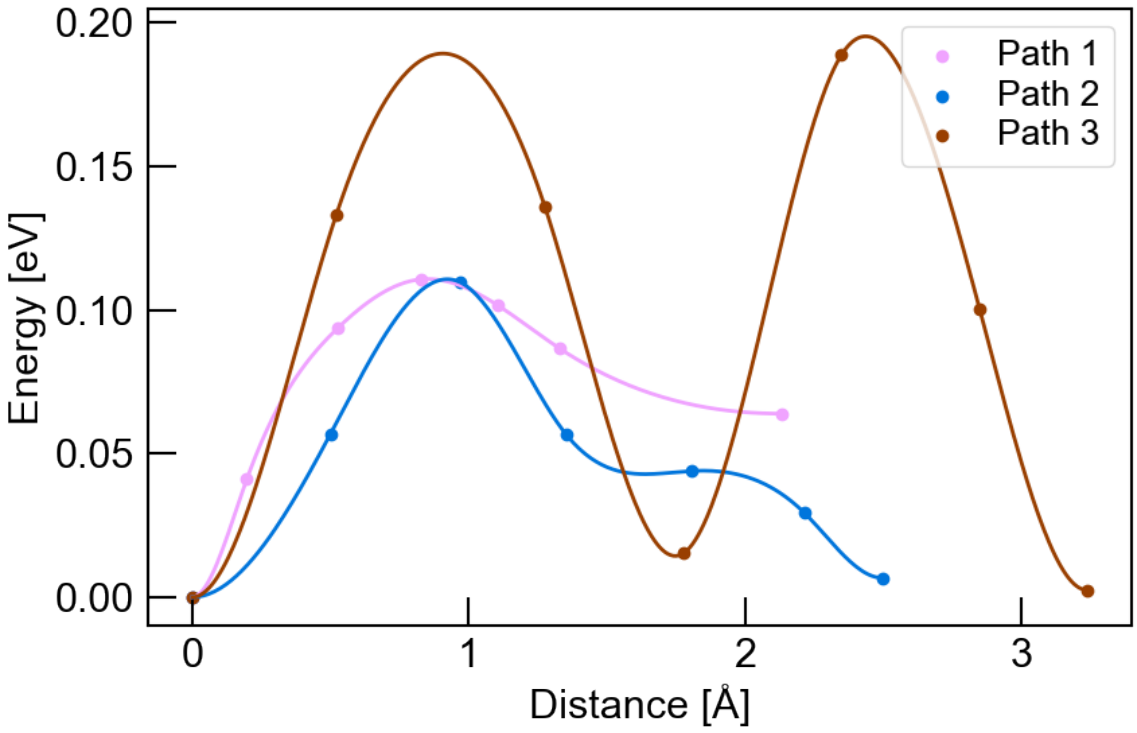

Figure 5.4: Lowest energy paths for vacancy path 1, 2 and 3

Table 5.1: Migration barriers for vacancy path 1, 2 and 3

Defect	Migration Barrier [eV]
Path 1	0.111
Path 2	0.111
Path 3	0.195

5.1.2 Interstitial Diffusion

The following three figures, Figure 5.9, 5.10 and 5.11, show the the three interstitial diffusion paths generated by the python script described in Section F.4. Path 2 is visualised with the help of two unit cells due to the path going over the boundary of the unit cell. The path length of path 1 and 3, 2.9 and 2.7 Å, are very similar to the vacancy paths, while the path length of interstitial path 2, 2.1 Å, is a little shorter.

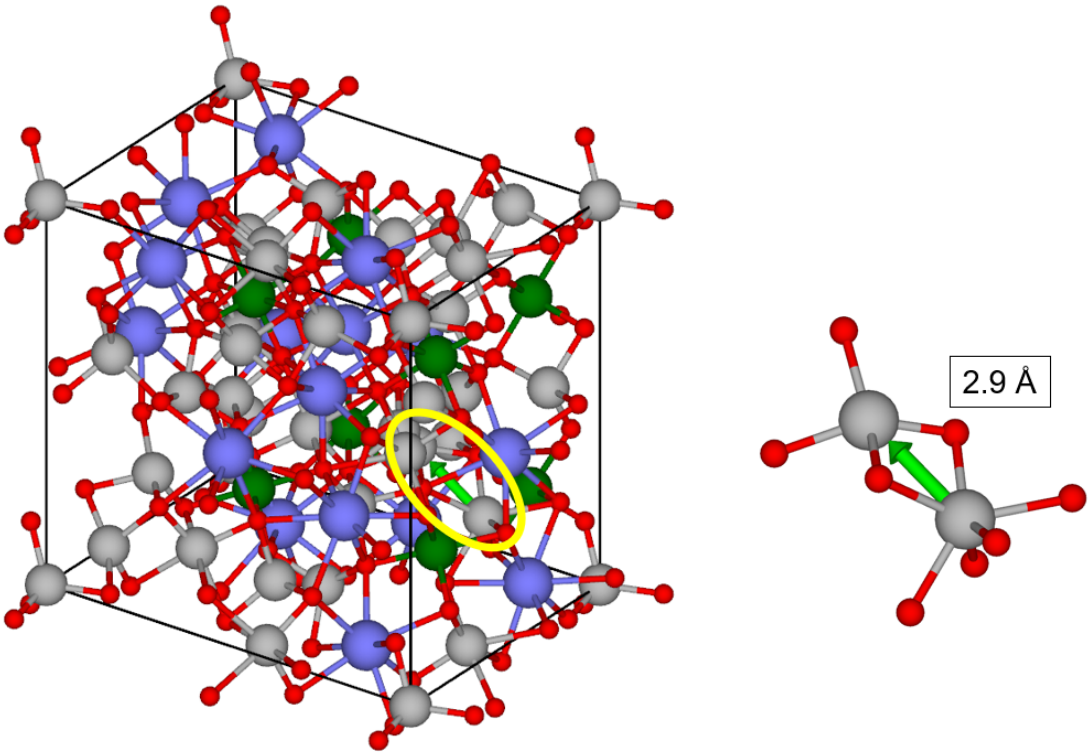

(a) (b)

Figure 5.5: Distinct interstitial path 1 visualized by the use of `VESTA`

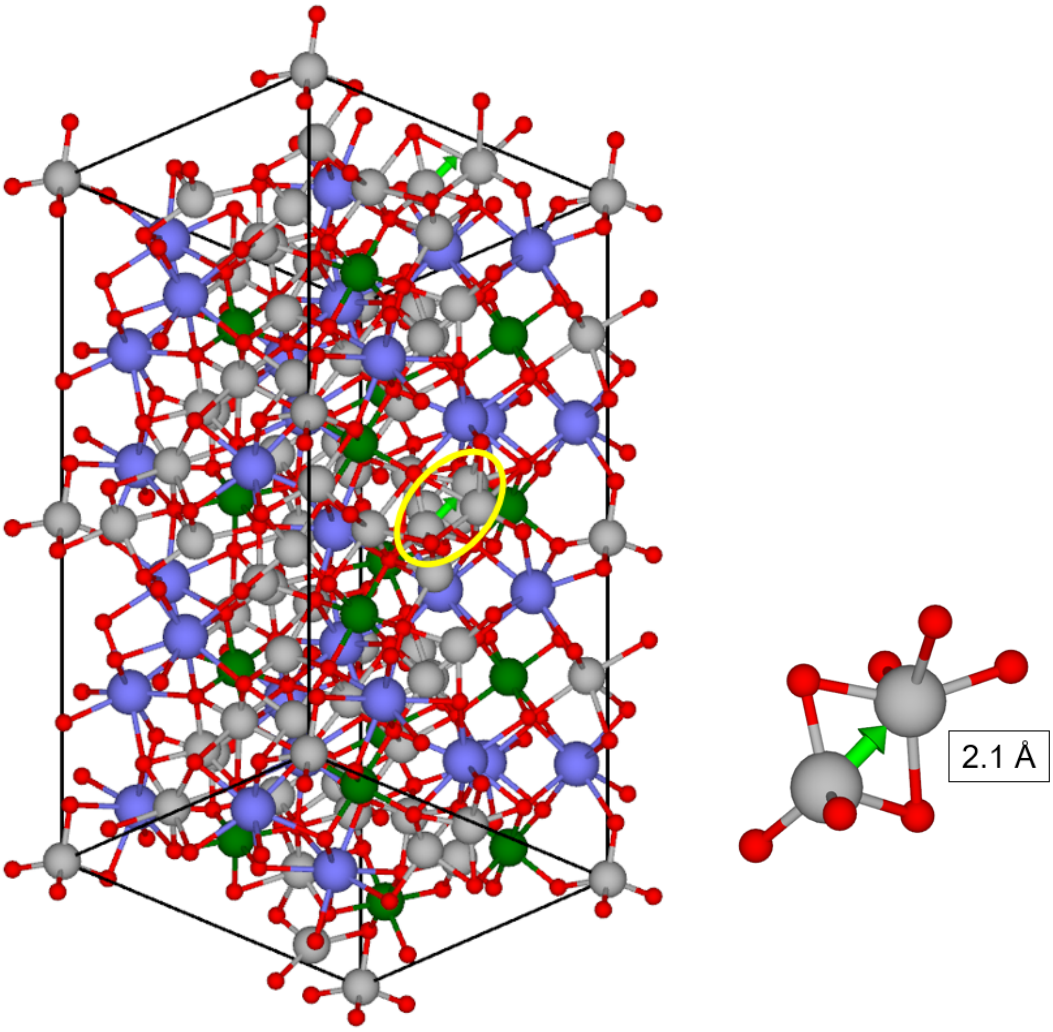

(a) (b)

Figure 5.6: Distinct interstitial path 2 visualized by the use of `VESTA`. Another unit cell was here added to the top easier visualisation of the path.

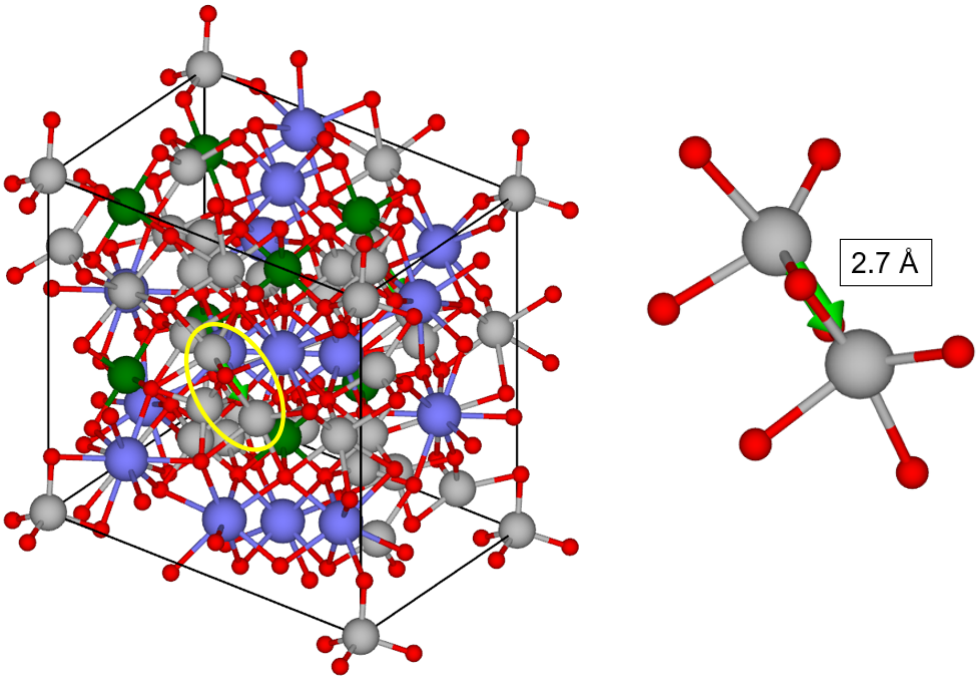

(a) (b)

Figure 5.7: Distinct interstitial path 3 visualized by the use of `VESTA`

Figure 5.8 shows calculated lowest energy paths for interstitial path 1 and 3. During relaxation of the end structure for path 2, the moving Li^+ moved towards its tetrahedral site in the start structure. Therefore, relaxation of the start and end structure resulted in two almost identical structures, thus no path could be made. The other two paths show very large migration energies and a small increase in the path length compared to the generated paths. Table 5.2 shows the calculated migration barriers for the three interstitial diffusion paths. Path 3 shows the largest migration barrier of almost 3 eV, but path 1 shows the largest difference in energy between the start and end structure.

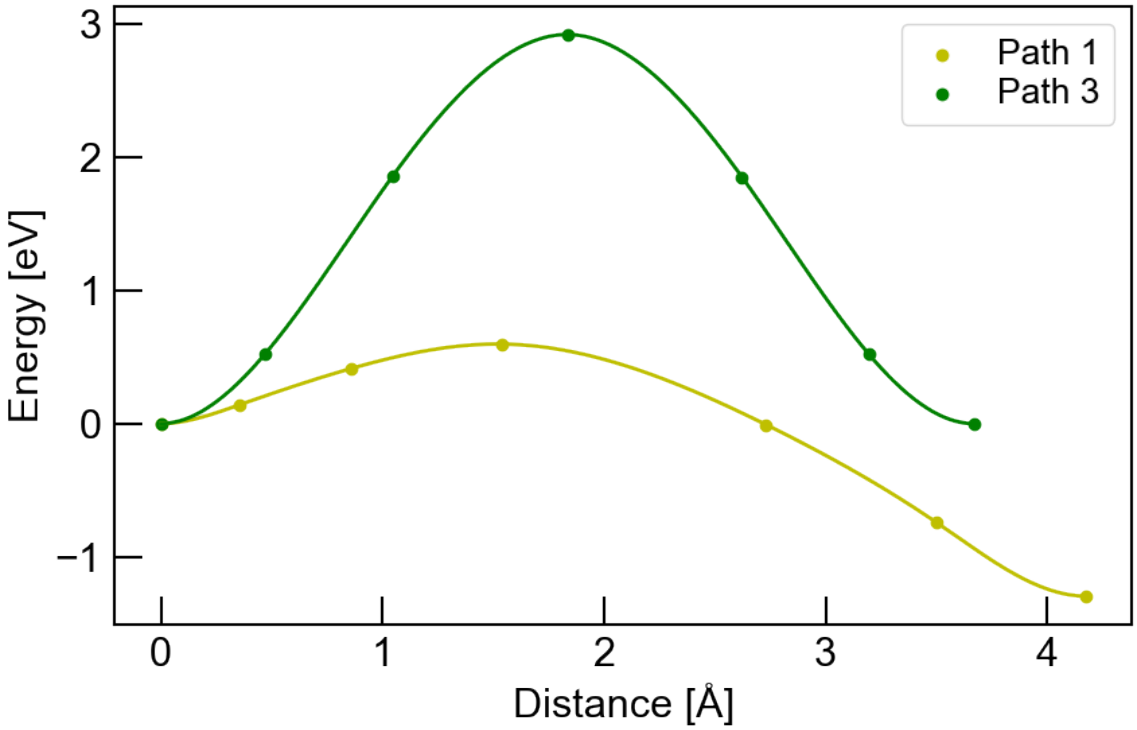

Figure 5.8: Lowest energy paths for interstitial path 1 and 3. Path 2 could not be used for NEB calculations due to the start and end structures relaxing to the same structure.

Table 5.2: Migration barriers for interstitial path 1, 2 and 3

Defect	Migration Barrier [eV]
Path 1	1.892
Path 2	-
Path 3	2.920

5.1.3 Interstitialcy Diffusion

The three generated interstitialcy paths are shown in Figure 5.9, 5.10 and 5.11. The interstititalcy paths consists of a path from an interstitial site to a lattice site and a path from the lattice site to another interstitial site. For Path 1 and 3, the first and second subpath have equal distance, with a length of 1.9 and 2.1 Å, respectively. The first subpath of interstititalcy path 2 is very short, 1.1 Å, and the second subpath is relatively long, 3.1 Å.

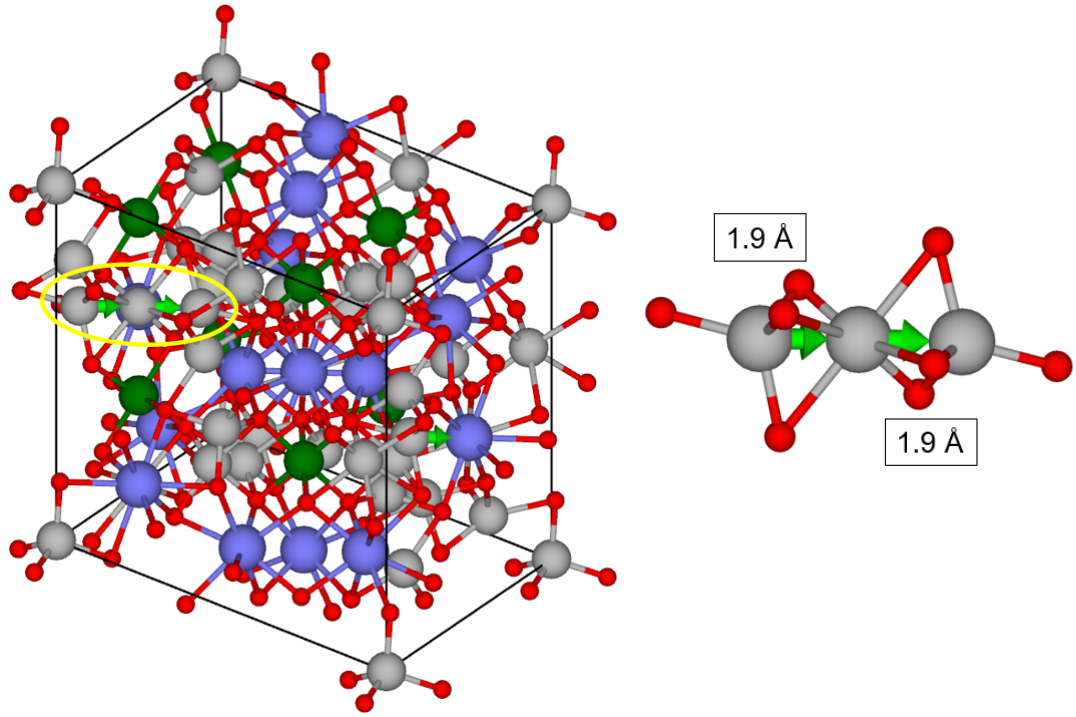

(a) (b)

Figure 5.9: Distinct interstitialcy path 1 visualized by the use of `VESTA`

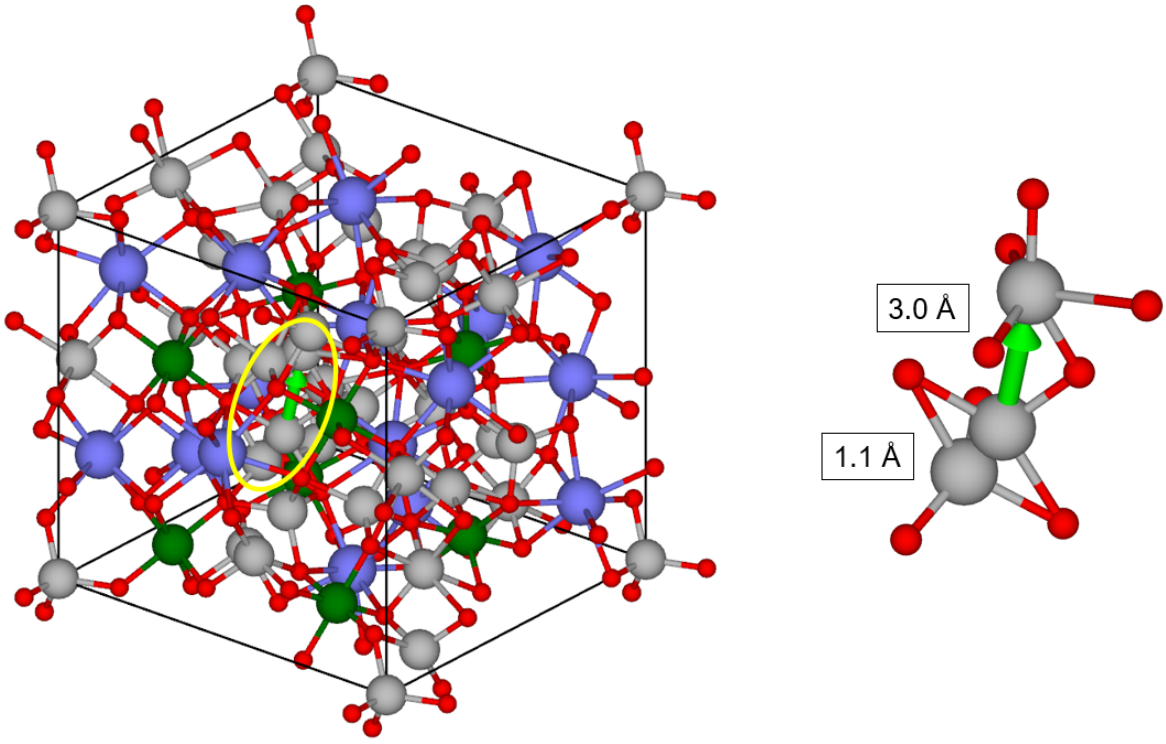

(a) (b)

Figure 5.10: Distinct interstitialcy path 2 visualized by the use of `VESTA`

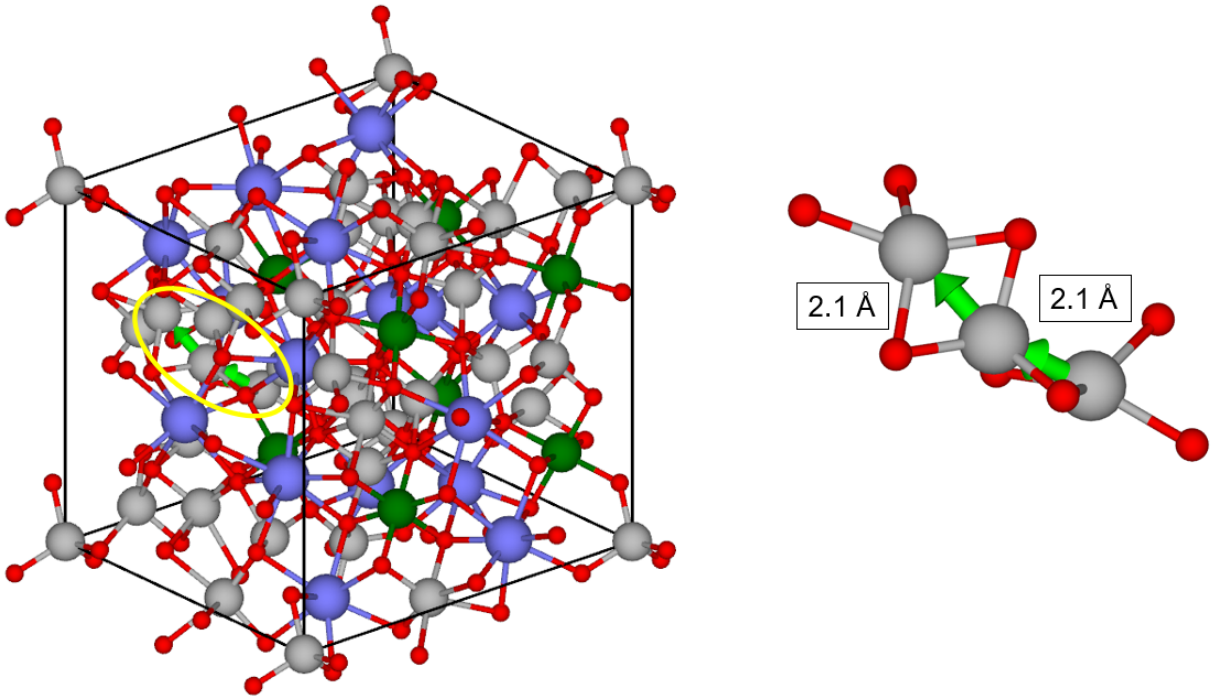

(a) (b)

Figure 5.11: Distinct interstitialcy path 3 visualized by the use of `VESTA`

Figure 5.12 (a) displays the lowest energy paths for three different interstitialcy paths. The x-axis in the plot describes the distance traveled by the Li ion initially situated at the lattice site. Path 2 shows a very large increase in path length and a very high lowest energy path. Both path 1 and 3 show relatively low migration barriers compared to path 2, and Figure 5.12 (b) shows the lowest energy paths without path 2. The migration barriers for the three paths are displayed in Table 5.3. The migration barrier of path 3 is 0.194 eV, 0.227 eV lower than the barrier of path 1. Compared to experimental values, the energy barrier of path 1 is about 0.1 eV higher and path 3 is about 0.1 eV lower, thus only path 3 that is relevant for Li ion conductivity. The start and end of the lowest energy paths for path 1 and 3 are relatively similar, but at a distance of about 0.35 Å, the energy profile of path 3 flattens. This plateau lasts until there is about 0.35 Å left of the path. In contrast, path 1 shows a parabolic energy profile, which is very similar to what was presented in the background section as a typical energy profile. Both paths are symmetrical and show a small reduction in path length.

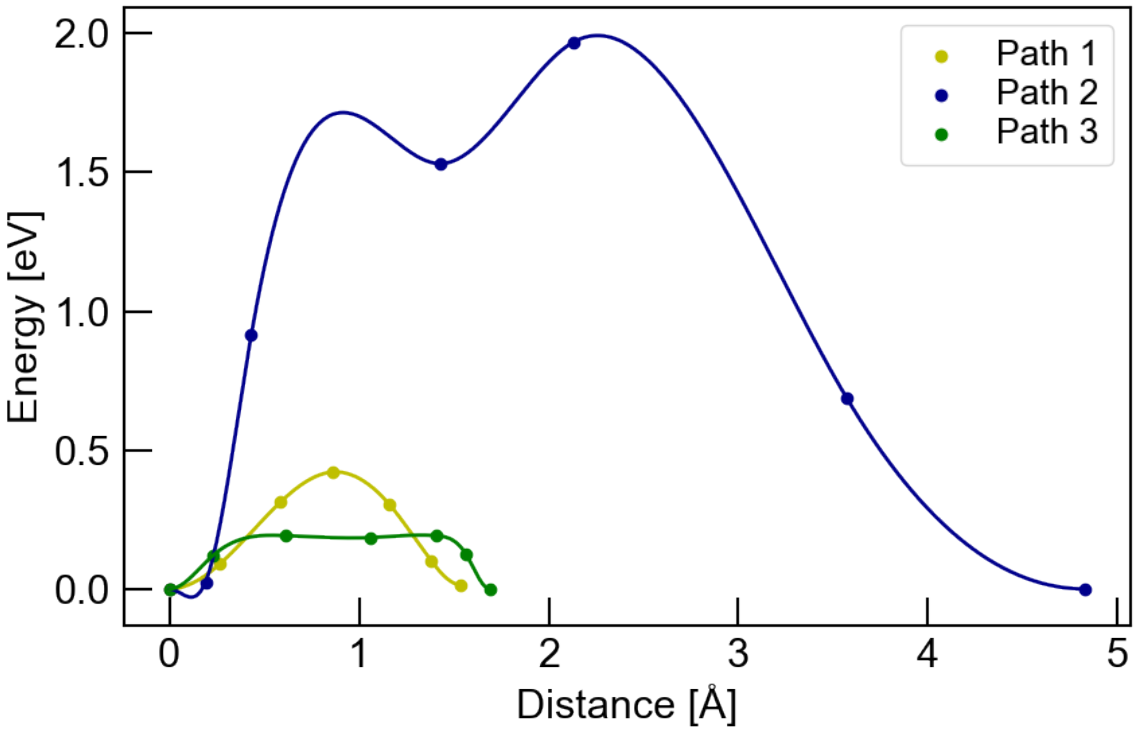

(a)

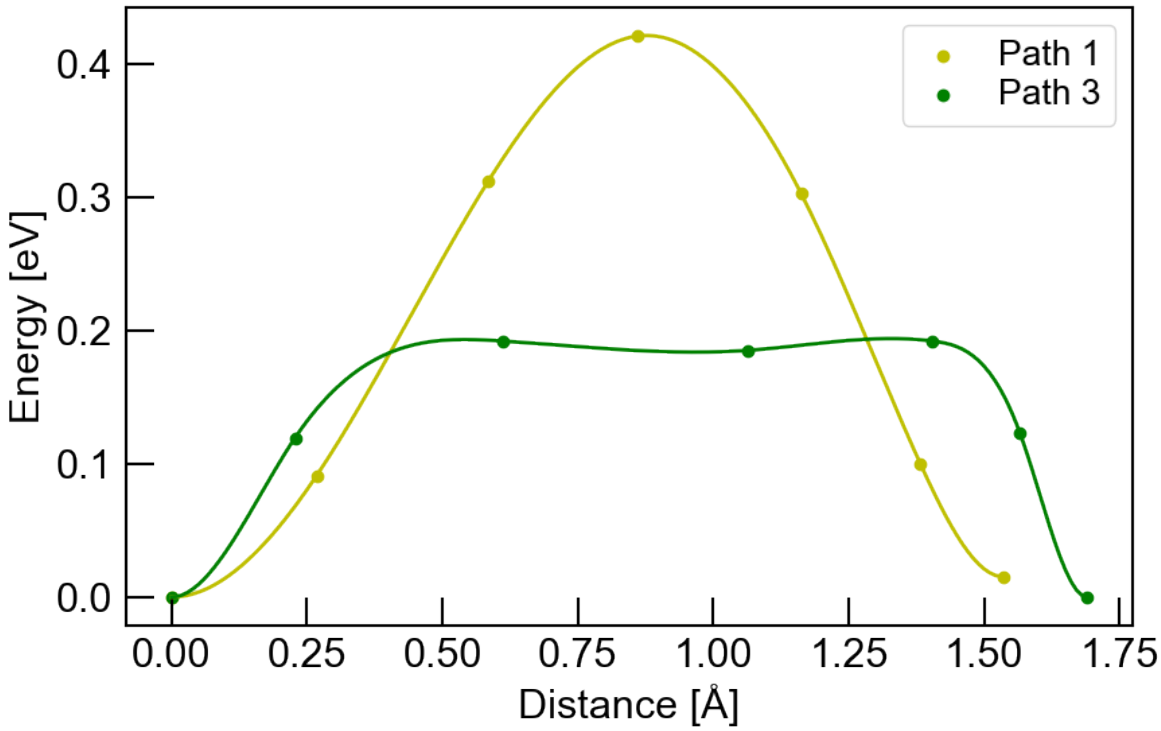

(b)

Figure 5.12: Lowest energy paths for interstitialcy path 1, 2 and 3

Table 5.3: Migration barriers for interstitialcy path 1, 2 and 3

Defect	Migration Barrier [eV]
Path 1	0.421
Path 2	2.022
Path 3	0.194

5.2 Vacancy Diffusion with Additional Point Defects

Figure 5.13 shows an example of vacancy path 1 with an additional defect. The defect in the example is a Nb ion on a Zr site and the other defect structures were made in a similar fashion by adding the defects to the vacancy paths.

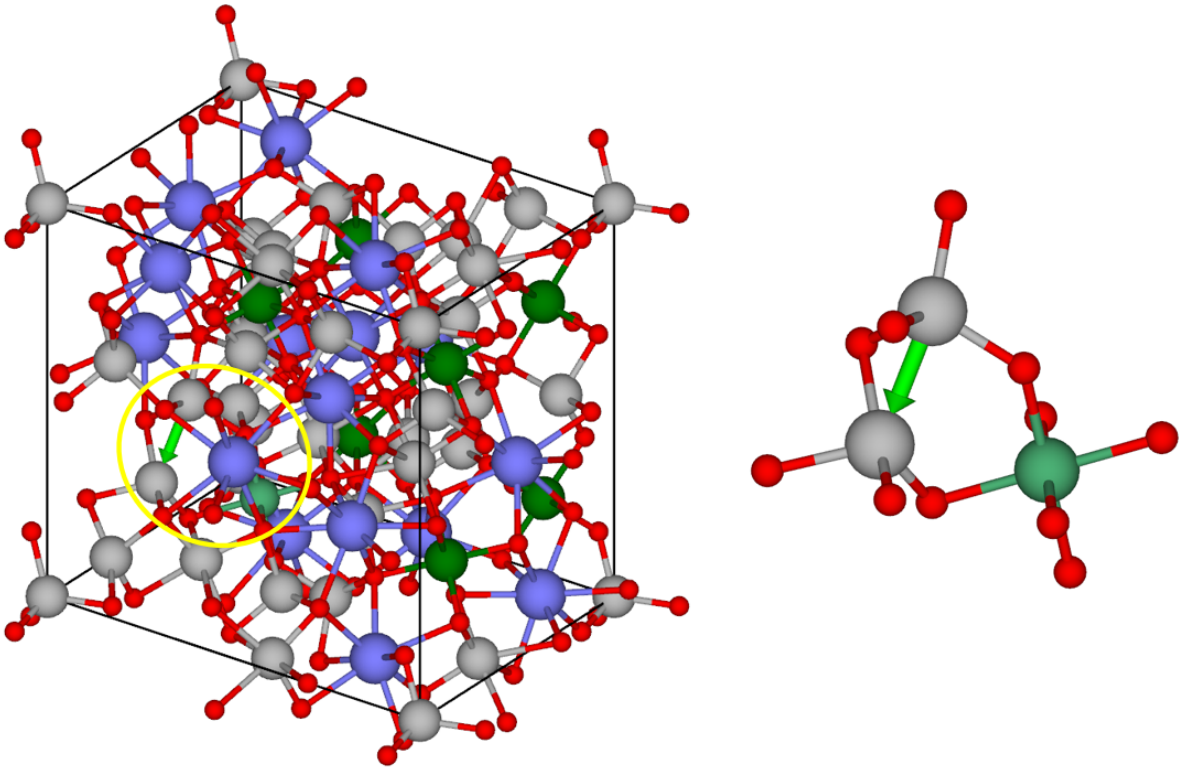

(a) (b)

Figure 5.13: Distinct vacancy path 1 with Nb at Zr site visualized by the use of `VESTA`

Figure 5.14 and 5.15 show the lowest energy paths found by NEB calculations for vacancy path 1 and 2 with additional defects in the structures. The paths labeled with "Standard" describes the path calculated without any extra defects and are also displayed in Figure 5.4. All path 1 calculations, except V_O, show a reduction in the path length. The calculated migration barriers are displayed in Table 5.4 and they mostly show a small increase in energy compared to the standard path. The Y^x_{La} defect shows a large decrease in energy for the end structure compared to the initial structure. The path with the $Al^{\bullet\bullet}_{Li^{tet}}$ defect shows an energy profile which is first decreasing and then increasing for the rest of the path. In addition, this path shows a large reduction in path length. The results from the NEB calculation with the O_i'' defect is not displayed in the figure. The calculation yielded

a set of structures where the moving Li^+ relaxed towards ether the start or end position, thus resulting in x values very close to the 0 or 1.7 Å. Therefore, the energies found by NEB calculations, were not suitable for fitting with polynomials.

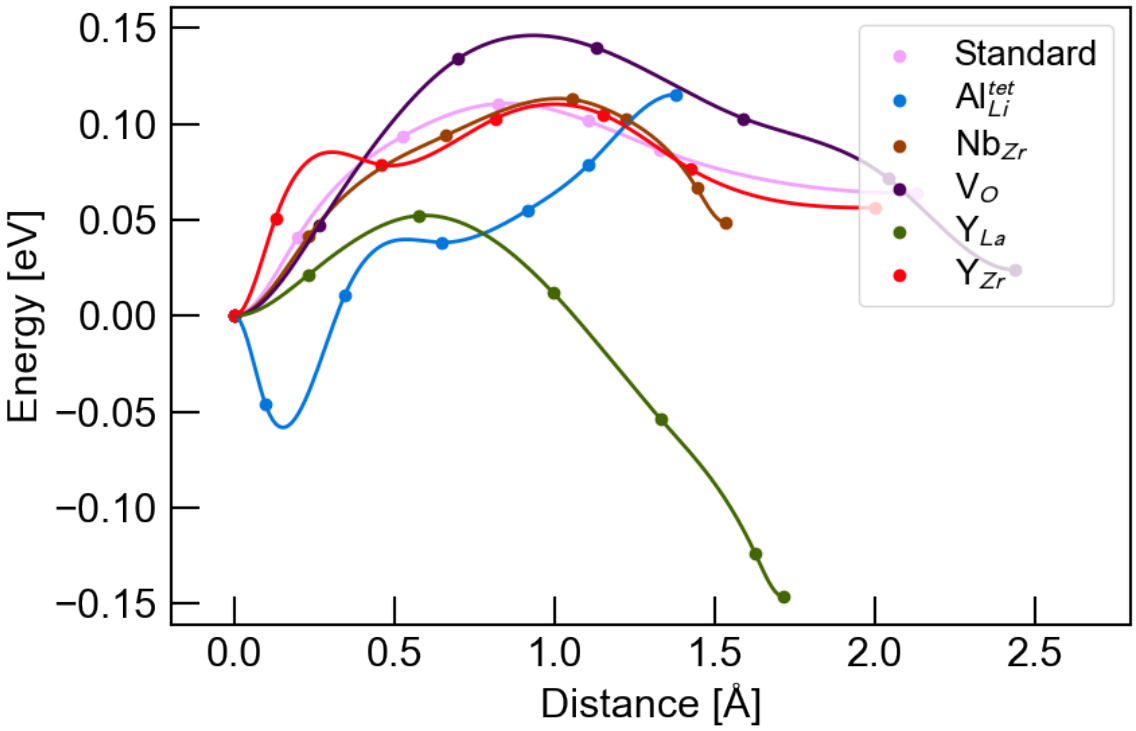

Figure 5.14: Migration barriers for vacancy path 1 with point defects situated close to the moving Li ion.

The calculated lowest energy paths for vacancy path 2 show very similar results regardless of the defect present in the structure. A reduction in relative energy is observed towards the end of all defect paths expect for $O_i^{''}$. $Al_{Li^{tet}}^{\bullet\bullet}$ and $Y_{Zr}^{'}$ show lower energy barriers than the standard and all of other structures show higher migration barriers, with Y_{La}^{x} having the largest barrier of 0.171 eV. The path with the $Al_{Li^{tet}}^{\bullet\bullet}$ defect is the only path that shows a large reduction in path length. In addition, the profile of this path also stands out because of the small valley in the energy profile at the start and end of the path. All of the calculated migration barriers are shown in Table 5.4.

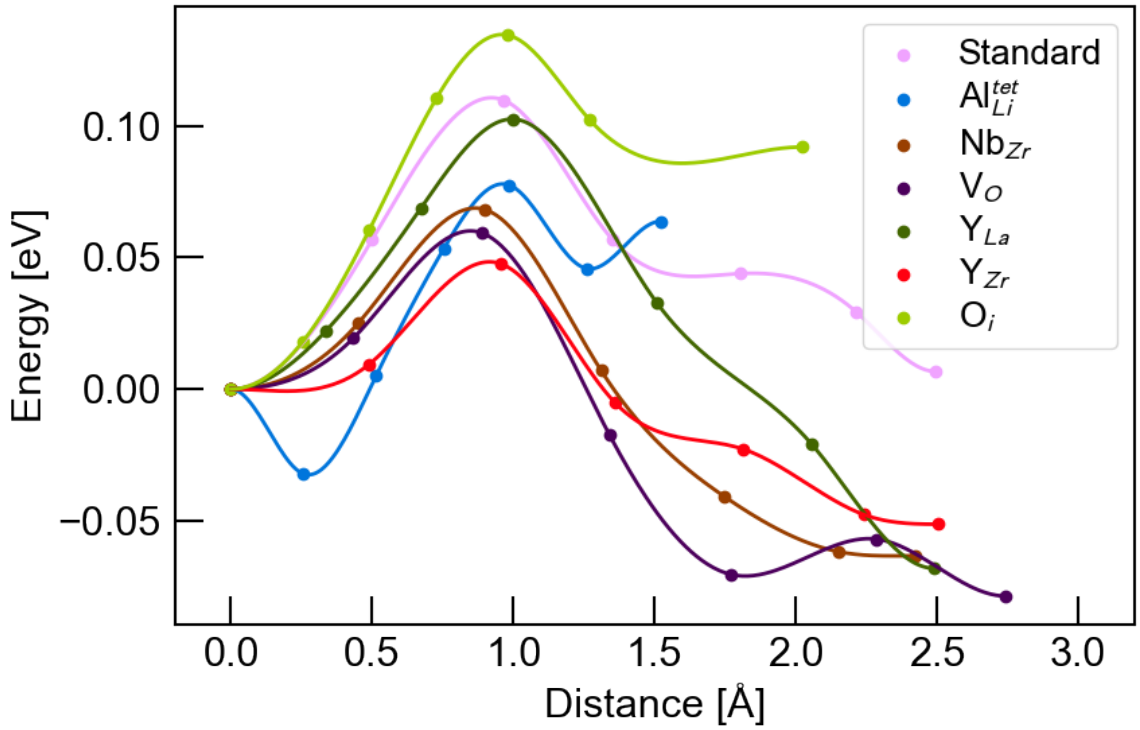

Figure 5.15: Migration barriers for vacancy path 2 with point defects situated close to the moving Li ion

Table 5.4: Calculated migration barriers for vacancy path 1 and 2 with defects.

Defect	Path 1	Path 2
Standard	0.111 eV	0.111 eV
$Al_{Li^{tet}}^{\bullet\bullet}$	0.174 eV	0.110 eV
$Nb_{Zr}^{\bullet}$	0.113 eV	0.132 eV
$V_{O}^{\bullet\bullet}$	0.146 eV	0.139 eV
Y_{La}^{x}	0.199 eV	0.171 eV
$Y_{Zr}^{'}$	0.110 eV	0.100 eV
$O_{i}^{''}$	-	0.135 eV

Table 5.5 shows the combined migration barriers for the different variations of the LLZO structure. These were produced by taking the harmonic average of the calculated migration barriers of the defects that can be found in the respective structures. The results show very similar migration barriers for both the undoped, Al-doped, Nb-doped and Y-doped structure.

Table 5.5: The harmonic average migration barriers for vacancy diffusion

Dopant	Harmonic average migration barrier [eV]
Undoped	0.126
Al-doped	0.129
Nb-doped	0.125
Y-doped	0.129

5.3 Localised Holes and Electrons

This section includes the results gathered from the calculations to test how the lowest energy vacancy paths are affected by the localisation of holes and electrons. Two different defects were tested. $Nb_{Zr}^{\bullet}$ was used to test the localisation of a charge compensating electron and Figure 5.16 shows the lowest energy paths for vacancy diffusion with a $Nb_{Zr}^{\bullet}$ defect. The lines marked as "Standard" is the calculated lowest energy paths without localisation of the electron. The other lines show the tests where the electron was localised on different ions. The different sites of electron localisation tested gives very similar results, which is also shown by the calculated migration barriers displayed in Table 5.6. The graphs with a localised electron show an increase in energy compared to the energy of the start structure. Especially the end of vacancy path 2 shows a large increase in energy. The migration barriers for path 1 all increase with the localisation of the electron and the opposite is true for vacancy path 2. This can be explained by the increase in energy of the end structures compared to the initial structures, resulting in a larger energy difference between start and end of path 1 and lower energy difference for path 2. Path 1 also shows some increase in path length, which may also lead to an increased migration barrier.

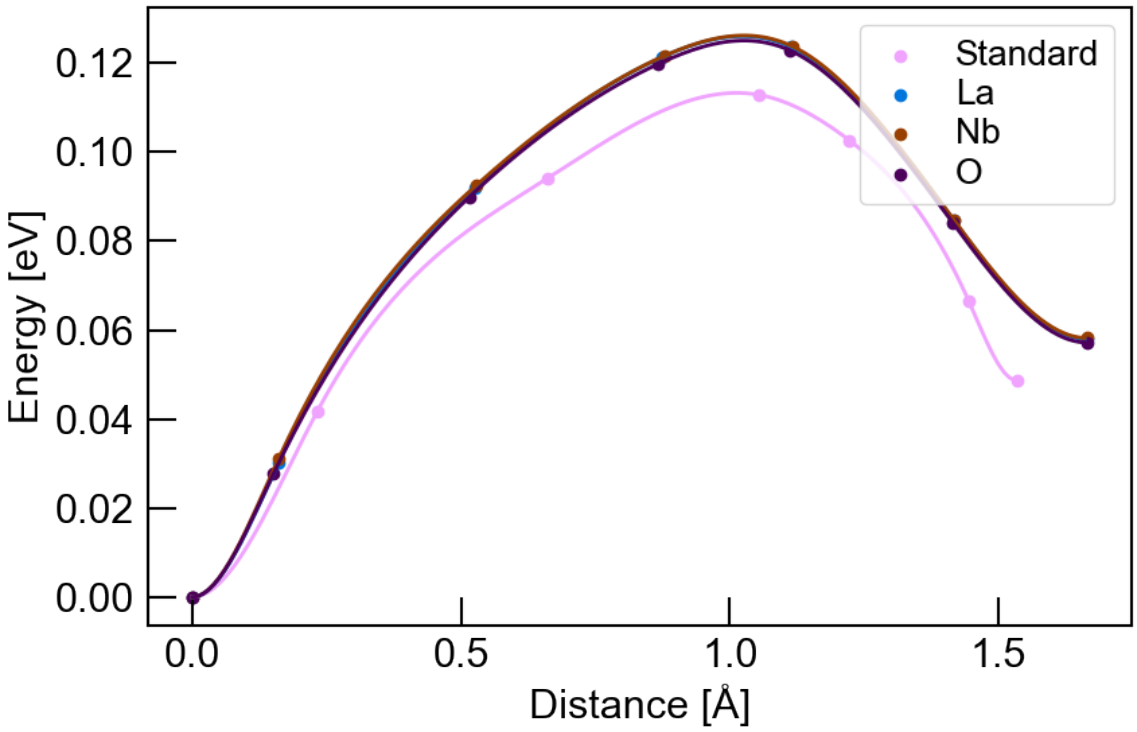

(a) Vacancy path 1

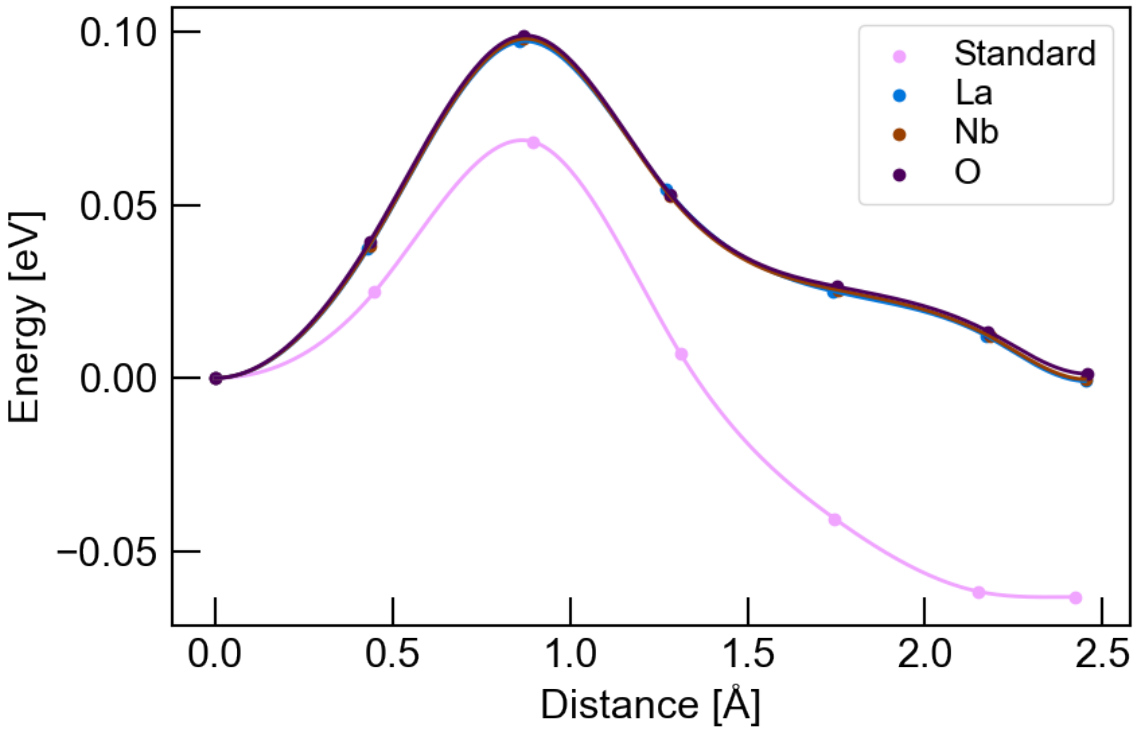

(b) Vacancy path 2

Figure 5.16: Vacancy path 1 (a) and 2 (b) with a $Nb^{\bullet}_{Zr}$ defect and the compensating electron on either an O, a La ion or the Nb ion. The line labeled "Standard" displays the lowest energy path without localisation of the electron.

Table 5.6: Migration barriers for vacancy diffusion with a $Nb^{\bullet}_{Zr}$ defect with localisation of the charge compensating electron. Standard displays the migration barrier without localisation of the electron, and La, Nb and O describes where the electron is localised.

Path	Standard	La	Nb	O
Path 1	0.113 eV	0.123 eV	0.126 eV	0.125 eV
Path 2	0.132 eV	0.098 eV	0.098 eV	0.099 eV

Figure 5.17 shows the result of NEB calculations for vacancy path 1 and 2 with a Y'_{Zr} defect close to the path. The charge compensation is here done by a localized hole on either an O ion close to the defect or the Y ion. The figure shows a decrease in the energy for the lowest energy paths for both path 1 and 2, compared to the initial structure. Similarly as for the $Nb^{\bullet}_{Zr}$, the largest observed difference in energy is found at the end of path 2. In addition, all the paths with localised holes show very similar results. The calculated migration barriers are shown in Table 5.7. Migration barriers for path 1 with a localised hole show a reduced energy barrier, but for path 2 all of them show an increased energy barrier. The change in migration barriers can again be explained by the change in the energy difference between the start and end structures. Path 1 now show a reduction in path length, which could contribute to decreasing the migration barrier.

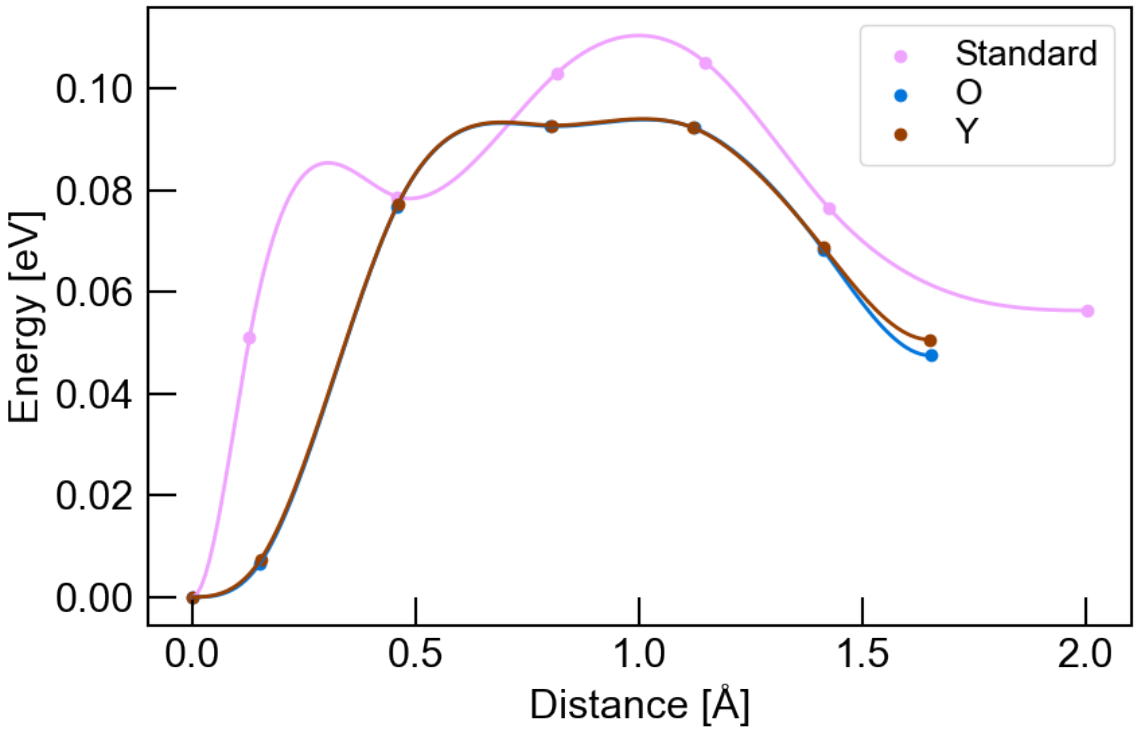

(a) Vacancy path 1

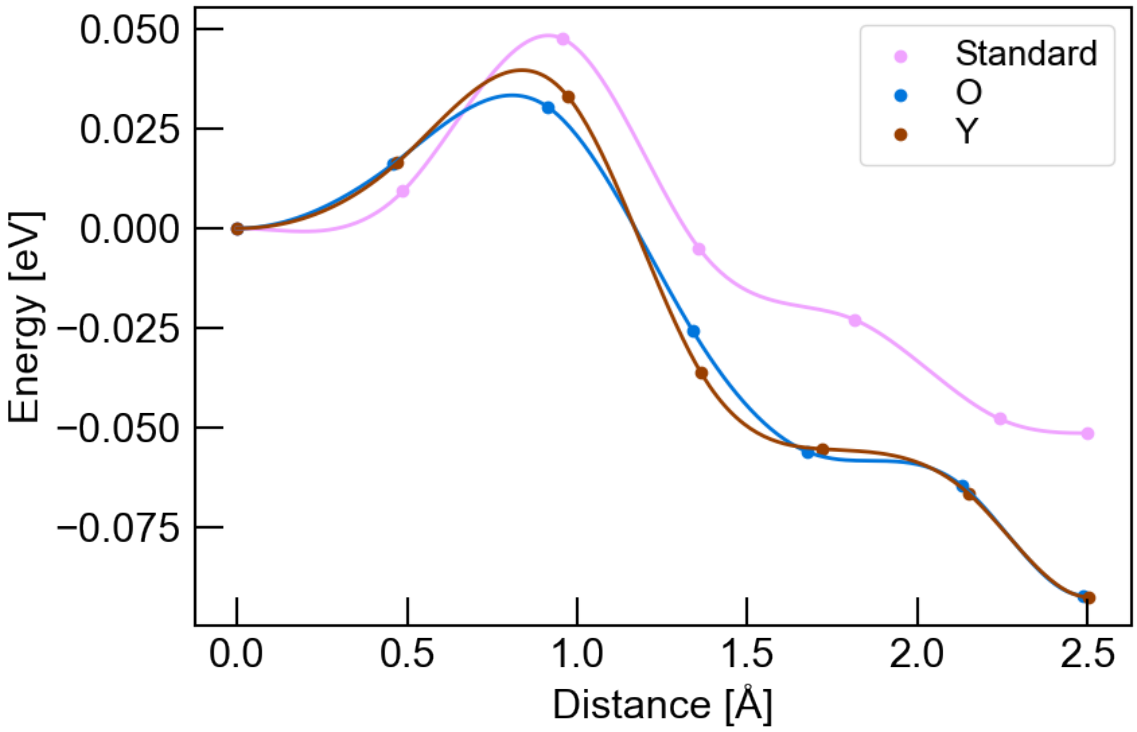

(b) Vacancy path 2

Figure 5.17: Vacancy path 1 (a) and 2 (b) with a Y'_{Zr} defect and the compensating hole on either an O or a Y ion

Table 5.7: Migration barriers for vacancy diffusion with a Y'_{Zr} defect with localisation of the charge compensating hole. Standard displays the migration barrier without localisation of the electron, and O and Y describes where the hole is localised

Path	Standard	O	Y
Path 1	0.110 eV	0.094 eV	0.094 eV
Path 2	0.100 eV	0.125 eV	0.132 eV

5.4 Li Ion Conductivity

5.4.1 Ionic Conductivity from Vacancy Diffusion

Figure 5.18 displays the calculated ionic conductivity from vacancy diffusion for undoped, Al-doped, Nb-doped and Y-doped tetragonal LLZO as a function of the charge carrier density and temperature. The curved lines show the ionic conductivities in $\frac{\mathrm{S}}{\mathrm{cm}}$. The dotted and dashed horizontal lines in the figure show the calculated charge carrier densities in oxygen rich/metal poor and oxygen poor/metal rich sintering environments, respectively. Table 5.8 shows the ionic conductivity at 298K and with the charge carriers densities calculated in a previous project [8]. The Nb-doped structure shows the highest calculated Li ion conductivity of $4.37 \cdot 10^{-4}$ $\frac{\mathrm{S}}{\mathrm{cm}}$ in ambient temperature for the structure sintered in O rich/metal poor environment.

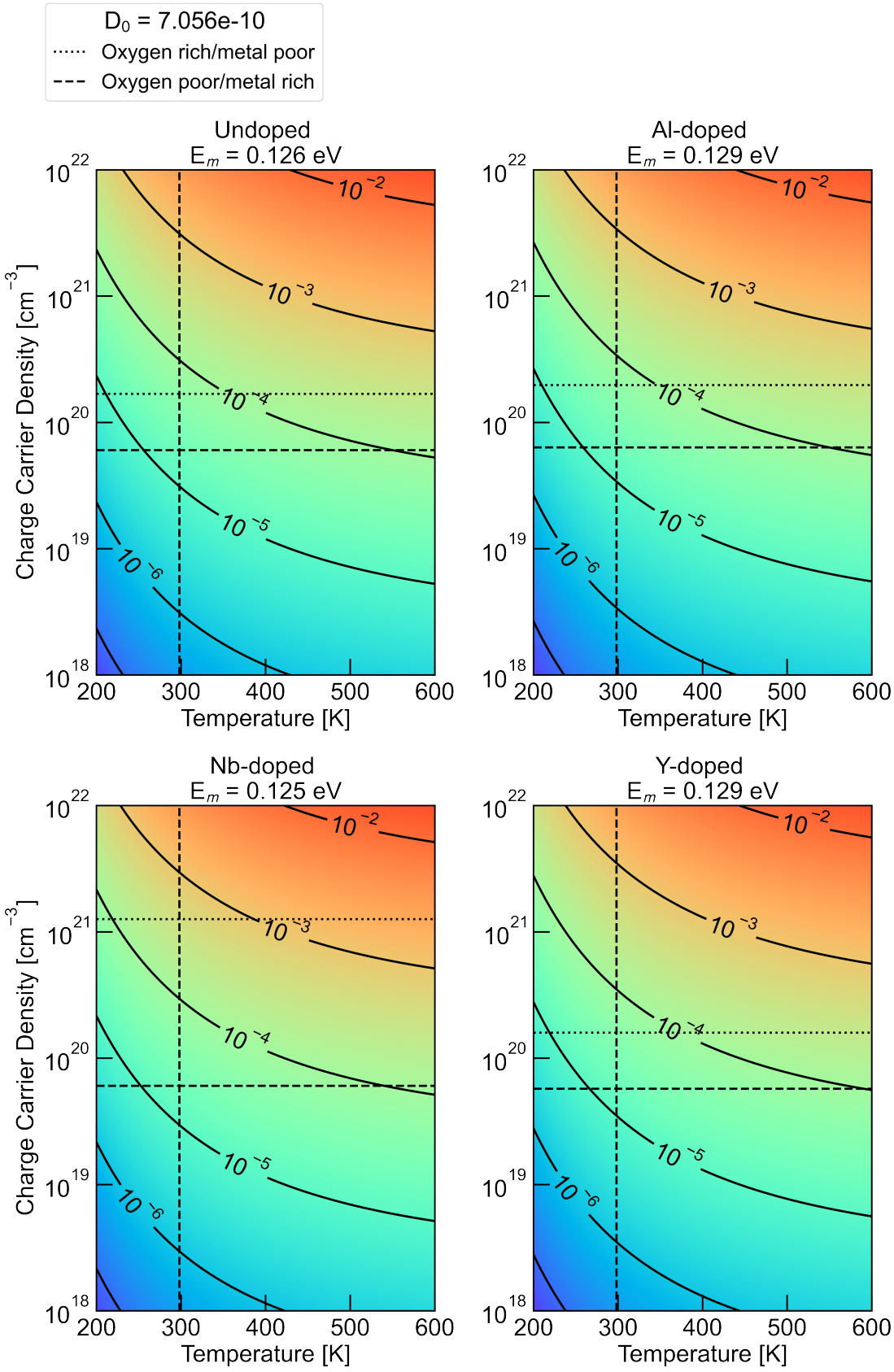

Figure 5.18: Predicted vacancy Li ion conductivity in undoped, Al-doped, Nb-doped and Y-doped LLZO structures. The vertical dotted line highlights room temperature and the horizontal lines describes the charge carrier density per cubic cm for O rich/metal poor and O poor/metal rich sintering environments. The curved lines show the ionic conductivity and is given in $\frac{\mathrm{S}}{\mathrm{cm}}$.

Table 5.8: Ionic conductivity as a result of vacancy diffusion in the undoped Al, Nb and Y doped LLZO structure. The conductivities are given in $\frac{S}{cm}$.

Dopant	Oxygen poor/metal rich	Oxygen rich/metal poor
Undoped	$1.99 \cdot 10^{-5}$	$5.53 \cdot 10^{-5}$
Al-doped	$2.22 \cdot 10^{-5}$	$5.53 \cdot 10^{-5}$
Nb-doped	$2.10 \cdot 10^{-5}$	$4.37 \cdot 10^{-4}$
Y-doped	$1.69 \cdot 10^{-5}$	$4.71 \cdot 10^{-5}$

5.4.2 Ionic Conductivity from Interstitialcy Diffusion

The predicted ionic conductivity contribution from interstitialcy diffusion is presented in Figure 5.19. The results show a conductivity in the order of 10^{-8} $\frac{S}{cm}$, which is very low compared to the contribution from the vacancy diffusion.

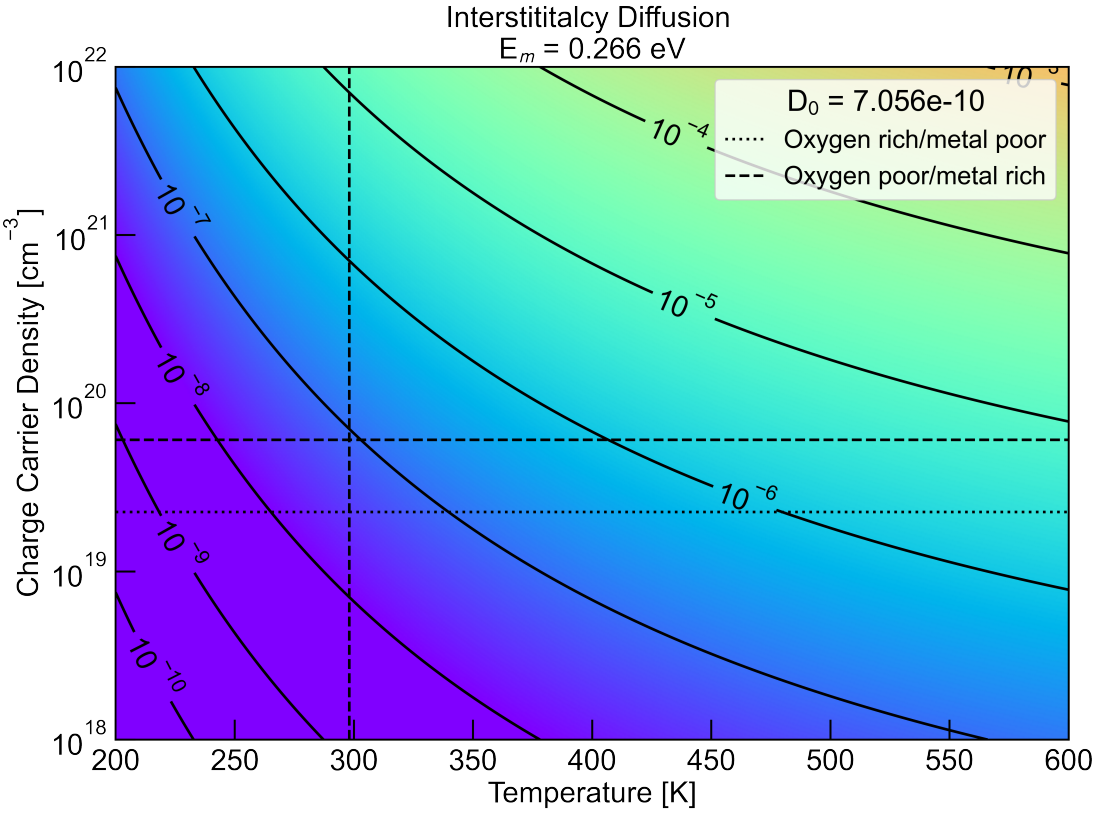

Figure 5.19: Predicted Li ion conductivity as a function of charge carrier density and temperature from interstitialcy movement

6 Discussion

6.1 Migration Barriers

6.1.1 Vacancy Diffusion

The migration barriers for path 1, 2 and 3, displayed in Section 5.1.1, show very low energy compared to the value of around 0.42 eV presented by Meier et al. [36]. In their calculations they investigated the the synchronous collective motion of Li ions and their NEB calculations included the movement of 6 different Li ions. Therefore, when compering the energy of a system where 6 Li ions are situated in their respective saddle point and a system where just 1 Li ion is in its saddle point, a difference in the systems energies are expected. However, a difference in migration energy of around 0.3 eV is still a significant difference. Another explanation could be their choice of functional for their DFT calculations. All of their calculations were conducted using the PBE functional and this functional is known to almost always overestimate the lattice constants of solids [60]. Furthermore, this can then lead longer paths than expected, thus higher migration barriers. The functional used in this project, PBEsol, is a version of PBE adapted for solids and does often show results in alignment with experimental lattice parameters and bond lengths.

Vacancy path 1 and 2 are the two paths received from `PYMATGEN` and are also the vacancy paths showing the lowest migration energies. The paths are shown in the Figure 5.1, 5.2 and 5.3, and path 1 is where the Li ion is moving from a Li^{tet} site to a distorted Li^{oct} site, path 2 is from an Li^{oct} site to a distorted Li^{oct} site and path 3 is between distorted Li^{oct} sites. The $V_{Li}^{'}$ will of course move the opposite direction. As described in the background section all the Li^{tet} sites and Li^{oct} sites are surrounded by distorted Li^{oct} sites. Therefore, Li ions needs to pass through distorted Li^{oct} sites to move around in the structure by vacancy diffusion. On the other hand, they do not necessarily need to pass through Li^{tet} or Li^{oct} sites. However, due to the migration barrier of path 3 being higher than path 1 and 2 it is preferable for the Li vacancies and ions to move such that every other site is a distorted Li^{oct} site. An example of such a path is shown below.

$$... \longleftrightarrow Li^{oct} \longleftrightarrow \text{Distorted } Li^{oct} \longleftrightarrow Li^{tet} \longleftrightarrow \text{Distorted } Li^{oct} \longleftrightarrow Li^{oct} \longleftrightarrow ... \quad (6.1.1)$$

Anything blocking or disrupting the optimal path will result in an increase in the migration barrier due to the Li ion needing to use path 3 as an alternative. This could for example be a result of dopants that prefer one special site over others. For instance Al ions that prefer Li^{tet} sites. However, many dopants are needed to block all the possible paths and the introduction of dopants like Al will therefore probably not have a large impact on the overall ionic conductivity. Electrostatic trapping can also disrupt the optimal path. A dopant's affinity of Li ions or $V_{Li}^{'}$ can result in trapping, thus reducing the mobility of the charge carrier. Table 6.1 displays binding energies, for a selection of low energy defects, from a previous project [8]. The binding energies are relatively small and indicates that these defects does not likely result in trapping of charge carriers in the LLZO structure.

Table 6.1: Binding energies for low energy defects and charge compensating Li defects [8].

Defects	Binding Energy [eV]
$Al^{\bullet}_{Li^{tet}} + 1\,V^{'}_{Li}$	-0.274
$Al^{\bullet\bullet}_{Li^{tet}} + 2\,V^{'}_{Li}$	-0.541
$Li^{\bullet}_{i} + 1\,V^{'}_{Li}$	-1.106
$Nb^{\bullet}_{Zr} + 1\,V^{'}_{Li}$	-0.120
$V^{\bullet}_{O} + 1\,V^{'}_{Li}$	-0.180
$V^{\bullet\bullet}_{O} + 2\,V^{'}_{Li}$	-1.252
$Y^{\bullet}_{Li^{oct}} + 1\,V^{'}_{Li}$	-0.480
$Y^{\bullet\bullet}_{Li^{oct}} + 2\,V^{'}_{Li}$	-0.811
$Y^{'}_{Zr} + 1\,Li^{\bullet}_{i}$	-0.108

Path 1 shows the largest energy difference between the initial and final structure. In this path, the Li ion is moving from a tetrahedral site to a distorted octahedral site. This means that the initial structure includes a distorted $V^{'}_{Li}{}^{oct}$ and that the final structure includes a $V^{'}_{Li}{}^{tet}$. The difference in energy agrees with results from a previous project showing that $V^{'}_{Li}{}^{oct}$ have lower formation energy than $V^{'}_{Li}{}^{tet}$. In addition, path 2 shows that the formation energies of distorted $V^{'}_{Li}{}^{oct}$ and $V^{'}_{Li}{}^{oct}$ are very similar.

The minimum energy path of vacancy path 3 is the only one of the vacancy paths that have two saddle points. After visually investigating the structures from the NEB calculation by the use of `VESTA`, it becomes clear what gives rise to the double peak. When the Li ion is in the middle of the path, see Figure 6.1, it is in a position where it is surrounded by 4 O ions which is creating an almost perfect Li^{tet} site. In previous work [8] 4 coordinated Li ions are found to be very stable in the tetragonal LLZO structure, thus creating a valley in the minimum energy path.

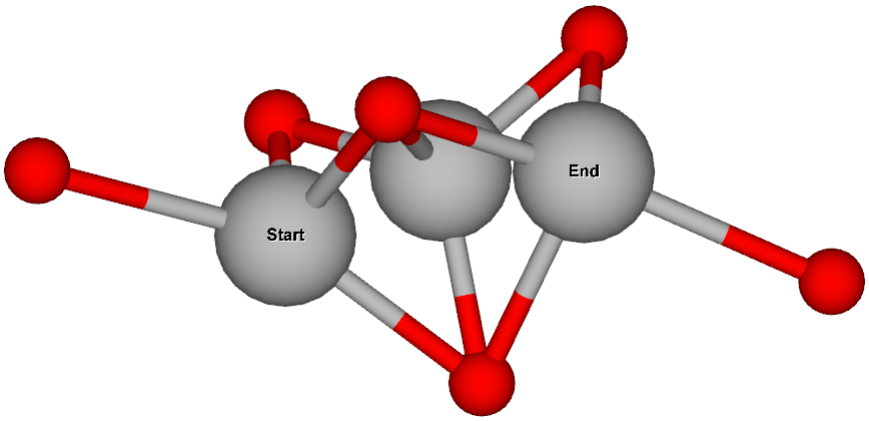

Figure 6.1: Vacancy path 3, with the start and end position in addition to the Li ion in the middle of the path.

To later calculate ionic conductivity only one migration barrier can be used. Therefore, the migration barriers are combined by the use of the harmonic average. Unfortunately, this may result in inaccurate migration barriers. For example, the harmonic average of the two migration barriers in the optimal path, described in equation 6.1.1, will be 0.110 eV,

but combining path 1 and 2 will result in an energy barrier of 0.174 eV. This is because vacancy path 1 ends with an energy of 0.064 eV compared to the start structure and if path 2 is added, the overall migration barrier will be 0.174 eV. When also considering the addition of defects, the migration barriers will possibly be even closer to experimental values of about 0.3-0.4 eV. In addition, the migration barrier of 0.174 eV is just 0.021 eV lower than the migration barrier of vacancy path 3. As a result, path 3 should also be considered a possible path for vacancy diffusion.

6.1.2 Interstitial Diffusion

Interstitial path 1 and 3 show very high migration barriers and indicates that the interstitial transport mechanism is not likely to contribute to the overall Li ion conductivity in tetragonal LLZO. The lowest energy path for path 2 is not displayed due to the generated initial and final structure relaxing to the exact same structures. This indicates that the script used to generate these paths is probably not perfect and could influence the result of the NEB calculations. However, the cubic phase is known to be stabilized by defects, so it is not unlikely to see some changes to the structure during relaxation of the LLZO structure with defects.

There are several reasons that can explain why the migration barriers of interstitial path 1 and 3 are so large. Firstly, a large increase in the path length is observed and a long path may lead to large migration barriers. The large increase in path length indicated that the interstitial sites move a lot during relaxation and this confirms that the python script does not find ideal interstitial positions. Secondly, the radius of the interstitial paths are to small. As described in the Computational Method section, the three interstitial paths with the most free space around the path were chosen for the calculations. Using linear interpolation from the start to the end structure to generate the path, the closest ions are about 1 Å away from the path before relaxation of the structures. These narrow paths are probably a large contributor to the high migration barriers received from the NEB calculations.

As described in the results section, the energy of the start and end structure for interstitial path 1 are very different, while the energy profile of path 3 is symmetrical. This result is most likely due to coordination of the Li ions in interstitial sites. Figure 5.5 (b) presents interstitial path 1 visualized by the use of `VESTA`, and it shows that the Li ion is moving from a site with coordination number of 5 to a site with coordination number of 4. The Li in lattice sites in the tetragonal LLZO structure have either a coordination number of 4 and 6 and as discussed earlier the Li sites with a coordination number of 4 is the most stable. The large difference in energy is therefore as expected. Figure 5.7 (b) shows that in path 3 the Li ion is moving from a site, with a coordination number of 5, to another site with a coordination number of 5. In addition the two sites looks almost identical and therefore about equal energies are expected. This type of reasoning can also be applied to explain why the start and end structure of path 2 relaxed to the same structure. As seen in Figure 5.6 (b), the Li ion moves from a tetrahedral site to a site with a coordination number of 5. Furthermore, this will probably result in a very large difference in energy between the start and end structure. In addition, the path length of 2.1 Å is very short, thus making it possible for the `VASP` relaxation to move one of the ions to the other interstitial site. As expected, when investigating the relaxed start and end structure, the $Li_i^{\bullet}$ are both found in the 4 coordinated stable tetrahedral start site.

6.1.3 Interstitialcy Diffusion

Interstitialcy path 1 and 3, displayed in Figure 5.12, show relatively low migration barriers, while path 2 shows a very large migration barrier. As seen in the figure, the length of path 2 is longer than the length of path 1 and 3 combined. Figure 5.9, 5.10 and 5.11 show the interstitialcy paths before relaxation and they show that only path 1 and 3 are symmetrical. In path 2 the lattice Li ion is moving from a tetragonal site to a 5 coordinated interstitial site. As discussed earlier, these 5 coordinated interstitial sites are not very stable and the result is that during relaxation, the Li ion in the 5 coordinated site moves to another position, further away, with lower energy. This explains the increased path length, which also partly can explain the large observed migration barrier. In addition, the $Li_i^{\bullet}$ on the other side of the Li lattice site, is situated very close to the lattice site, and is therefore also expected to move further away from the lattice site during relaxation. Visual investigations of the relaxed structures confirms that both the interstitial sites moved away from the lattice site during relaxation.

Figure 5.12 (b) shows the lowest energy path for just interstitialcy path 1 and 3, and as described in the results section the path lengths are similar, but the shape of the energy profiles are different. Path 1 shows a path with increasing energy from the start to the center of the path and then decreasing from the center to the end, while path 3 flattens at about 0.2 eV. The start and end structure for interstitialcy path 1 does not really change during relaxation. Figure 6.2 shows the two moving Li ions for path 1 from the structure in the saddle point. The ion to the left is moving from a tetrahedral interstitial site into a octahedral lattice site, while the other ion is moving from the octahedral lattice site into a tetrahedral interstitial site. Both the ions are at this moment situated in similar positions, and it looks reasonable that this is the saddle point, because they are not situated in the middle of 4 coordinated or 6 coordinated O polyhedra.

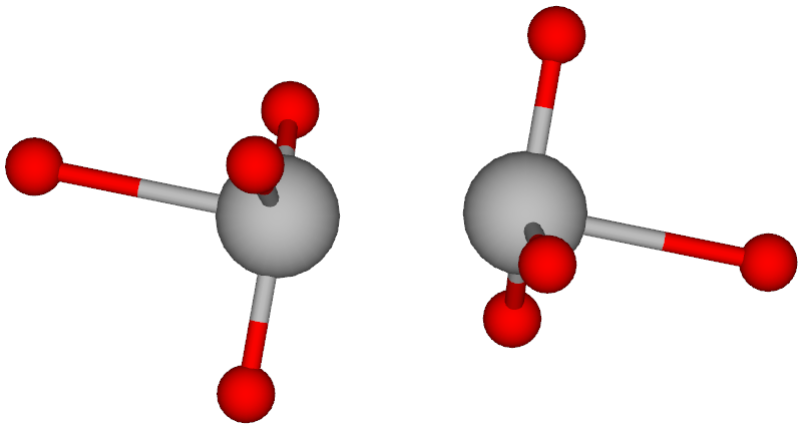

Figure 6.2: The two moving Li ions in the structure in the middle of interstitialcy path 1

Figure 6.3 (a) shows the relaxed interstitialcy path 3. Both the interstitial site in the start and end structure moved several angstrom during relaxation. Figure (b) displays the moving Li ions from the structure in the middle of the NEB calculation. The energy profile for this path is very flat after reaching 0.2 eV and can be explained by the two Li ions settling into 4 coordinated tetrahedra like sites, as seen in Figure 6.3 (b). The results again indicates that the 5 coordinated interstitial sites are not very stable. From the initial structure, energy is needed to push the Li ion away from the lattice site, but some energy is gained by removing the 5 coordinated site.

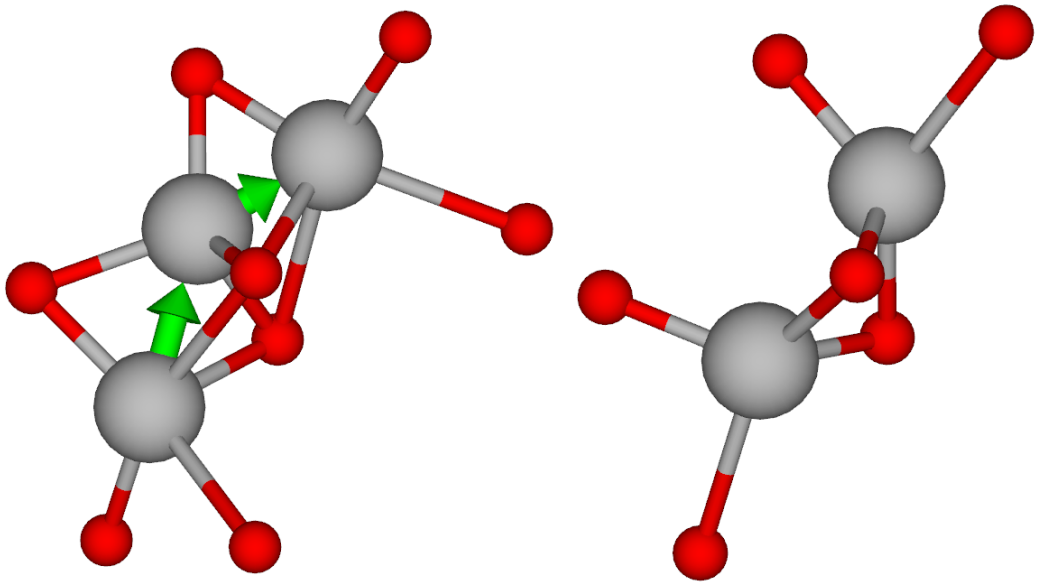

(a) (b)

Figure 6.3: (a) displays interstitialcy path 3 after relaxation. (b) shows the two moving Li ions in the structure in the middle of path.

The calculated migration barriers for path 1 and 3, displayed in Table 5.3, indicate that the interstitialcy transport mechanism may be a contributor to the Li ion transport in LLZO. The energy barrier of interstitialcy path 1 is twice as large as the barrier for path 3. When comparing the total energy of the initial structures, a difference of 0.015 eV is observed, with the initial structure of path 1 having the lowest energy. This energy difference is likely due to the 5 coordinated interstitial sites in path 3. The result is that the initial structure for path 3 is less likely to form. However, 0.015 eV is a very small energy difference.

6.1.4 Vacancy Diffusion with Additional Point Defects

The two lowest energy vacancy paths were investigated with a selection of additional point defects. These defects were chosen because of their low formation energy found in previous work [8]. The formation energies are displayed in Table 4.1 and the calculated lowest energy paths are presented in Figure 5.14 and 5.15. None of the defects results in a large increase in migration energy and the energies of the different paths are often very similar to the path without an extra defect. This is especially true for vacancy path 2.

For vacancy path 1, the path with an $Al^{\bullet\bullet}_{Li^{tet}}$ defect shows a very strange lowest energy path. From experience gathered during this project, defects in tetragonal LLZO have tendencies to induce changes in the structure. In addition, doping of tetragonal LLZO with Al is known as method for stabilizing the cubic phase. Therefore, it is reasonable to assume the introduction of an Al ion, might cause destabilization of some sites in addition to stabilizing new sites. As seen in the Figure 5.14, the Y^{x}_{La} defect causes the end structure to have lower energy than the start structure. This means that either the distorted octahedral site becomes more stable, the tetrahedra site becomes less stable or a mix of both. The Y ion is situated equally close to both the start and end site of the moving Li ion, and the distance between the different sites and the Y ion can therefore not be used to explain the results. The 8 coordinated Y ion has a radius of 1.019 Å, while the 8

coordinated La ion has a radius of 1.16 Å [63]. This difference in radius might be enough to give some extra space for the O ions, thus reducing the energy of the distorted octahedral site. The structures in the path with the Y'_{Zr} was also compared to the standard path by visual investigation, but no large differences were observed. A path with O''_i was also investigated, but the results from the NEB calculation were not plotted. This is because during the NEB relaxation the moving Li ion, in all the structures, relaxed towards either the start or the end structure, resulting in energies very close to either the start or the end of the path. Furthermore, other ions in the structure moved during the relaxation of the start and end structure and the result was large relative energies of up to 0.6 eV. This value cannot be trusted and should be disregarded. The NEB calculation was rerun with different optimizers, but every relaxation ended with the same structures, where the moving Li ion had moved to the initial or final site.

All the defects close to vacancy path 2 have the effect of increasing the difference in energy between the start and end structure. Most of the defects leads to the end structures having a lower energy. In other words, the defects leads to a stabilization of the distorted octahedral site or a destabilisation of the octahedral site. A reason for this difference could be where the defects are situated compared to the path. For instance, a $V^{\bullet\bullet}_O$ will probably prefer to be closer to the V'_{Li} side of the path. However, in this exact case the O ion chosen was situated equally close to both ends of the path. In addition, this is mostly true for the other defects as well and therefore, this explanation cannot be used. O''_i is the only defect that shows increasing energy for the final structure compared to the initial structure. The reason behind this effect could be that by introducing additional ions to the structure, the structure becomes more crowded. Visual investigations of the structure shows that the O''_i is located closer to end site of the moving Li ion and therefore, this increase in energy may be a result of an increase in crowdedness. The Al defect does also display strange results for vacancy path 2. The start and end structure does not seem to be fully relaxed, due to the second and sixth structures have a total energy lower than the initial and final structure, respectively. Al ions have proven to induce changes to the LLZO structure, in addition to making structures that are difficult to relax. Moreover, this could be because of the known effect of Al stabilizing the cubic structure.

All of the defects, except the $V^{\bullet\bullet}_O$ defect, added to vacancy path 1 results in a reduction in path length. This could be tributed to some of the defects showing some affinity for the V'_{Li} or the Li ion. Furthermore, if this is the case, similar reduction in path length should also be observed for vacancy path 2. However, this is not the case. Almost no reduction in path lengths are observed, except for the path with the Al defect. In general, path 2 is less affected by the introduction of defects and therefore, path 1 is possibly the vulnerable part of the Li transport system presented in Section 6.1.1. Furthermore, the reduction in path length between Li^{tet} and distorted Li^{oct} site could result in an increased distance between distorted Li^{oct} and Li^{oct} sites, thus also higher migration barriers for vacancy path 2.

Addition of a $Li^{\bullet}_i$ defect was also investigated, but during relaxation of both the initial and final structure, the $Li^{\bullet}_i$ just moved to the vacancy site. Several different algorithms for ionic relaxation were tested, but all of them ended with the same result. A solution to this problem could be to move the $Li^{\bullet}_i$ further away from the path, but this will reduce the observable effect on the calculated lowest energy paths.

In general, the introduction of defects in the LLZO structure does not lead to a large increase in migration barriers. The small changes in lowest energy paths are likely due to changes in the structure, not the affinity between the Li ion or the V'_{Li} and the defect. Therefore, doping can be used as method for increasing charge carrier density in the LLZO

structure. O interstitials are very important for inducing $V_{Li}^{'}$, thus also the charge carrier density. Moreover, from the results from the vacancy path 1 calculations, it is not clear how $O_i^{''}$ affects the lowest energy paths. However, the results from vacancy path 2 do not show any large difference between the structure with the $O_i^{''}$ compared to the other structures. Therefore, its is reasonable to believe that that $O_i^{''}$ will not have a large impact on the migration barriers and that the results from vacancy path 1 can be disregarded. Nonetheless, more calculations should be conducted in order to gain accurate information on the effects of the $O_i^{''}$ defect.

6.2 Localisation of Holes and Electrons

The band structure calculated for tetragonal LLZO, displayed in Figure D.1, shows a large band gap and flat valence and conduction bands. The large band gap together with flat bands and previous results showing that the Fermi level is pinned in between the valence and conduction band [8], suggest that the LLZO structure is a poor conductor of both electrons and holes. Therefore, the effect of localised holes and electrons on the lowest energy paths, were investigated and the results are shown in Section 5.3.

The lowest energy paths for vacancy path 1 and 2 with a $Nb_{Zr}^{\bullet}$ defect and a localised electron as charge compensation, are displayed in Figure 5.16 (a) and (b), respectively. The energy of the paths with a localised electron have changed compared to the standard path, but only by a small amount. The structures towards the end of the paths now have higher energy compared to the start structure, which means that having the moving Li ion in the distorted octahedral site has become less favourable compared to having it in the tetrahedral or octahedral site. The lowest energy paths with a localised electron are all almost identical, thus indicating that the observed effect arises only from having a localised electron, not where the electron is situated.

The energy of the vacancy paths with a $Y_{Zr}^{'}$ defect and a localised hole, are shown in Figure 5.17. Similarly as the results from the calculations with a localised electron, the results show that where the localised hole is situated does not affect the result. However, a small change in energy from the standard path to the paths with a localised hole is observed. A localised hole gives the opposite effect of a localised electron, and the distorted octahedral sites become more stable compared to the tetrahedral and octahedral sites.

Overall, the effect displayed by forced localisation of an electron or a hole does not heavily affect the calculated lowest energy vacancy paths. All the calculated migration barriers are in the range of ± 0.04 eV, compared to the path without either a localised hole or electron. A change of 0.04 eV is not a large change in energy, but it is large compared to the size of the calculated migration barriers and the localisation of holes and electrons should therefore not be disregarded as something that possibly can disrupt the mobility of the Li ions. Lastly, the method of forcing localisation with the use of magnetic moments can be questioned. Correct localisation of electrons and holes would be better served using DFT + U or hybrid functionals rather than assuming the positions ourselves and should be considered in future work.

Charge compensation by electrons and holes will compete with charge compensation by defects. As a result, the effects of aliovalent doping might be reduced and for example the charge compensation described in equation 4.1.1 and 4.1.2 can potentially lead to decreased formation of $V_{Li}^{'}$ and $Li_i^{\bullet}$, respectively. However, the two electrodes in contact with the electrolyte can act as reservoirs for electrons and holes, and in most cases electrons and

holes will find lower energy states in the electrodes. Consequently, the migration barriers in LLZO in a battery will in most cases not be affected by either localised holes or electrons.

6.3 Ionic Conductivity

The ionic conductivities calculated in this project are a result of charge carrier densities calculated in a previous project, as well as migration barriers calculated in this project. The ionic conductivities presented in Section 5.4 are predictions based on the Nernst-Einstein relation, equation 2.4.3.

6.3.1 Vacancy Conductivity

The calculated contribution to the ionic conductivity, as a result of vacancy diffusion, for the tetragonal LLZO structure is displayed in Figure 5.18. The figure includes a conductivity plot for the undoped, Al-doped, Nb-doped and Y-doped structure. The calculated migration barriers for the vacancy paths resulted in small variation in the migration barriers for the structures with the different dopants. The Al-doped and Y-doped structure shows the highest migration barrier of 0.129 eV, but they are all very similar. As a result, all the conductivity plots are very similar, and the only large difference is the charge carrier densities.

The calculated charge carrier densities are very similar in extreme O-poor/metal rich sintering environments. However, in extreme O-rich/metal-poor environments the variation in $V_{Li}^{'}$ concentrations are relatively large. The sintering environment can be tuned by changing the partial pressure of O, but the extremes shown in the plot are very difficult to achieve. Figure 2.6 shows the $V_{Li}^{'}$ concentration as a function of the chemical potential of O, which is representing the stability region. As a result, the charge carrier densities for O-poor/metal-rich environments will be larger than what is presented in Figure 5.18, but still very close to the dashed lines. Furthermore, the charge carrier densities from O-rich/metal-poor environments will be lower than the dotted lines in the figure. The Nb-doped structure show by far the largest charge carrier density in O-rich/metal-poor sintering environment and therefore also the largest Li ion conductivity of $4.37 \cdot 10^{-4}$ $\frac{\mathrm{S}}{\mathrm{cm}}$.

Regardless of the sintering environment, all the predicted ionic conductivities at ambient temperatures are larger than 10^{-5} $\frac{\mathrm{S}}{\mathrm{cm}}$. Reported ionic conductivities for the undoped tetragonal LLZO structure in room temperature are around 10^{-6} $\frac{\mathrm{S}}{\mathrm{cm}}$. Comparing these values, it is clear that all the predicted ionic conductivities in this figure are too high. To calculate the ionic conductivities there are three important inputs. The diffusion prefactor, the migration barriers and the charge carrier densities, and they can all be the source of the error.

The diffusion prefactor used in the calculations was calculated from estimations done by B. Andriyevsky et al. [62]. No additional sources describing the diffusion prefactor for tetragonal LLZO were found, and the calculated diffusion prefactor could therefore not be verified. As a result, great uncertainty is associated with the diffusion prefactor used in this project. The diffusion prefactor is proportional to the ionic conductivity and changing the prefactor will not change the difference in ionic conductivity between the different variations of the structure and between the different sintering environments.

As discussed in Section 6.1.1, the migration barriers calculated during this project are lower than other reported migration barriers for the tetragonal LLZO structure. In addition,

using the harmonic average to combine migration barriers may, as described, not result in accurate barriers. The ionic conductivity decreases exponentially with increasing migration barriers. Therefore, a small increase in the migration barrier will drastically decrease the ionic conductivity. In addition, the conductivity lines in the conductivity plot will become steeper at lower temperatures and result in the ionic conductivity being more temperature dependent around ambient temperature.

The charge carrier densities are taken from the results of a previous project [8]. Native defect concentrations have also been investigated by Squires et al. [43], and they report $V_{Li}^{'}$ concentrations of just above 10^{18} cm^{-3}. This is substantially lower concentrations than the concentrations used in this project. This difference is likely due to the functional used to calculate the defect formation energies. The defect concentrations used in this project were calculated using the PBEsol functional due to expense and time constrains, while Squires et al. used the HSE06 hybrid functional.

Using either a migration barrier of 0.3 eV or a charge carrier density of 10^{18} cm^{-3} will result in too low Li ion conductivities and this suggests that the migration barrier is in between what is found in this project and other reported values, that the charge carrier density is in between Squires et al. results and the densities presented in this report, that the diffusion prefactor is wrong or a mix of all of them. Even though the results does not display a good prediction of the ionic conductivity of tetragonal LLZO, it shows how dopants can change and improve the ionic condcutivity in solid state electrolytes.

6.3.2 Interstitialcy Conductivity

Figure 5.19 presents the ionic conductivity as a result of interstitialcy diffusion in the undoped tetragonal LLZO structure. The charge carriers for interstitialcy movement is $Li_i^{\bullet}$ and the dashed and dotted horizontal lines describes the the $Li_i^{\bullet}$ concentration for the different sintering environments. Similarly as for the $V_{Li}^{'}$ concentration, the lines show extreme environments which are not achievable. As seen in the figure, an O-poor/metal-rich environment is preferable for the formation of $Li_i^{\bullet}$, thus also interstitialcy diffusion. Unfortunately, this will result in a decrease in the $V_{Li}^{'}$ concentration, and consequently reducing the Li ion conductivity contribution from vacancy diffusion.

The predicted ionic conductivity from interstitialcy diffusion is in the order of 10^{-8} $\frac{S}{cm}$, which is very low and a 1000 times lower than the ionic conductivity from vacancy diffusion. In addition, it is likely that the ionic conductivity should be even lower. If the calculated ionic conductivities from vacancy diffusion are to high compared to experimental values, then the calculated ionic conductivities from interstitialcy diffusion should be expected to also give too large ionic conductivities. Consequently, the contribution from interstitialcy diffusion to the overall Li ion conductivity, at ambient temperatures, can be neglected.

6.4 Further Work

In this project, the migration barriers of vacancy, interstitial and interstitialcy paths have been investigated, but only two of the vacancy paths have been investigated with additional point defects. Therefore, the effects of additional defects on vacancy path 3 should be investigated. The interstitialcy paths investigated also displayed low energies and the effect of additional defects, close to these paths, should also be investigated. The concentration of $O_i^{''}$ defects is very large for structures sintered in an O-rich atmosphere and the results

from the calculations with this defect were not conclusive. Therefore, the effect of this point defect on the migration barriers should be properly investigated in the future. In addition, more interstitial paths should be investigated in order to completely rule out the interstitial mechanism as a possible Li ion transport mechanism in tetragonal LLZO.

As discussed in Section 6.3.1, the calculated ionic conductivities are very large compared to experimental values. Therefore, it could be necessary to recalculate some of the defect formation energies with a hybrid functional, in order to investigate if the defect concentrations calculated with the PBEsol functional are trustworthy.

An electrolyte for use in batteries needs to be compatible with the electrodes. Therefore, interactions between possible electrodes and the LLZO structure should be investigated. In addition, solid state electrolytes are known to show bad contact with the electrodes and methods for ensuring good contact needs to be developed.

Further work should also include investigation of other structures than LLZO. Aliovalent doping have proven to be a viable option for inducing desired defects in LLZO without increasing the migration barriers by a substantial amount. Therefore, this technique should also be investigated for other promising solid electrolytes to see if other structures show similar results. By investigating even more structures, even more can be learned about the effects of aliovalent doping.

All calculations carried out during this project are on the tetragonal LLZO structure. Further work may include conducting similar investigations on the more conductive cubic phase. However, the results from the calculations on tetragonal structure should give a good indication of what to expect from the cubic structure. Furthermore, the effect of the different defects and dopants on the stabilization of the cubic phase, should be investigated.

7 Conclusion

Investigations of the lowest energy paths for vacancy diffusion resulted in finding a critical path. The path where the moving V'_{Li} is alternating between a distorted octahedral site and an octahedral or tetrahedral site was found to be the lowest energy path. A migration barrier of 0.110 eV was found for this path by taking the harmonic average of the migration barriers of the two subpaths. This method of combining migration barriers av been discussed and criticized, due to the possibility of this method underestimating the migration barriers. The addition of defects to the optimal vacancy path have also been investigated and resulted in a subtle increase in the migration barriers of around 0.028 eV on average. Migration barriers for paths with different defects were combined to barriers representing doped structures. V'_{Li} densities calculated in the previous project were used, together with the calculated migration barriers, to predict ionic conductivity. For O-poor/metal rich sintering environments the ionic conductivity of the undoped, Al-doped, Nb-doped and Y-doped structures were all in the order of 10^{-5} $\frac{S}{cm}$. O-rich/metal poor environment resulted in a doubling of the ionic conductivities for all the structures except the Nb-doped structure. The Nb-doped structure showed an ionic conductivity of more than 20 times the conductivity of the structure from sintering in O-poor/metal rich environment. However, the calculated ionic conductivities are about 10 times larger than experimental values and can therefore not be trusted. In spite of this large difference in ionic conductivity, the results show that aliovalent doping can lead to a large increase in ionic conductivity in solids.

The migration barriers calculated for interstitial diffusion were very large. One of the three NEB calculations failed, but the others showed barriers of about 2 eV and 3 eV. These large energy barriers are likely a result of very narrow interstitial paths in the LLZO structure and indicate that interstitial diffusion will not contribute to the overall Li ion conductivity.

Two of the three interstitialcy paths investigated during this project, showed relatively low migration barriers. The third displayed a migration barrier of 2 eV, but this was due to a drastic increase in path length as a result of the relaxation of the start and end structures. The two lowest migration barriers were used, together with $Li_i^\bullet$ densities from the previous project, to calculate ionic conductivity from interstitialcy diffusion. The result was an ionic conductivity of about 10^{-8} $\frac{S}{cm}$, which is about 1000 times lower than the contribution from vacancy diffusion. As a result, the interstitialcy transport mechanism can be disregarded as an important mechanism for ionic conductivity in the tetragonal LLZO structure.

The localization of electrons and holes resulted in small changes in the lowest energy paths for vacancy diffusion and resulted in migration barriers of ± 0.04 eV compared to the structure without a localised hole or electron. Even though the energy difference is small, it is relatively large compared to the size of the migration barriers. Therefore, more test are needed in order to improve our understanding of the electrostatic effects of localisation of holes and electrons.

To summarize, the vacancy transport mechanism is the main contributor to ionic conductivity in the tetragonal LLZO structure. Aliovalent doping can induce desired defects without disrupting the mobility of the charge carriers. For other LLZO like structures, aliovalent doping might be a great tool for enhancing ionic conductivity, but more tests and investigations are needed.

References

[1] United Nations. Climate Change. URL https://www.un.org/en/global-issues/climate-change.

[2] V.J. Inglezakis. Chapter 7 - Extraterrestrial Environment. In Stavros G. Poulopoulos and Vassilis J. Inglezakis, editors, *Environment and Development*, pages 453 – 498. Elsevier, Amsterdam, 2016.

[3] World Ocean Review(WOR). WORLD OCEAN REVIEW 1, LIVING WITH THE OCEANS. – A REPORT ON THE STATE OF THE WORLD'S OCEANS. 2010.

[4] UNITED NATIONS. PARIS AGREEMENT. 2015. URL https://unfccc.int/sites/default/files/english_paris_agreement.pdf.

[5] V. Masson-Delmotte, P. Zhai, H. O. Pörtner, D. Roberts, J. Skea, P.R. Shukla, A. Pirani, W. Moufouma-Okia, C. Péan, R. Pidcock, S. Connors, J. B. R. Matthews, Y. Chen, X. Zhou, M. I. Gomis, E. Lonnoy, T. Maycock, M. Tignor, and T. Waterfield (eds.). Global Warming of 1.5°C. An IPCC Special Report on the impacts of global warming of 1.5°C above pre-industrial levels and related global greenhouse gas emission pathways, in the context of strengthening the global response to the threat of climate change, sustainable development, and efforts to eradicate poverty. *IPCC*, 2018.

[6] Xuebing Han, Languang Lu, Yuejiu Zheng, Xuning Feng, Zhe Li, Jianqiu Li, and Minggao Ouyang. A review on the key issues of the lithium ion battery degradation among the whole life cycle. *eTransportation*, 1:100005, 2019.

[7] Masaki Yoshio, Ralph J. Brodd, and Akiya Kozawa. *Lithium-Ion Batteries*. Springer, 2009. ISBN 978-0-387-34445-4. doi: https://doi.org/10.1007/978-0-387-34445-4.

[8] Kristoffer Eggestad. Computational Study of Point Defects in the Li Ion Solid State Electrolyte $Li_7La_2Zr_3O_{12}$. Department of Material Science and Engineering, Norwegian University of Technology and Science, 12 2020.

[9] Keith B. Oldham, Jan C. Myland, and Alan M. Bond. *Electrochemical Power*, chapter 5, pages 85–104. John Wiley & Sons, Ltd, 2011. ISBN 9781119965992. doi: https://doi.org/10.1002/9781119965992.ch5.

[10] Daniel Uxa, Bujar Jerliu, Erwin Hüger, Lars Dörrer, Michael Horisberger, Jochen Stahn, and Harald Schmidt. On the Lithiation Mechanism of Amorphous Silicon Electrodes in Li-Ion Batteries. *The Journal of Physical Chemistry C*, 123(36):22027–22039, 2019. doi: 10.1021/acs.jpcc.9b06011.

[11] Wu Xu, Jiulin Wang, Fei Ding, Xilin Chen, Eduard Nasybulin, Yaohui Zhang, and Ji-Guang Zhang. Lithium metal anodes for rechargeable batteries. *Energy Environ. Sci.*, 7:513–537, 2014. doi: 10.1039/C3EE40795K.

[12] Matthew Li and Jun Lu. Cobalt in lithium-ion batteries. *Science*, 367(6481):979–980, 2020. ISSN 0036-8075. doi: 10.1126/science.aba9168.

[13] Jeffrey W. Fergus. Recent developments in cathode materials for lithium ion batteries. *Journal of Power Sources*, 195(4):939–954, 2010. ISSN 0378-7753. doi: https://doi.org/10.1016/j.jpowsour.2009.08.089.

[14] Dmitry Belov and Mo-Hua Yang. Investigation of the kinetic mechanism in overcharge process for Li-ion battery. *Solid State Ionics*, 179(27):1816–1821, 2008. ISSN 0167-2738. doi: https://doi.org/10.1016/j.ssi.2008.04.031. Solid State Ionics 16: Proceedings of the 16th International Conference on Solid State Ionics (SSI-16), Part II.

[15] Chil-Hoon Doh, Dong-Hun Kim, Hyo-Suck Kim, Hye-Min Shin, Young-Dong Jeong, Seong-In Moon, Bong-Soo Jin, Seung Wook Eom, Hyun-Soo Kim, Ki-Won Kim, Dae-Hee Oh, and Angathevar Veluchamy. Thermal and electrochemical behaviour of C/Li_xCoO_2 cell during safety test. *Journal of Power Sources*, 175(2):881–885, 2008. ISSN 0378-7753. doi: https://doi.org/10.1016/j.jpowsour.2007.09.102.

[16] Boris Ravdel, K.M Abraham, Robert Gitzendanner, Joseph DiCarlo, Brett Lucht, and Chris Campion. Thermal stability of lithium-ion battery electrolytes. *Journal of Power Sources*, 119-121:805–810, 2003. ISSN 0378-7753. doi: https://doi.org/10.1016/S0378-7753(03)00257-X. Selected papers presented at the 11th International Meeting on Lithium Batteries.

[17] Yi Zhan, Wei Zhang, Bing Lei, Hongwei Liu, and Weihua Li. Recent Development of Mg Ion Solid Electrolyte. *Frontiers in Chemistry*, 8:125, 2020. ISSN 2296-2646. doi: 10.3389/fchem.2020.00125.

[18] Theodosios Famprikis, Pieremanuele Canepa, James Dawson, M. Saiful Islam, and Christian Masquelier. Fundamentals of inorganic solid-state electrolytes for batteries. *Nature Materials*, 18:1–14, 08 2019. doi: 10.1038/s41563-019-0431-3.

[19] Yonatan Horowitz, Christina Schmidt, Dong-hwan Yoon, Luise Mathilda Riegger, Leon Katzenmeier, Georg Maximillian Bosch, Malachi Noked, Yair Ein-Eli, Jürgen Janek, Wolfgang G. Zeier, Charles Eliezer Diesendruck, and Diana Golodnitsky. Between Liquid and All Solid: A Prospect on Electrolyte Future in Lithium-Ion Batteries for Electric Vehicles. *Energy Technology*, 8(11):2000580, 2020. doi: https://doi.org/10.1002/ente.202000580.

[20] Jürgen Janek and Wolfgang Zeier. A solid future for battery development. *Nature Energy*, 1:16141, 09 2016. doi: 10.1038/nenergy.2016.141.

[21] Mogalahalli V. Reddy, Christian M. Julien, Alain Mauger, and Karim Zaghib. Sulfide and oxide inorganic solid electrolytes for all-solid-state li batteries: A review. *Nanomaterials*, 10(8), 2020. ISSN 2079-4991. doi: 10.3390/nano10081606.

[22] Chih-Long Tsai, Qianli Ma, Christian Dellen, Sandra Lobe, Frank Vondahlen, Anna Windmüller, Daniel Grüner, Hao Zheng, Sven Uhlenbruck, Martin Finsterbusch, Frank Tietz, Dina Fattakhova-Rohlfing, Hans Peter Buchkremer, and Olivier Guillon. A garnet structure-based all-solid-state li battery without interface modification: resolving incompatibility issues on positive electrodes. *Sustainable Energy Fuels*, 3: 280–291, 2019. doi: 10.1039/C8SE00436F.

[23] David W. Richerson and William E. Lee. *Modern ceramic engineering: Properties, Processing, and Use in Design*, chapter 10, pages 320–321. CRC Press, 2018.

[24] Helmut Mehrer. *Diffusion in Solids: Fundamentals, Methods, Materials, Diffusion-Controlled Processes*. Springer series in solid-state sciences. Springer, Berlin, Heidelberg, 2007. doi: 10.1007/978-3-540-71488-0.

[25] Milton Ohring. Chapter 1 - A Review of Materials Science. In Milton Ohring, editor, *Materials Science of Thin Films*, pages 1–56. Academic Press, San Diego, second edition edition, 2002. ISBN 978-0-12-524975-1. doi: https://doi.org/10.1016/B978-012524975-1/50004-5.

[26] S. Matsumoto. Silicon: Diffusion. In K.H. Jürgen Buschow, Robert W. Cahn, Merton C. Flemings, Bernhard Ilschner, Edward J. Kramer, Subhash Mahajan, and Patrick Veyssière, editors, *Encyclopedia of Materials: Science and Technology*, pages 8543–8549. Elsevier, Oxford, 2001. ISBN 978-0-08-043152-9. doi: https://doi.org/10.1016/B0-08-043152-6/01524-2.

[27] Peter Atkins and Julio de Paula. *Atkins' Physical Chemestry*. Oxford, 2014.

[28] Paul Heitjans and Sylvio Indris. Diffusion and ionic conduction in nanocrystalline ceramics. *Journal of Physics: Condensed Matter*, 15(30):R1257–R1289, jul 2003. doi: 10.1088/0953-8984/15/30/202.

[29] Eongyu Yi, Hao Shen, Stephen Heywood, Judith Alvarado, Dilworth Y. Parkinson, Guoying Chen, Stephen W. Sofie, and Marca M. Doeff. All-Solid-State Batteries Using Rationally Designed Garnet Electrolyte Frameworks. *ACS Applied Energy Materials*, 3(1):170–175, 2020. doi: 10.1021/acsaem.9b02101.

[30] Reinhard Wagner, Günther J. Redhammer, Daniel Rettenwander, Anatoliy Senyshyn, Walter Schmidt, Martin Wilkening, and Georg Amthauer. Crystal Structure of Garnet-Related Li-Ion Conductor $Li_{7-3x}Ga_xLa_3Zr_2O_{12}$: Fast Li-Ion Conduction Caused by a Different Cubic Modification? *Chemistry of Materials*, 28(6):1861–1871, 2016. doi: 10.1021/acs.chemmater.6b00038. PMID: 27019548.

[31] Venkataraman Thangadurai, Sumaletha Narayanan, and Dana Pinzaru. Garnet-type solid-state fast Li ion conductors for Li batteries: critical review. *Chem. Soc. Rev.*, 43:4714–4727, 2014. doi: 10.1039/C4CS00020J.

[32] Abin Kim, Seungjun Woo, Minseok Kang, Heetaek Park, and Byoungwoo Kang. Research Progresses of Garnet-Type Solid Electrolytes for Developing All-Solid-State Li Batteries. *Frontiers in Chemistry*, 8:468, 2020. ISSN 2296-2646. doi: 10.3389/fchem.2020.00468.

[33] Junji Awaka, Norihito Kijima, Hiroshi Hayakawa, and Junji Akimoto. Synthesis and structure analysis of tetragonal $Li_7La_3Zr_2O_{12}$ with the garnet-related type structure. *Journal of Solid State Chemistry*, 182(8):2046 – 2052, 2009.

[34] Ramaswamy Murugan, Venkataraman Thangadurai, and Werner Weppner. Fast Lithium Ion Conduction in Garnet-Type $Li_7La_3Zr_2O_{12}$. *Angewandte Chemie International Edition*, 46(41):7778–7781, 2007.

[35] Randy Jalem, Yoshihiro Yamamoto, Hiromasa Shiiba, Masanobu Nakayama, Hirokazu Munakata, Toshihiro Kasuga, and Kiyoshi Kanamura. Concerted Migration Mechanism in the Li Ion Dynamics of Garnet-Type $Li_7La_3Zr_2O_{12}$. *Chemistry of Materials*, 25(3):425–430, 2013. doi: 10.1021/cm303542x.

[36] Katharina Meier, Teodoro Laino, and Alessandro Curioni. Solid-State Electrolytes: Revealing the Mechanisms of Li-Ion Conduction in Tetragonal and Cubic LLZO by First-Principles Calculations. *The Journal of Physical Chemistry C*, 118(13):6668–6679, 2014. doi: 10.1021/jp5002463.

[37] Ramaswamy Murugan, Venkataraman Thangadurai, and Werner Weppner. Fast Lithium Ion Conduction in Garnet-Type $Li_7La_3Zr_2O_{12}$. *Angewandte Chemie International Edition*, 46(41):7778–7781, 2007. doi: https://doi.org/10.1002/anie.200701144.

[38] Wenjuan Xue, Yaping Yang, Qiaoling Yang, Yuping Liu, Lian Wang, Changguo Chen, and Renju Cheng. The effect of sintering process on lithium ionic conductivity of $Li_{6.4}Al_{0.2}La_3Zr_2O_{12}$ garnet produced by solid-state synthesis. *RSC Adv.*, 8:13083–13088, 2018. doi: 10.1039/C8RA01329B.

[39] Guanghua Liu, Tianjun Li, Yan Xing, and Wei Pan. Synthesis of li7la3zr2o12 solid electrolyte by solid phase sintering method. *IOP Conference Series: Materials Science and Engineering*, 678:012150, nov 2019. doi: 10.1088/1757-899x/678/1/012150.

[40] Hany El-Shinawi, Gary W. Paterson, Donald A. MacLaren, Edmund J. Cussen, and Serena A. Corr. Low-temperature densification of Al-doped $Li_7La_3Zr_2O_{12}$: a reliable and controllable synthesis of fast-ion conducting garnets. *J. Mater. Chem. A*, 5:319–329, 2017. doi: 10.1039/C6TA06961D.

[41] Eric Jianfeng Cheng, Asma Sharafi, and Jeff Sakamoto. Intergranular Li metal propagation through polycrystalline $Li_{6.25}Al_{0.25}La_3Zr_2O_{12}$ ceramic electrolyte. *Electrochimica Acta*, 223:85–91, 2017. ISSN 0013-4686. doi: https://doi.org/10.1016/j.electacta.2016.12.018.

[42] Yaoyu Ren, Yang Shen, Yuanhua Lin, and Ce-Wen Nan. Direct observation of lithium dendrites inside garnet-type lithium-ion solid electrolyte. *Electrochemistry Communications*, 57:27–30, 2015. ISSN 1388-2481. doi: https://doi.org/10.1016/j.elecom.2015.05.001.

[43] Alexander Squires, David Scanlon, and Benjamin Morgan. Native Defects and Their Doping Response in the Lithium Solid Electrolyte $Li_7La_3Zr_2O_{12}$. *Chemistry of Materials*, 12 2019.

[44] Daniel Rettenwander, Peter Blaha, Robert Laskowski, Karlheinz Schwarz, Patrick Bottke, Martin Wilkening, Charles A. Geiger, and Georg Amthauer. DFT Study of the Role of Al^{3+} in the Fast Ion-Conductor $Li_{7-3x}Al^{3+}_xLa_3Zr_2O_{12}$ Garnet. *Chemistry of Materials*, 26(8):2617–2623, 2014. doi: 10.1021/cm5000999. PMID: 25673921.

[45] Shinya Nishino, Takeo Fujiwara, and Hisatsugu Yamasaki. Nanosecond quantum molecular dynamics simulations of the lithium superionic conductor $Li_{4-x}Ge_{1-x}P_xS_4$. *Phys. Rev. B*, 90:024303, Jul 2014. doi: 10.1103/PhysRevB.90.024303.

[46] Jian-Fang Wu, En-Yi Chen, Yao Yu, Lin Liu, Yue Wu, Wei Kong Pang, Vanessa K. Peterson, and Xin Guo. Gallium-Doped $Li_7La_3Zr_2O_{12}$ Garnet-Type Electrolytes with High Lithium-Ion Conductivity. *ACS Applied Materials & Interfaces*, 9(2):1542–1552, 2017. doi: 10.1021/acsami.6b13902. PMID: 28004907.

[47] Bingkai Zhang, Rui Tan, Luyi Yang, Jiaxin Zheng, Kecheng Zhang, Sijia Mo, Zhan Lin, and Feng Pan. Mechanisms and properties of ion-transport in inorganic solid electrolytes. *Energy Storage Materials*, 10:139–159, 2018. ISSN 2405-8297. doi: https://doi.org/10.1016/j.ensm.2017.08.015.

[48] Seungho Yu and Donald J. Siegel. Grain Boundary Contributions to Li-Ion Transport in the Solid Electrolyte $Li_7La_3Zr_2O_{12}$ (LLZO). *Chemistry of Materials*, 29(22):9639–9647, 2017. doi: 10.1021/acs.chemmater.7b02805.

[49] David S. Sholl and Janice A. Steckel. *Density Functional Theory: A Practical Introduction*, chapter 1-3, pages 1–81. John Wiley & Sons, Ltd, 2009. ISBN 9780470447710. doi: https://doi.org/10.1002/9780470447710.ch1.

[50] P. Hohenberg and W. Kohn. Inhomogeneous electron gas. *Phys. Rev.*, 136:B864–B871, Nov 1964. doi: 10.1103/PhysRev.136.B864.

[51] W. Kohn and L. J. Sham. Self-consistent equations including exchange and correlation effects. *Phys. Rev.*, 140:A1133–A1138, Nov 1965. doi: 10.1103/PhysRev.140.A1133.

[52] Greg Mills and Hannes Jónsson. Quantum and thermal effects in H_2 dissociative adsorption: Evaluation of free energy barriers in multidimensional quantum systems. *Phys. Rev. Lett.*, 72:1124–1127, Feb 1994. doi: 10.1103/PhysRevLett.72.1124.

[53] Ziqin Rong, Daniil Kitchaev, Pieremanuele Canepa, Wenxuan Huang, and Gerbrand Ceder. An efficient algorithm for finding the minimum energy path for cation migration in ionic materials. *The Journal of Chemical Physics*, 145(7):074112, 2016. doi: 10.1063/1.4960790.

[54] Graeme Henkelman, Blas P. Uberuaga, and Hannes Jónsson. A climbing image nudged elastic band method for finding saddle points and minimum energy paths. *The Journal of Chemical Physics*, 113(22):9901–9904, 2000. doi: 10.1063/1.1329672.

[55] Daniel Sheppard, Rye Terrell, and Graeme Henkelman. Optimization methods for finding minimum energy paths. *The Journal of Chemical Physics*, 128(13):134106, 2008. doi: 10.1063/1.2841941.

[56] G. Kresse and J. Hafner. Ab initio molecular dynamics for liquid metals. *Phys. Rev. B*, 47:558–561, Jan 1993. doi: 10.1103/PhysRevB.47.558.

[57] G. Kresse and J. Furthmüller. Efficiency of ab-initio total energy calculations for metals and semiconductors using a plane-wave basis set. *Comput. Mater. Sci.*, 6(1): 15 – 50, 1996. ISSN 0927-0256. doi: 10.1016/0927-0256(96)00008-0.

[58] G. Kresse and J. Furthmüller. Efficient iterative schemes for ab initio total-energy calculations using a plane-wave basis set. *Phys. Rev. B*, 54:11169–11186, Oct 1996. doi: 10.1103/PhysRevB.54.11169.

[59] G Kresse and J Hafner. Norm-conserving and ultrasoft pseudopotentials for first-row and transition elements. *Journal of Physics: Condensed Matter*, 6(40):8245–8257, oct 1994. doi: 10.1088/0953-8984/6/40/015.

[60] John P. Perdew, Adrienn Ruzsinszky, Gábor I. Csonka, Oleg A. Vydrov, Gustavo E. Scuseria, Lucian A. Constantin, Xiaolan Zhou, and Kieron Burke. Restoring the Density-Gradient Expansion for Exchange in Solids and Surfaces. *Phys. Rev. Lett.*, 100:136406, Apr 2008. doi: 10.1103/PhysRevLett.100.136406.

[61] Benjamin A. D. Williamson, Thomas J. Featherstone, Sanjayan S. Sathasivam, Jack E. N. Swallow, Huw Shiel, Leanne A. H. Jones, Matthew J. Smiles, Anna Regoutz, Tien-Lin Lee, Xueming Xia, Christopher Blackman, Pardeep K. Thakur, Claire J. Carmalt, Ivan P. Parkin, Tim D. Veal, and David O. Scanlon. Resonant ta doping for enhanced mobility in transparent conducting sno2. *Chemistry of Materials*, 32(5): 1964–1973, 2020. doi: 10.1021/acs.chemmater.9b04845.

[62] B. Andriyevsky, K. Doll, and T. Jacob. Ab initio molecular dynamics study of lithium diffusion in tetragonal $Li_7La_3Zr_2O_{12}$. *Materials Chemistry and Physics*, 185:210–217, 2017. ISSN 0254-0584. doi: https://doi.org/10.1016/j.matchemphys.2016.10.025.

[63] R. D. Shannon. Revised effective ionic radii and systematic studies of interatomic distances in halides and chalcogenides. *Acta Crystallographica Section A*, 32(5):751–767, Sep 1976. doi: 10.1107/S0567739476001551.

[64] G P Francis and M C Payne. Finite basis set corrections to total energy pseudopotential calculations. *Journal of Physics: Condensed Matter*, 2(19):4395–4404, may 1990. doi: 10.1088/0953-8984/2/19/007.

A NEB Optimizers

As mentioned in Section 3.3 there are several different optimizers available for NEB calculations. Visit NEB-optimizers for more information on these optimizers. During this project the default VASP optimizer was used for most calculations. However, the "Quick-Min" optimizer [55] was used for a couple of tricky calculations. Examples of INCAR files for both the default VASP optimizer and the Quick-Min optimizer are provided in Section G.1 Therefore, the accuracy of the Quick-Min optimizer were tested. Vacancy diffusion for both path 1 and 2 with a $Nb_{Zr}^{\bullet}$ defect were chosen and used as test systems. Figure A.1 shows the migration barriers for vacancy path 1 and 2 with a Nb at a Zr site close to the path. The energy barriers are calculated using both the default VASP optimizer and the Quick-Min optimizer. From the figure it is clear that the two optimizers give very similar results. This indicates that the results from Quick-Min can be trusted for NEB calculations on the LLZO structure, but further testing is needed for a final verdict regarding the overall accuracy of the Quick-Min optimizer. However, from acquired experience during this project, the Quick-Min optimizer are able to calculate energy barriers for very strange and difficult paths. On the other hand this may lead to not finding errors in the relaxation of the start and end structures.

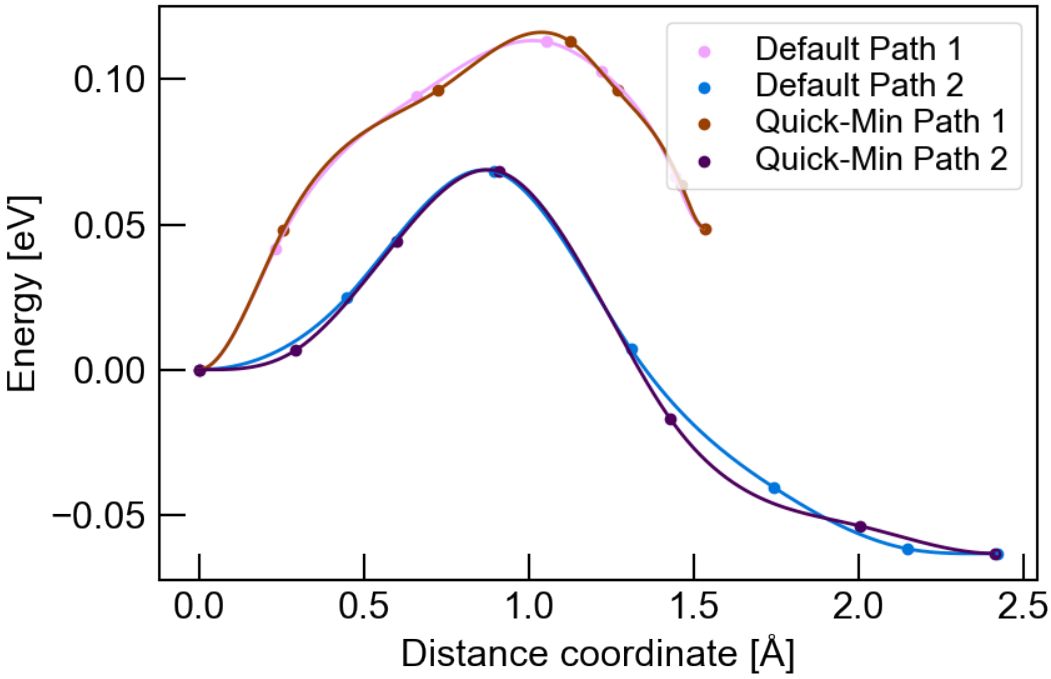

Figure A.1: Migration barriers for vacancy diffusion, for path 1 and 2, with a $Nb_{Zr}^{\bullet}$ defect, calculated using the default VASP optimizer as well as the Quick-Min optimizer.

The relaxation time of the NEB calculations were also investigated, and Table A.1 shows no clear results regarding which optimizer is the fastest.

Table A.1: NEB calculation relaxation time for vacancy path 1 and 2 with $Nb_{Zr}^{\bullet}$ using the default VASP optimizer and the Quick-Min optimizer. Gamma point relaxation and 5 nodes were used for all calculations and NSW is the maximum number of ionic steps.

NSW	Default Path 1	Quick-Min Path 1	Default Path 2	Quick-Min Path 2
10	00:47:58	01:03:07	01:05:34	00:59:07
20	01:02:15	01:21:30	00:59:07	01:03:04
30	00:57:40	01:05:19	01:05:13	01:16:15
40	01:32:36	01:11:31	01:24:34	01:05:09
50	01:11:32	01:02:50	01:45:28	00:43:29
60	00:39:22	01:26:53	01:47:56	01:05:29
70	–:–:–	01:15:34	01:08:48	00:31:12
80	–:–:–	02:02:07	00:29:18	–:–:–
90	–:–:–	01:28:41	–:–:–	–:–:–
Total	06:08:23	11:57:32	9:45:58	6:43:45

B Generating Structures for NEB Calculations

To be able to run NEB calculations, structures in between the start and end structure are needed. In the early parts of the project these structures were found by interpolation between the initial and final structure. Later in the project `pymatgen_diffusion.neb.pathfinder`'s `IDPPSolver` [53] was tested as an alternative. Vacancy path 2 with $O_i^{''}$ defect was selected as a test system. Both the speed and the results of the NEB calculations were investigated and compared. Table B.1 shows the maximum number of ionic steps, NSW, and time needed to relax NEB calculations when the structures were constructed with regular interpolation or the `IDPPSolver`.

Table B.1: NEB calculation relaxation time for vacancy path 2 with $O_i^{''}$ using regular interpolation or the `IDPPSolver`. Gamma point relaxation and 5 nodes were used for all calculations and NSW is the maximum number of ionic steps.

NSW	Regular Interpolation	`IDPPSolver`
10	00:54:12	01:12:14
20	00:25:27	00:12:14
30	00:34:50	00:12:14
40	01:14:09	01:12:14
50	00:40:57	–:–:–
60	00:44:08	–:–:–
70	00:16:54	–:–:–
Total	04:50:37	03:57:05

Figure B.1 shows the migration barriers found by the NEB calculations. The results are very similar and therefore, due to the reduction in relaxation time, the `IDPPSolver` was used for the remaining NEB calculations performed in this project. However, more test needs be conducted before the `IDPPSolver` can be called a superior method for generating NEB structures.

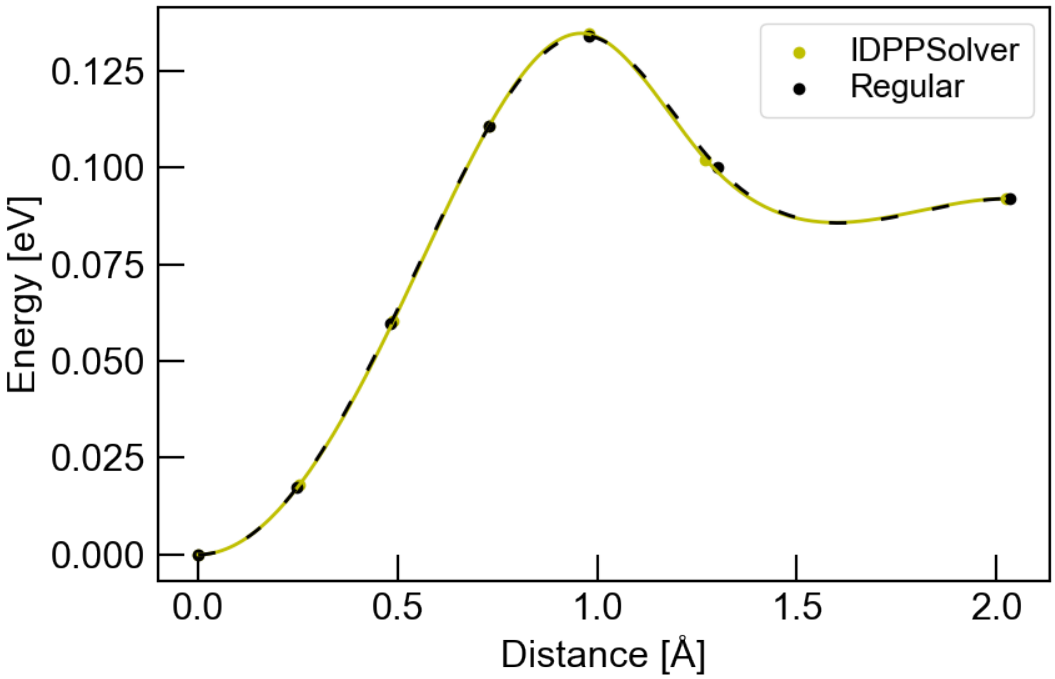

Figure B.1: Migration barriers calculated for vacancy path 2 with O_i'' using regular interpolation and `IDPPSolver` to generate structures in between the start and end structure. The energy barriers were calculated to be 0.134 and 0.135 eV respectively.

Listing B.1 displays the script used to generated the structures in between with the `IDPPSolver` and listing B.2 shows the script used to generate the structures by regular interpolation.

```
from pymatgen_diffusion.neb.pathfinder import IDPPSolver
from pymatgen import Structure
import os

init = Structure.from_file('CONTCAR_init')
final = Structure.from_file('CONTCAR_final')

idpp_solved_from_endpoints = IDPPSolver.from_endpoints(endpoints=[init,
    final], nimages=5,sort_tol=0.0).run()

for i,file in enumerate(idpp_solved_from_endpoints):
        try:
                os.mkdir('./'+"{:02d}".format(i))
        except:
                pass
        file.to(filename='./'+"{:02d}".format(i)+'/POSCAR',fmt='poscar')
```

Listing B.1: Python script for generating structures for NEB calculations by the use of `IDPPSolver`

```python
from pymatgen import Structure

initfile = Structure.from_file('POSCAR_init')
finalfile = Structure.from_file('POSCAR_final')

neb = initfile.interpolate(finalfile,nimages=6,pbc=True)

for index,structure in enumerate(neb):
    structure.to(filename='POSCAR-{}.vasp'.format(i+1,fmt='poscar')

initfile.to(filename='POSCAR-0.vasp', fmt='poscar')
finalfile.to(filename='POSCAR-{}.vasp'.format(len(neb)+1),fmt='poscar')
```

Listing B.2: Python script for generating structures for NEB calculations by the use of regular interpolation

C Convergence testing

C.1 Cutoff Energy

Figure C.1 shows the results of the convergence testing with respect to the cutoff energy for the tetragonal LLZO structure. From the figure it is clear the the energy converges around 500 eV. An energy cutoff of 600 eV were chosen for all calculations containing the LLZO structure due to possible Pulay stress [64].

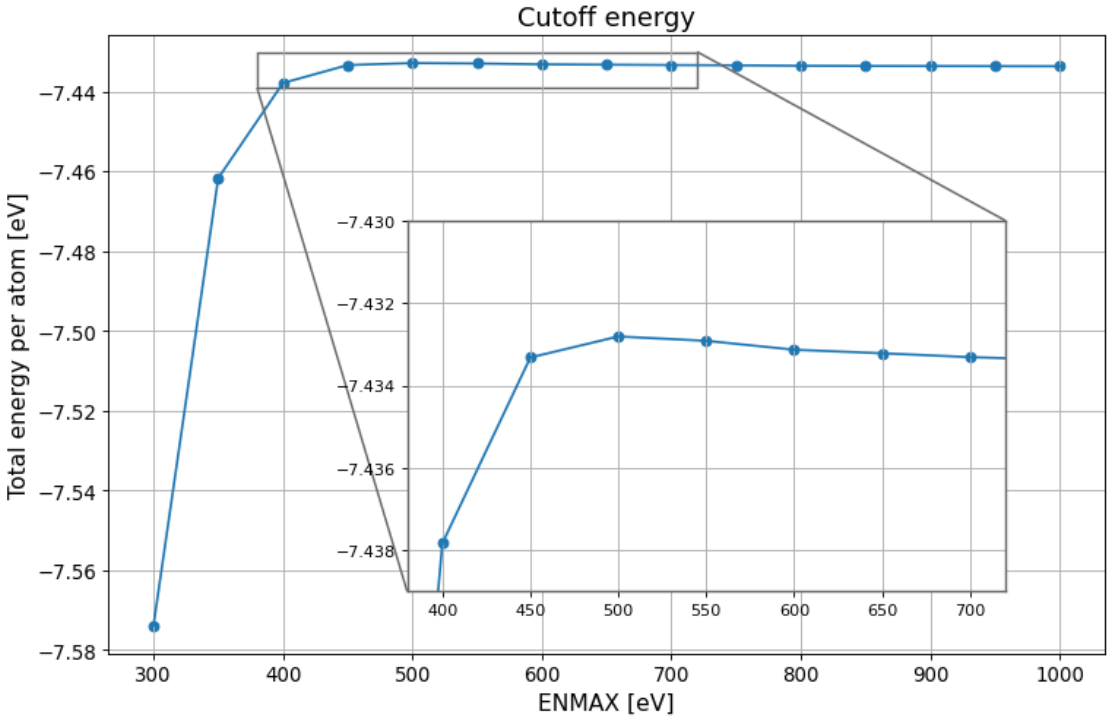

Figure C.1: Cutoff energy convergence testing for LLZO

C.2 *k*-points

Figure C.2 shows the convergence testing for k-points. `3x3x3` were chosen as k-points and used for all calculations concerning defect formation energies in previous work [8]. For all calculations in this project, gamma-point relaxation, with kpoints `1x1x1`, was used. k-point grids used in the convergence test were generated using `kgrid` (https://github.com/WMD-group/kgrid.git).

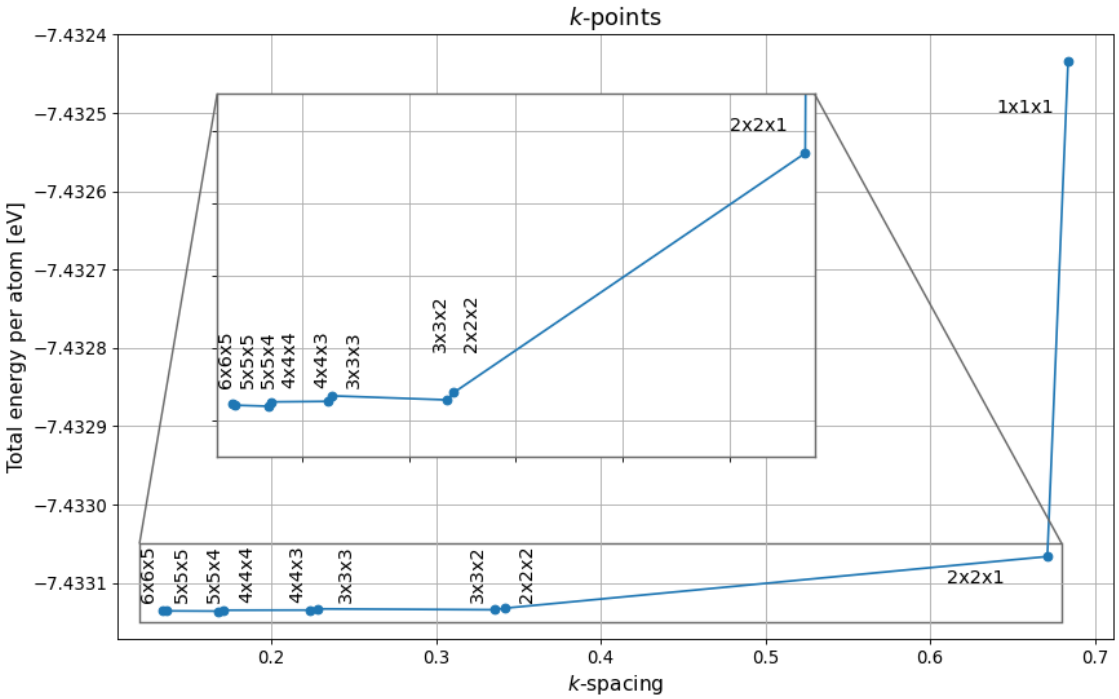

Figure C.2: k-points convergence testing for LLZO

D Electronic Structure

Figure D.1 shows the band structure of tetragonal LLZO calculated in a previous [8]. It was calculated using VASP with an energy cutoff of 600 eV, 3x3x3 as k-points grid and the PBEsol functional. The results from the same calculations were also used to produce the dos plot, which is displayed in Figure D.2. Both plots show an energy gap of just above 4 eV.

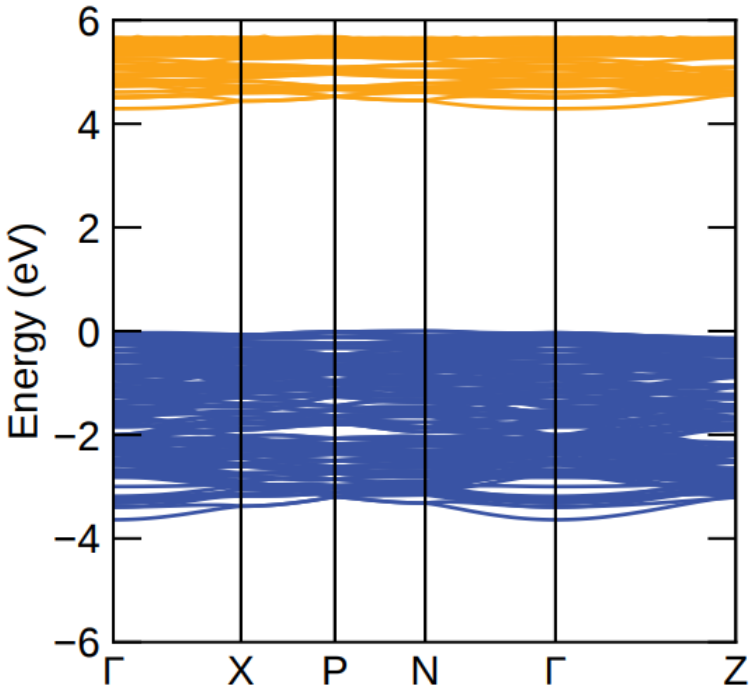

Figure D.1: Band structure for LLZO [8]

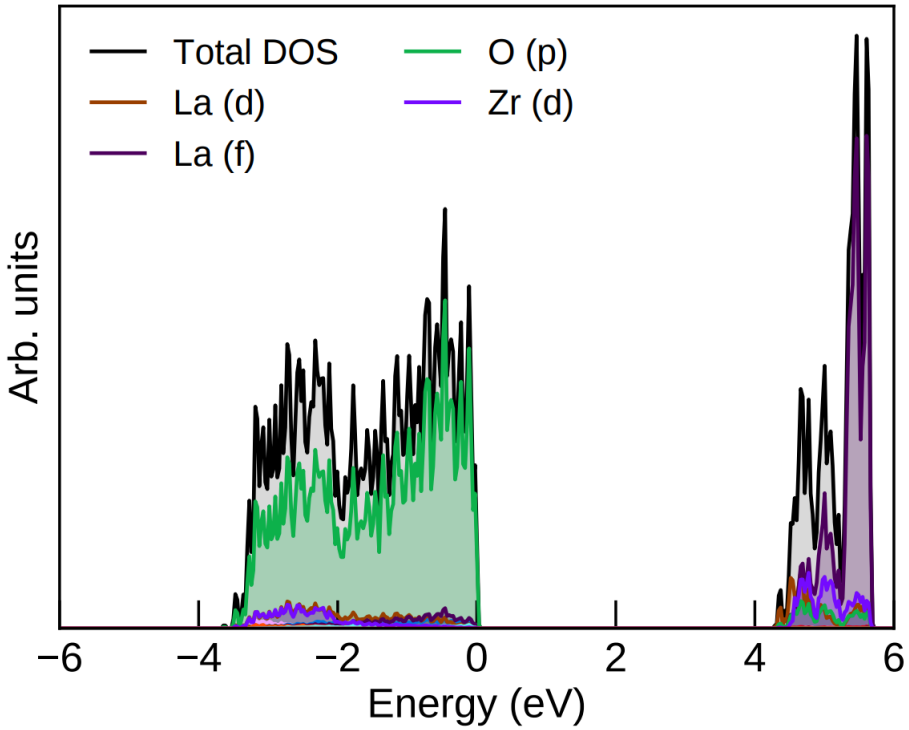

Figure D.2: Density of states for LLZO [8]

E Transition Level Diagram for Undoped LLZO

Figure E.1 displays the transition level diagrams for undoped tetragonal LLZO calculated during previous work [8]. (a) is calculated from metal rich/O-poor sintering environment, while (b) is calculated from metal poor/O-rich environment.

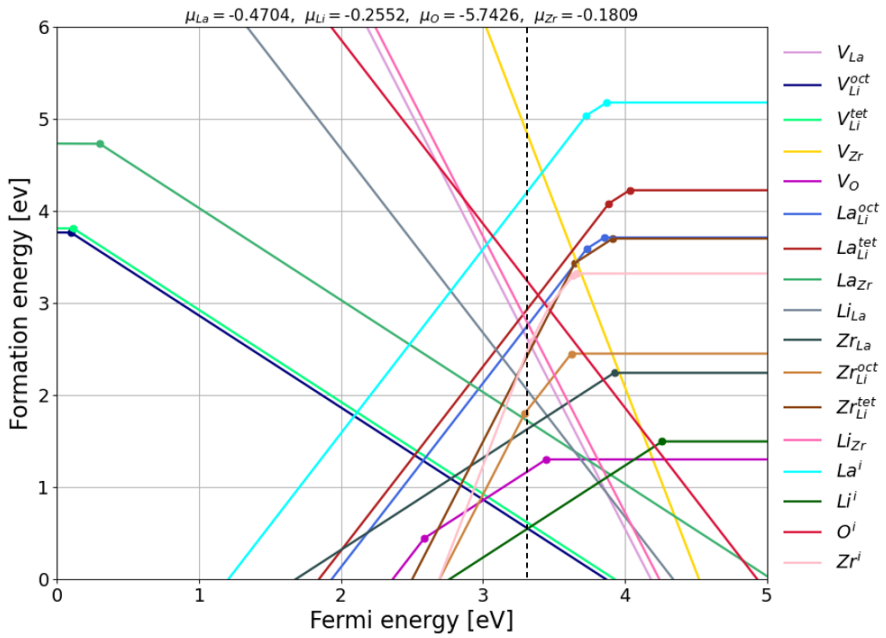

(a) Metal rich/oxygen poor

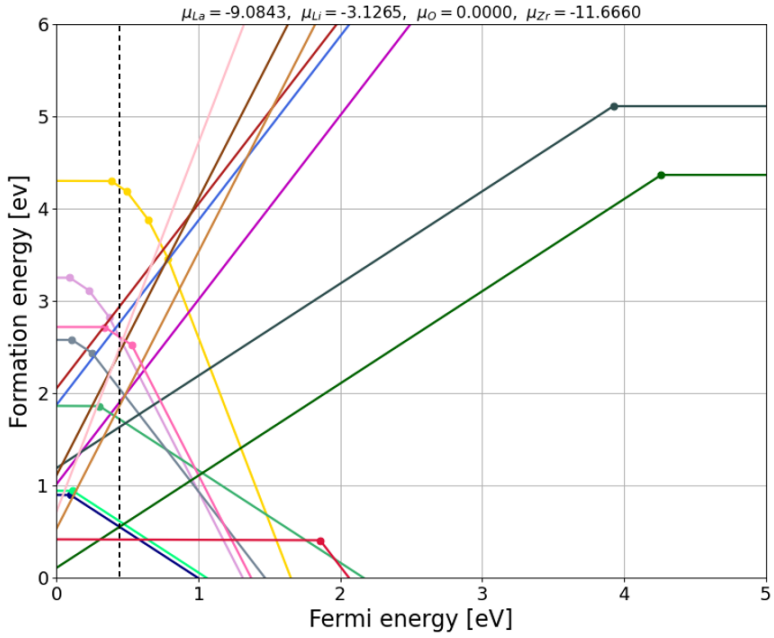

(b) Metal poor/oxygen rich

Figure E.1: Transition level diagram for undoped LLZO from different sintering environments. The black dashed line displays the pinning of the Fermi level.

F Scripts

F.1 Vacancy Path Finder

In this project, `pymatgen.analysis.path_finder`'s `DistinctPathFinder` [53] was used to find distinct vacancy paths as well as interstitial paths. The script determines and returns symmetrically distinct paths between atoms. The migrating species as well as the structure are given as input to the script. The script loops through all the equivalent sites and investigates their neighbors in order to construct paths between them.

F.2 VoronoiInterstitialGenerator

The `VoronoiInterstitialGenerator` is a class taken from `pymatgen.analysis.defects.generators` and are made to generate interstitial sites based on simple Voroni analysis. The script locates many interstitial sites, but only returns unique interstitial sites. To be able to generate interstitial and interstitialcy paths, all possible interstitial sites were needed. Therefore, the script was modified to return all interstitial sites found. The modified `VoronoiInterstitialGenerator` can be found in Jupyter file published on github.

F.3 ChargeDensityAnalyzer

The ChargeDensityAnalyzer class is taken from `pymatgen.analysis.defects.utils module` and is an analyzer made to find interstitial sites from the total charge density. A `CHGCAR` file is needed as an input and interstitials are found from minimums in the charge density.

F.4 Interstitial and Interstitialcy Path Finder

The script used to find interstitial and interstitialcy paths can be found at github. The script uses either the charge density or the structure to generate interstitial sites and then interstitial and interstitialcy paths. Using a POSCAR works great for small symmetrical structures while a CHGCAR file is recommended for larger structues. The script consists of six classes, `VoronoiInterstitialGenerator`, `AllInterstitials`, `InterstititalPath`, `InterstitialPaths`, `InterstitialcyPath`, `InterstitialcyPaths` and `chgcarInterstitials`. The `VoronoiInterstitialGenerator` is a version of `pymatgen.analysis-.defects.generators`'s `VoronoiInterstitialGenerator` modified to return all possible interstitial sites, not only the distinct sites. `AllInterstitials` is an object containing a structure with all interstitial sites of one type of atom. `InterstititalPath` and `InterstititalcyPath` paths are used to describe a path. An interstitial path needs a structure, an initial site, an end site and a migration specie. Similarly, an interstitialcy paths needs a structure, migrating specie, initial site and end site, but also a lattice site. These to objects includes methods for comparing paths and creating start and end structures. `InterstitialPaths` and `InterstitialcyPaths` are used to find and save information about all the possible paths. Lastly, `chgcarInterstitials` are used to generate interstitial sites

from the charge density by the use of a CHGCAR file. Minimums in the charge density are recognised as possible sites.

F.5 Interstitial sites

The following two figures, F.1 and F.2, display the interstitial sites found using two different methods. The first figure shows the interstitial sites generated using the POSCAR file, describing the LLZO structure. The second method instead utilizes the charge density of the structure. This charge density used in this project was received form the CHGCAR file after relaxation of the LLZO structure. Figure F.1 clearly shows more interstitial sites than Figure F.2. However, many of these are situated very close to each other and are in reality the same interstitial sites.

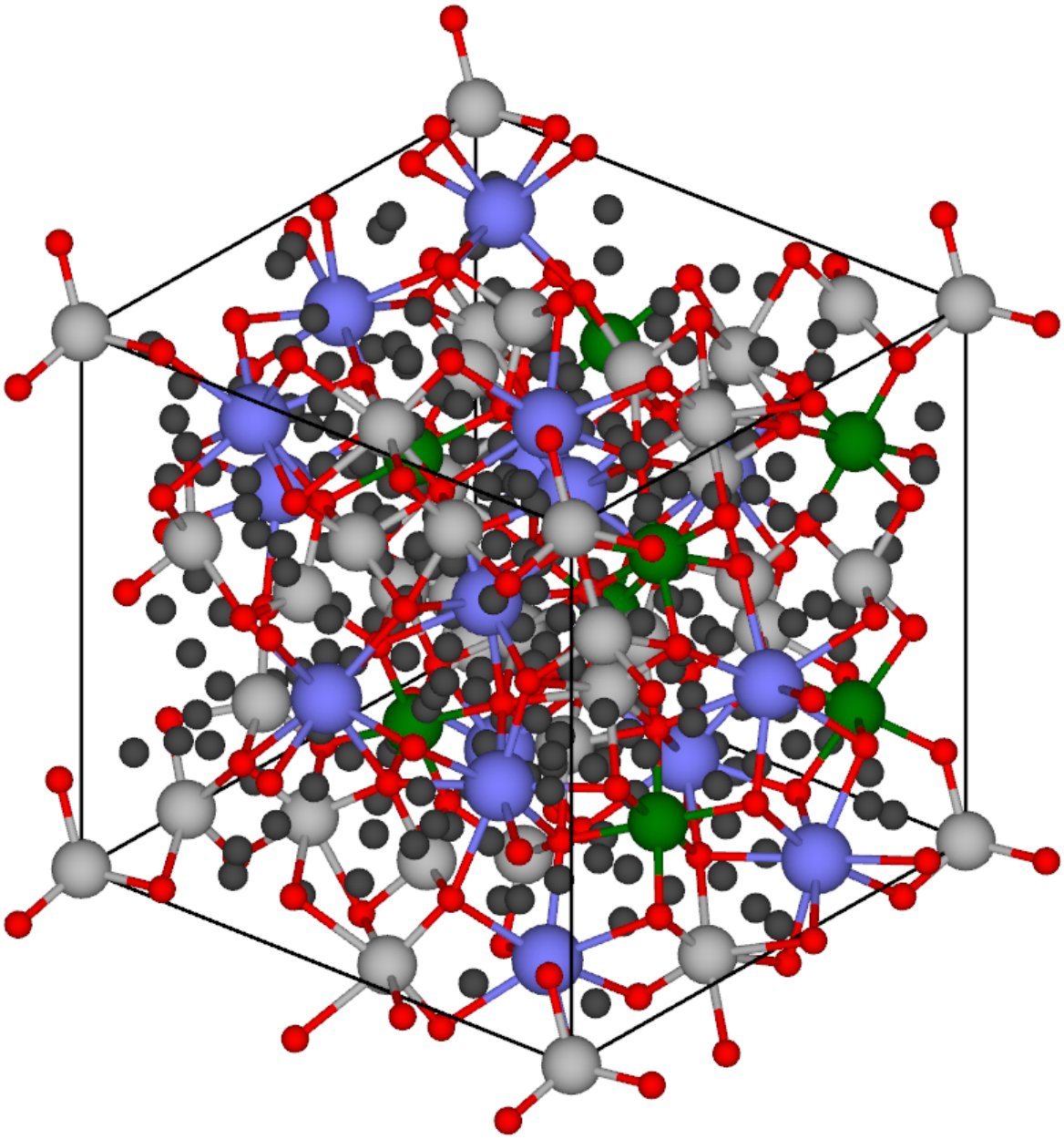

Figure F.1: The LLZO structure with all the possible interstitial sites received from `VoronoiInterstitialGenerator` marked in black

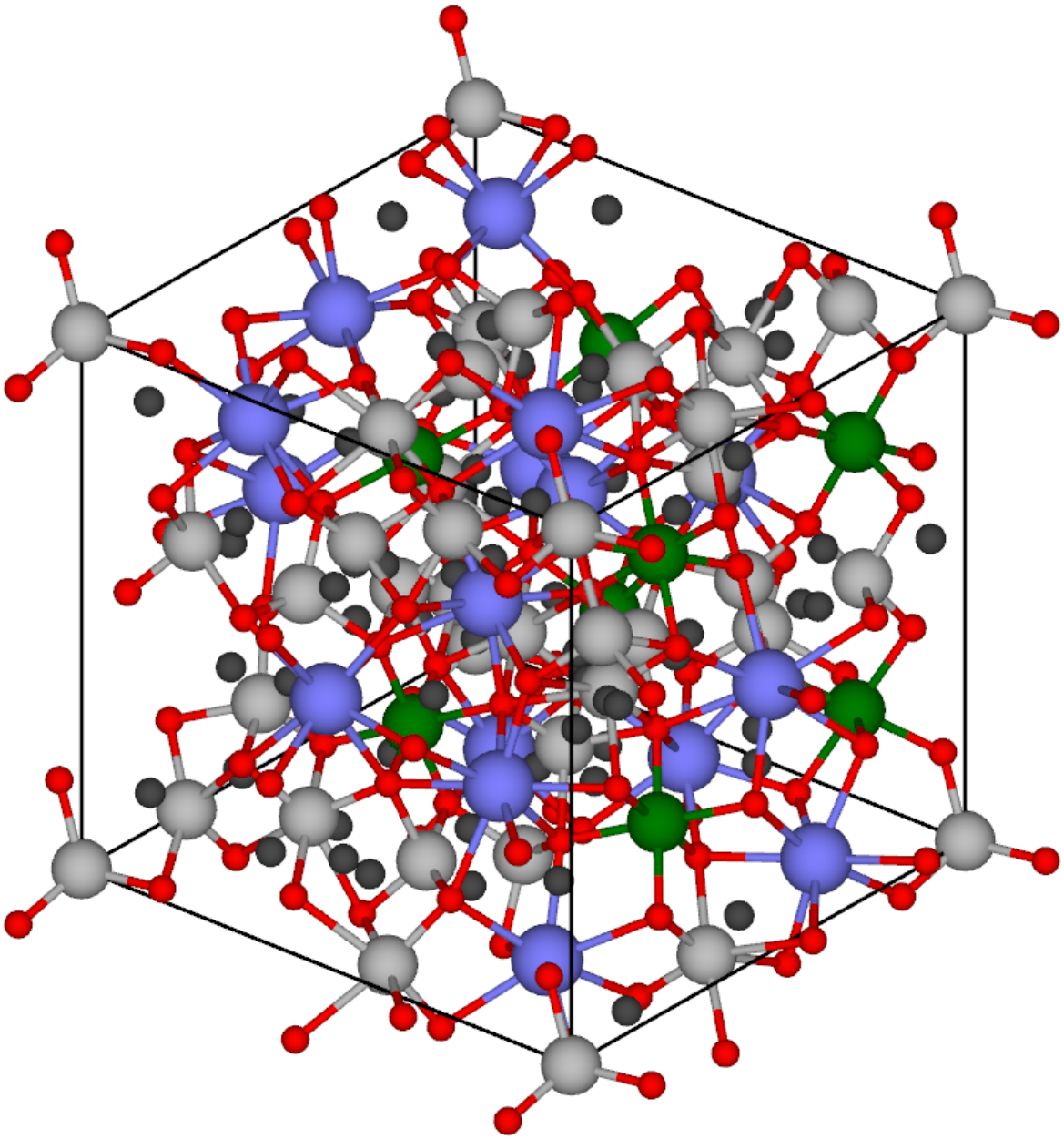

Figure F.2: The LLZO structure with the possible interstitial sites found by the use of the charge density marked in black

G VASP - Files

G.1 INCAR

Listing G.1 shows a typical INCAR file used for relaxation of structures. Everything after exclamation marks are comments and are marked in blue.

```
SYSTEM = Generic Input

start Parameters
  NWRITE      = 2       ! Medium-level information output
  ISTART      = 1       ! read existing wavefunction; if there
  INIWAV      = 1       ! Random initial wavefunction; otherwise
  !ICORELEVEL = 1        ! Print core levels
  !ICHARG     = 11      ! Non-selfconsistent: GGA/LDA band structures
  !NBANDS     = 130     ! No. bands

parallelisation
  NCORE  = 16           ! No. cores per orbital
  !LPLANE = .TRUE.      ! Real space distribution; supercells
  !KPAR   = 2           ! K-point parallelisation

electronic relaxation
  PREC    = Normal   ! Precision level
  ALGO    = Normal     ! SCF minimisation algorithm; 38/48 combo
  ENMAX   = 600        ! Plane-wave cutoff
  NELM    = 200        ! Max SCF steps
  NELMIN  = 2          ! Min SCF steps
  EDIFF   = 1E-05      ! SCF energy convergence
  GGA     = PS         ! PBEsol exchange-correlation
  LASPH   = .TRUE.     ! Non-spherical elements; d/f convergence
  LREAL   = .FALSE.      ! Projection operators: automatic
  ADDGRID = .TRUE.     ! Increase grid; helps GGA convergence
  !IVDW = 11           ! Grimme's D3 VDW correction

ionic relaxation
  EDIFFG = -0.01       ! Ionic convergence; eV/AA^3
  NSW    = 10          ! Max ionic steps
  IBRION = 1           ! Algorithm: 0-MD; 1-Quasi-New; 2-CG
  ISIF   = 2           ! Stress/relaxation: 2-Ions, 3-Shape/Ions/V, 7-Vol
  ISYM   = 0           ! Symmetry: 0-none; 2=GGA; 3=hybrids
  NBLOCK = 1           ! Update XDATCAR every X steps
  KBLOCK = 40          ! Update PCDAT and DOSCAR every X*NBLOCK steps
  ISMEAR = 0           ! Gaussian smearing; metals:1
  SIGMA  = 0.02        ! Smearing value in eV; metals:0.2
  IWAVPR = 1           ! charge density extrapolation: 0-non 1-charg 2-wave
    3-comb
  POTIM  = 0.1       ! Timestep in fs

misc
  LORBIT  = 11         ! PAW radii for projected DOS
  NEDOS   = 2000       ! DOSCAR points
  !LVHAR   = .TRUE.     ! Ionic and Hartree potential
  !RWIGS   = 1.5 1.5    ! Radii for each atomic species
  !LOPTICS = .TRUE.     ! Output OPTIC file
  LVTOT   = .TRUE.     ! Electrostatic potential
  !LELF    = .TRUE.     ! Localisation function

hybrid-dft
  !LHFCALC  = .TRUE.    ! Activate HF
  !PRECFOCK = F         ! HF FFT grid
  !NKRED    = 2         ! Reduce k-grid-even only
  !ALGO     = DAMPED    ! Dampened MD SCF; IALGO=53
  !ALGO     = All       ! SCF Combo; ALGO=58
  !TIME     = 0.30      ! Timestep for IALGO5X
  !HFLMAX   = 4         ! HF cut-off: 4d,6f
  !HFSCREEN = 0.207     ! Switch to screened exchange; e.g. HSE06
  !AEXX     = 0.25      ! 25% HF exchange; e.g. PBE0

```

```
magnetic
  ISPIN    = 2          ! Enable spin polarisation
  !MAGMOM  = 5 0        ! Initial magnetic momoment on each ion
  NUPDOWN  = 1         ! Enforce spin multiplet
  !NELECT = 575
  !LSORBIT = .TRUE.     ! Spin-orbit coupling

dft+u
  !LDAU     = .TRUE.    ! Activate DFT+U
  !LDATYPE  = 2         ! Dudarev; only U-J matters
  !LDAUL    = 2 -1      ! Orbitals for each species
  !LDAUU    = 2  0      ! U for each species
  !LDAUJ    = 0  0      ! J for each species
  !LMAXMIX  = 4         ! Mixing cut-off; 4-d, 6-f

decomposed charge density
  !LPARD = .TRUE.       ! Generate PARCHG
  !EINT  = -10 0        ! Energy range
  !NBMOD = -3           ! With reference to Ef
  !KPUSE = 1            ! Over k-points
  !IBAND = 20           ! Over bands
```

Listing G.1: An example of a typical INCAR file used for relaxing the start and end structures. Everything in blue is not active due to "!" making it a comment

For NEB calculations the the tags in listing G.2 is added to the INCAR. Listing G.3 shows the tags edited and added to run NEB calculations with the Quick-Min optimizer instead of the default VASP optimizer.

```
NEB
  ICHAIN = 0
  IMAGES = 5
  SPRING = -5.0
  LCLIMB = .TRUE.
```

Listing G.2: Tags added to run NEB calculations

```
ionic relaxation
  ISBRION = 3           ! Algorithm: 0-MD; 1-Quasi-New; 2-CG
  POTIM   = 0           ! Timestep in fs

NEB
  IOPT    = 3           ! Choosing NEB optimizer
  MAXMOVE = 0.2
  TIMESTEP = 0.1
```

Listing G.3: Tags added and edited to run NEB calculations with the Quick-Min optimizer

G.2 job

The two following listings, G.4 and G.5, display the job file used for all the relaxations of the start and end structures, and the job file used for all the NEB calculations respectively.

```
#!/bin/bash -l
#SBATCH --job-name=name_of_job
#SBATCH --account=nn9264k
#SBATCH --nodes=4
#SBATCH --ntasks-per-node=16
#SBATCH --time=6:00:00
#SBATCH --exclusive
#SBATCH --partition=normal
SCRATCH_DIRECTORY=${PWD}
module load VASPModules VASP/5.4.4-intel-2017a
mpirun vasp_gam > vasp_out
echo $PWD >> ~/fin_dir
```

Listing G.4: Job file used for relaxation of structures

```
#!/bin/bash -l
#SBATCH --job-name=name_of_NEB_job
#SBATCH --account=nn9264k
#SBATCH --nodes=5
#SBATCH --ntasks-per-node=16
#SBATCH --time=12:00:00
#SBATCH --exclusive
#SBATCH --partition=normal
SCRATCH_DIRECTORY=${PWD}
module load VASPModules VASP/5.4.4-intel-2017a
mpirun vasp_gam_tst > vasp_out
echo $PWD >> ~/fin_dir
```

Listing G.5: Job file used for NEB calculations

G.3 KPOINTS

Listing G.6 shows the KPOINTS file used for relaxing all start and end structures as well as all the NEB calculations.

```
Automatic mesh
0
Gamma
  1   1   1
  0.  0.  0.
```

Listing G.6: KPOINTS file used for all NEB related calculations

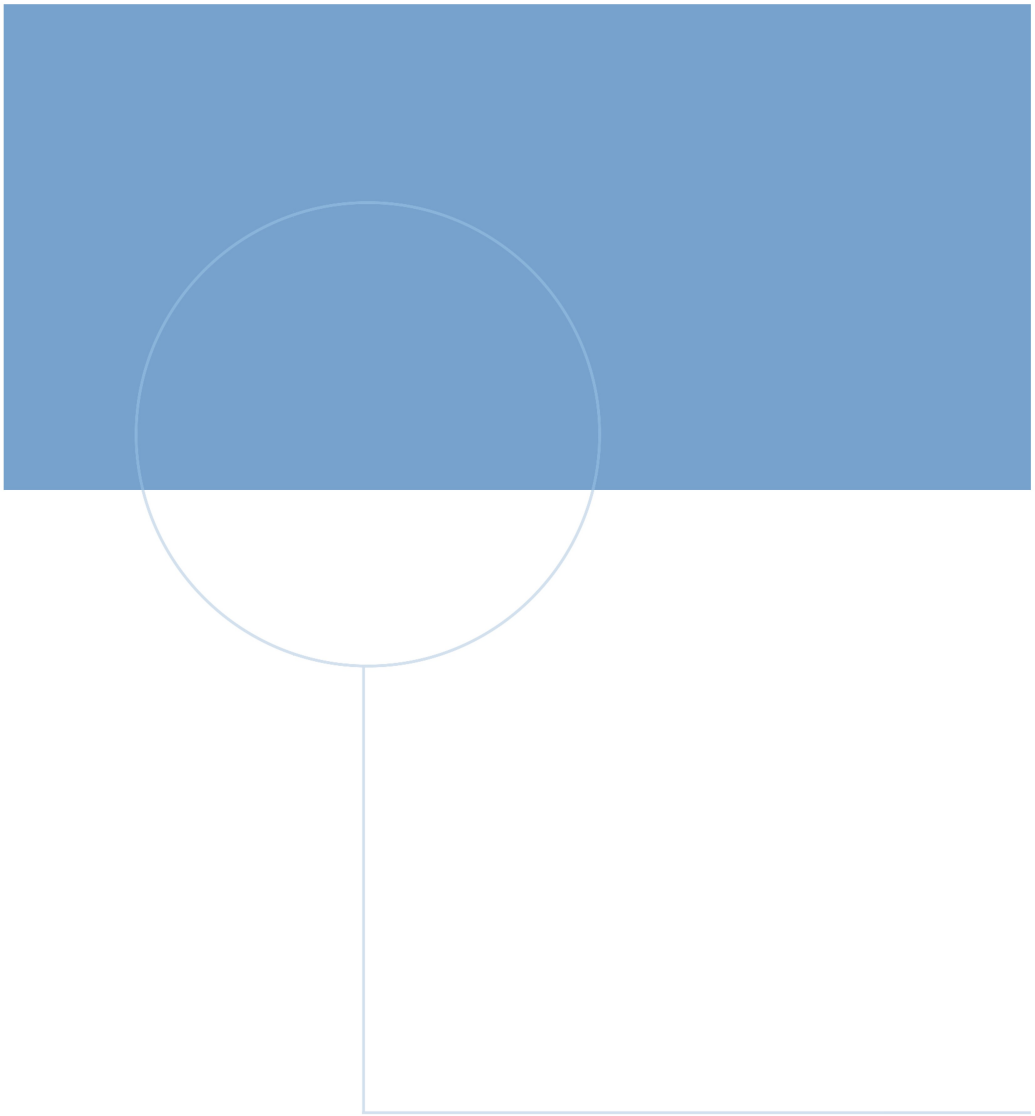

NTNU

Norwegian University of
Science and Technology